Prognostics and Health Monitoring for ECU Based on Piezoresistive Sensor Measurements

am Fachbereich Maschinenbau

an der Technischen Universität Darmstadt

zur

Erlangung des akademischen Grades Doktor-Ingenieur (Dr.-Ing)

eingereichte

Dissertation

vorgelegt von

Alicja Palczynska

aus Breslau - Polen

Hauptberichterstatter:	Prof. Dr.-Ing. T. Melz
Mitberichterstatter:	Prof. Dr.-Ing. S. Rinderknecht

Tag der Einreichung:	23. Oktober 2017
Tag der mündlichen Prüfung:	23. Januar 2018

Fachbereich Maschinenbau
Fachgebiet Systemzuverlässigkeit, Adaptronik und Maschinenakustik
der Technische Universität Darmstadt

2018

Palczynska, Alicja : Prognostics and Health Monitoring for ECU Based on Piezoresistive Sensor Measurements
Darmstadt, Technische Universität Darmstadt,
Jahr der Veröffentlichung der Dissertation auf TUprints: 2018
Tag der mündlichen Prüfung: 23.01.2018

Abstract

This dissertation presents a new approach to prognostics and health monitoring for automotive applications using a piezoresistive silicon stress sensor. The stress sensor is a component with promising performance for monitoring the condition of an electronic system, as it is able to measure stress values that can be directly related to the damage sustained by the system. The primary challenge in this study is to apply a stress sensor to system-level monitoring. To achieve this goal, this study firstly evaluates the uncertainties of measurement conducted with the sensor, and then the study develops a reliable solution for gathering data with a large number of sensors.

After overcoming these preliminary challenges, the study forms a framework for monitoring an electronic system with a piezoresistive stress sensor. Following this, an approach to prognostics and health monitoring involving this sensor is established. Specifically, the study chooses to use a fusion approach, which includes both model-based and data-driven approaches to prognostics; such an approach minimizes the drawbacks of using these methods separately. As the first step, the physics of failure model for the investigated product is established. The process of physics of failure model development is supported by a detailed numerical analysis of the investigated product under both active and passive thermal loading. Accurate FEM modeling provides valuable insight into the product behavior and enables quantitative evaluation of loads acting in the considered design elements. Then, a real-time monitoring of the investigated product under given loading conditions is realized to enable the system to estimate the remaining useful life based on the existing model. However, the load in the design element may abruptly change when delamination occurs. A developed data-driven approach focuses on delamination detection based on a monitoring signal. The data driven methodology utilizes statistical pattern recognition methods in order to ensure damage detection in an automatic and reliable manner. Finally, a way to combine the developed physics-of-failure and data-driven approaches is proposed, thus creating fusion approach to prognostics and health monitoring based on piezoresistive stress sensor measurements.

Zusammenfassung

In dieser Dissertation wird ein neues Vorgehen an Prognostics and Health Monitoring für Automobileanwendung durch Benutzung eines piezoresistiven Spannungssensors vorgestellt. Der piezoresistive Sensor ist sehr entwicklungsfähig für Zuverlässigkeitsanwendungen, weil er die direkte Messung von mechanischen Spannungen ermöglicht, die auf die Schadensentwicklung bezogen werden kann. Die Hauptherausforderung dieser Studie ist die Umsetzung des Spannungsensors für das Monitoring am Systemniveau. Um dieses Ziel zu erreichen, muss die Messunsichercheit von dem Sensor ausgewertet werden. Desweiteren muss ein System entwickelt werden, welches das Messen mit mehreren Sensoren in der selben Zeit ermöglicht.

Nachdem der Rahmen für die elektronische Systemmonitoring mit dem piezoresistiven Spannungssensor festgelegt wurde, konnte ein Vorgehen an Prognostics and Health Monitoring, welches den Sensor beinhaltet, etabliert werden. Es wurde ein Hybridvorgehen ausgewählt, welches das Model Based und das Data Driven Vorgehen enthält und die Nachteile der getrennten Benutzung dieser Methoden minimalisiert. Als erstes muss ein Lebensdauermodel für das untersuchte Produkt entwickelt werden, das von FEM Modellierung unterstützt wird. Die detaillerte FEM Analyse gibt eine wertvolle Einsicht in das Produktverhalten und ermöglicht quantitative Evaluierung von der Belastung, die auf die betrachtete Konstruktionselemente wirkt. Als nächstes muss das Echtzeitmonitoring von dem untersuchten Produkt durchgeführt werden, um die Beurteilung von den Lebensdauer unter Verwendung von dem entwickelten Lebensdauermodel zu ermöglichen. Jedoch steigt die Belastung auf die betrachteten Konstruktionselemente plötzlich, wenn die Delamination auftritt. Deswegen wird das entwickelte Data Driven Vorgehen auf die Delaminationerkennung basierend auf die Spannungssensormessung fokusiert. Es benutzt statistiche Strukturerkennungsalgorithmen, die die automatische und zuverlässige Delaminationdetektion ermöglichen. Letztendlich wird das Hybridvorgehen an PHM vorgeschlagen, das beide entwickelte Methoden kombiniert.

Declaration

Hiermit versichere ich, die vorliegende Dissertation ohne Hilfe Dritter nur mit den angegebenen Quellen und Hilfsmitteln angefertigt zu haben. Alle Stellen, die aus Quellen entnommen wurden, sind als solche kenntlich gemacht. Diese Arbeit hat in gleicher oder hnlicher Form noch keiner Prfungsbehr vorgelegen.

Darmstadt, den

_____

(Alicja Palczynska)

Contents

Nomenclature

List of Abbreviations

ADC Analog to Digital Converter

AHP Analytic Hierarchy Process

ASSIST Alliance for Solid-State Illumination Systems and Technologies

BGA Ball Grid Array

CCD Charge Coupled Device

CMOS Complementary metal-oxide-semiconductor

CPU Central Processing Unit

CS Creep Strain

CSED Creep Strain Energy Density

CSTH Continuous System Telemetry Harness

CTE Coefficient of Thermal Expansion

DAC Digital to Analog Converter

DAQ Data Acquisition System

DIC Digital Image Correlation

DMA Dynamic Mechanical Analysis

DoE Design of Experiment

ECU Electronic Control Unit

EMC Epoxy Molding Compound

EMI Electromagnetic Interference

FEA Finite Element Analysis

FEM Finite Element Method

FFT Fast Fourier Transform

FM Failure Mode

FMEA Failure Modes and Effects Analysis

FMMEA Failure Modes, Mechanisms and Effects Analysis

GND Ground potential

HDD Hard Disk Drive

I/O Input/Output

IC Integrated Package

IGBT Insulated Gate Bipolar Transistor

JEDEC Joint Electron Device Engineering Council

LED Light Emitting Diode

LGA Land Grid Array

LS-SVD Least Square Singular Value Decomposition

LSB Least Significant Bit

LTCC Low Temperature Cofired Ceramics

MD Mahalanobis Distance

MLCC Multilayer Ceramic Capacitor

MLP Multi-Layer Perception

MOSFET Metal Oxide Semiconductor Field Effect Transistor

MSB Most Significant Bit

MSET Multivariate State Estimation Technique

OOR Ordered Overall Range

PCB Printed Circuit Board

PEMI Portable Engineering Moire Interferometry

PGA Programmable Gain Amplifier

PHM Prognostics and Health Monitoring

POD Proper Orthogonal Decomposition

PoF Physics of Failure

PS Plastic Strain

PSED Plastic Strain Energy Density

PSO Particle Swarm Optimization

PTL Predicted Total Life

RBF Radial Basis Function

RUL Remaining Useful Life

S.M.A.R.T. Self-Monitoring, Analysis and Reporting Technology

SAM Scanning Acoustic Microscopy

SMD Surface Mounted Device

SoH State of Health

SPRT Sequential Probability Ratio Test

SVD Singular Value Decomposition

SVM Support Vector Machine

TBM Transferable Belief Model

TFA Time Frequency Analysis

TMA Thermo-Mechanical Analysis

VAM Volume Average Method

VDD Power supply potential

VDoE Virtual Design of Experiment

List of Symbols

$\alpha_{U_{Th}}$ temperature coefficient of threshold voltage

α_i positive Lagrangian multipliers

α_{Cu} the coefficient of thermal expansion of copper

α_{eff} effective coefficient of thermal expansion

α_{Ppg} the coefficient of thermal expansion of prepreg

ϵ_x, ϵ_y normal strains

γ_{xy} shear strain

λ parameter in Box-Cox transformation

μ_e mobility of electrical carriers in the channel of transistor

Π_D^n, Π_{44}^p, Π_S^n, Π_S^p, Π_{12}^n, Π_{12}^p effective piezoresistive coefficients of silicon influenced by the circuit

π_D^n, π_{44}^p, π_S^n, π_S^p, π_{12}^n, π_{12}^p piezoresistive coefficients of silicon

Ψ a damage parameter e.g. temperature range, mean temperature, current density, plastic strain

ρ_{Si} resistivity of silicon in chosen direction

σ_{11} normal in-plane stress in x-direction

σ_{12} shear stress in xy-direction

σ_{22} normal in-plane stress in y-direction

σ_d difference in normal in-plane stresses

σ_S singular value of a matrix

C correlation matrix

C_1, C_2 constants for the lifetime equation, usually determined experimentally

C_{ox} capacitance of the oxide layer in MOSFET

D_N damage ratio at the end of N cycles/days/hours

E_{Cu} the Young's modulus of copper

E_{eff} effective value of Young's modulus

E_{Ppg} the Young's modulus of prepreg

$f(\Delta T)$ function describing temperature effects on resistivity change

f_s the spatial frequency of the virtual reference grating (2400 lines/mm)

I_1, I_2 currents in both branches of current mirror

I_{D0} reference current (in an absence of mechanical stress)

I_D drain current of MOSFET transistor

$K(x_i, x_j)$ Gaussian radial basis function

N number of cycles/days/hours of operation

N_d net impurity concentration

N_f number of cycles to failure

n_f number of cycles performed at a given stress level

N_x, N_y the fringe orders in x- and y-directions

q_e electrical charge of majority carrier

S singular values matrix

T_0 reference temperature

U, V displacements in x- and y-directions

U_{GS} voltage between gate and source of MOSFET

U_{orth},V_{orth} orthonormal matrices

U_{Th0} threshold voltage at the reference temperature

U_{th} threshold voltage of MOSFET

V_{Cu} the volume fraction of copper

V_{el} the volume of an element

V_{Ppg} the volume fraction of prepreg

W width of the MOSFET channel

W_{AVG} the average creep (plastic) strain energy density accumulated per cycle in a critical layer

W_{SED} the creep (plastic) strain energy density accumulated per cycle in each element

X_{ij} performance parameter matrix

Z_{ij} normalized performance parameter matrix

Chapter 1

Introduction

1.1 Motivation

1.1.1 Benefits of autonomous driving

Autonomous driving is a technology that has potential to provide solutions for many challenges of our fast developing world, and it also can ensure safety on the roads. It can prevent up to 90% of all road accidents that are caused by human error [1]; these errors are mainly due to poor risk assessment, improper situation analysis, and slow or incorrect reaction of the driver. All of these problems do not concern autonomous driving systems. These systems are not susceptible to fatigue, nor can they be affected emotionally. Additionally, their decision time is much shorter. With autonomous driving and the internet-of-things technology, traffic flow can become more efficient than before. This change will most likely lower the level of stress for many drivers. It can also reduce fuel consumption and the level of exhaust emission. Such an effect is particularly important as more people are anticipated to live in urbanized areas in the future, and in these areas traffic jams and air pollution could become a major problem. Moreover, the assistance systems can improve safety and comfort of driving, which is especially crucial as we are facing demographic changes. In particular, these systems can help the growing elderly population to remain active. An additional benefit from the introduction of assistance systems is the productive use of time during driving, thus enhancing driving pleasure. This is a clear advantage as individuals are becoming more mobile and connected every day. In particular, the young generation would rather spend their time using mobility solutions than driving a car.

The automotive industry is already aware of all these advantages and the changes that this technology will bring to the automotive market. Therefore, autonomous driving is currently in an intensive development phase, which includes studies regarding reliability methods as these are crucial for avoiding sudden malfunctions of such a system.

1.1.2 Reliability issues

The autonomous driving technology is a huge challenge for the engineering community with regards to reliability. The human error factor is eliminated in a situation where the steering of a car relies only on the electronic control system, and the whole risk of malfunctioning is shifted to the system. Furthermore, as electronic control systems become more complex, reliability issues also become more complicated. In other words, there are simply many more things that can go wrong. The interactions between different parts of a system are also very complex—it is very difficult to predict how even a minor change in one part of a system can affect its whole behavior. To get a sense on the current situation, some data can be introduced here. Among cars over a three-year usage in the 2008-2013 period [2], the number of electrical faults increased

by 66%. The least reliable electric systems experienced a failure in one out of every three cars per year [2]. The most reliable vehicle model had only one breakdown in every seven cars (see Figure 1.1.1). On average, every fourth vehicle developed a problem in its electrical system. In order to introduce autonomous driving features on the market, this situation must be drastically improved.

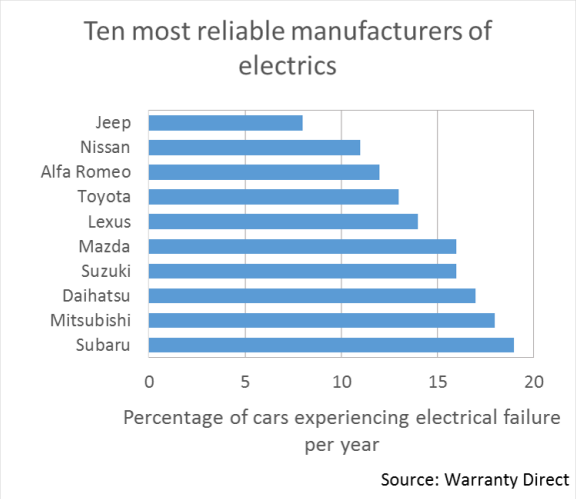

Figure 1.1.1: Ten most reliable manufacturers of electric systems [2].

One way to achieve this goal is redundancy. The idea behind it is that in case of failure, an additional system should switch on to enable a safe stop of a vehicle. For example, in the case of an autonomous steering system failure, an additional system would take control over the car or pass the control to the driver. However, that should concern not only the steering unit but also other electronic systems (e.g., the electronic control unit). Thus, using redundancy in many of the electronic systems that are in the vehicles currently available would be very expensive. The repair time and cost would also increase significantly.

A more viable solution that addresses reliability concerning autonomous driving would be prognostics and health monitoring (PHM). It is a method that enables the reliability assessment of a system during its actual operation. Monitoring the state of health of electronics in real time enables a prediction of the oncoming failure. Thus, it mitigates the risk of sudden failure which may cause further damage, and it does so by informing the user before the fault occurs. PHM is a new and very promising field; it provides warnings about imminent failure, and it also increases system availability. Moreover, it lowers the cost of inspections and gathers the data on the load history of a product for future design optimization, qualification, and root cause failure analysis [3]. However, to implement this method it is crucial to monitor the system using suitable sensors. Usually, appropriate sensors that can measure load are applied to the system, such as temperature sensors for thermal loads or acceleration sensors for vibration or shock. However, these sensors are not able to directly measure the parameters related to a damage. This can be accomplished using a silicon-based piezoresistive stress sensor that is able to directly measure mechanical stress. Thus, it would be very interesting to apply this type of sensor to reliability applications, and this thesis investigates how the sensor can be used for implementation of PHM methodology for automotive electronics.

1.2 Objectives

The main research question that is addressed in this study is whether a piezoresistive stress sensor can be integrated within an ECU and whether it can be used to monitor its state of health. Thus, the main goal of this research is to make a feasibility study on the application of a piezoresistive silicon stress sensor for PHM methodology for automotive applications. The main challenge in this study is to apply a stress

sensor to system-level monitoring. To achieve this objective, the study firstly evaluates the uncertainties of measurement conducted with the sensor. After this, a reliable solution for gathering data from a large number of sensors can be developed.

Next, the study establishes an approach to PHM involving the piezoresistive stress sensor. To realize this goal, a physics-of-failure model is firstly established for the investigated product. Additionally, a data-driven approach is developed in order to detect any anomalies that may cause a change in the loading conditions of the considered design elements. Finally, a method to combine the developed physics-of-failure and data driven approach is proposed.

1.3 Outline

The topics covered in this thesis are organized into nine chapters, and this section provides a brief description of the contents of each chapter.

Chapter 2 presents the state-of-the-art research concerning PHM methods. The focus is on introducing a fusion approach for PHM since this is the approach adapted in this work. A fusion approach for PHM combines both PHM techniques developed up until this point—including model-based and data-driven approaches. This approach also takes advantage of virtual modeling for early development stage optimization of design, as well as for physics-of-failure modeling. All three of these methods are explained in the chapter along with examples of their application from present literature. Additionally, the chapter clarifies the general scheme for creating PHM methodology; such a scheme is later adapted using the piezoresistive stress sensor.

Chapter 3 describes the piezoresistive silicon-based stress sensor that is a main tool proposed for PHM methods implementation in this thesis. The advantages of this sensor are presented along with the challenges encountered in the duration of this study. A detailed description of the working principle and governing equations is provided. Additionally, the uncertainties of measurements are assessed to enable the practical use of this sensor.

Chapter 4 discusses the product type investigated in this research and identifies the microelectronic package considered for this study. The chapter also introduces a test vehicle designed to study reliability of the investigated package on the system level.

Chapter 5 presents the results of virtual modeling. In this thesis, the virtual modelling technique is used mainly for the accurate physics-of-failure modeling. The model is prepared in a highly meticulous way with a special emphasis on accurate material modeling and geometry representation. For a proper active load condition modeling, a detailed multi-domain and multi-level simulation of an investigated test vehicle is performed.

Chapter 6 describes the results of the investigation on model-based approach to prognostics. The test vehicles are subjected to an accelerated reliability test under active and passive load conditions. During the experiments, the load acting on the test vehicles is continuously monitored. The results of this experiment are then correlated with the simulation results to obtain a lifetime model and to predict the state of health of the system.

Chapter 7 describes the results of the investigation on the data-driven approach to prognostics. First, the chapter presents a feasibility study on damage detection using the stress sensor. This study uses the results of a simulation with different investigated failure modes. The applicability of two statistical pattern recognition algorithms for failure detection is studied. The two investigated algorithms are the Mahalanobis distance and singular value decomposition. Their performances are then compared. Next, a support vector machine algorithm for a damage typology is implemented. Finally, the algorithms are tested with data coming from measurements that were gathered during the delamination progression.

Chapter 8 provides an explanation on how both physics-of-failure and data driven approaches can be brought together in order to predict the remaining useful life of a product in a systematic way. This method benefits from the advantages of both approaches and helps to limit their drawbacks.

Finally, Chapter 9 summarizes the main achievements of this thesis, and the conclusions are drawn. In addition, my original contribution to the knowledge gap is presented.

Chapter 2

State of the art

2.1 Introduction

PHM is a relatively new discipline that focuses on the development of methods to evaluate the reliability of a system in its real life cycle conditions. The basis of PHM consists of monitoring the system during its use in real time so that impending failures could be predicted. Thus reliability can be ensured when the user is informed before the failure occurs.

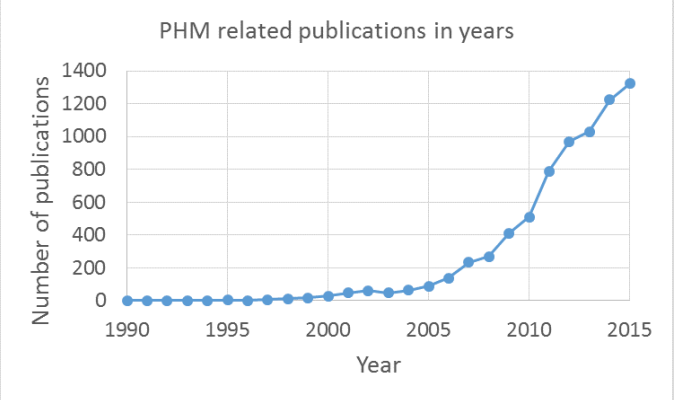

Figure 2.1.1: Publication numbers concerning PHM during the last 20 years based on search hits on Google Scholar.

The topics of PHM has continued to draw more attention from scholars; this can be seen from the number of publications devoted to this subject (see Figure 2.1.1). A possible reason for the growing interest is the many potential benefits that PHM can bring. Some benefits include:

- Warning of system failure in advance
- Lower life-cycle cost (e.g., a reduction of inspection costs or downtime)
- Increase of system availability (through the extension of maintenance cycles)
- Knowledge of load history for future design and root cause failure analysis

Figure 2.1.2 presents the general process flow of PHM. Sensors interrogate the system, and the state of health (SoH) can be assessed based on gathered data. That process is called diagnostics. Prognostics consists of an estimation of the remaining useful life (RUL) based on known current SoH. Knowing the RUL enables forecasting of maintenance actions, thereby improving safety and cost management.

There are two main groups of prognostics methods—physics-based approaches and data-driven approaches. A method that merges all of these methodologies is referred to as a fusion approach, which employs all the advantages of the underlying methods while minimizing their deficiencies.

All these methods are described in detail in the following sections so that the state of the art in PHM can be better understood. The main goal of this research is to produce a feasibility study on the application of piezoresistive silicon stress sensors for PHM in automotive applications, and hence it is important to know which methods and approaches are already available.

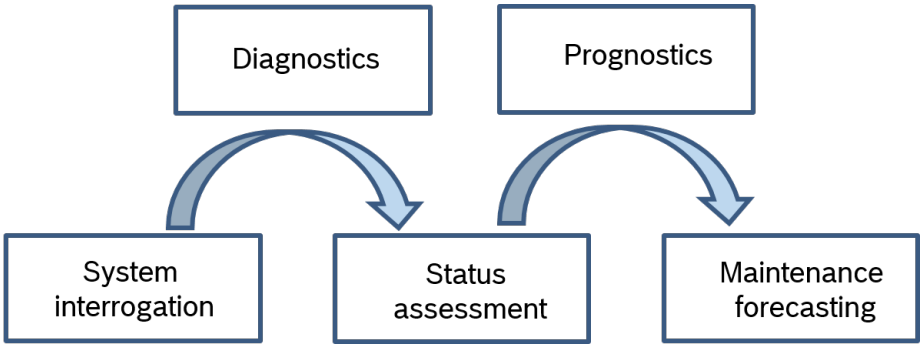

Figure 2.1.2: Process flow of PHM.

2.2 Virtual modeling

Numerical simulations play an important role in the product development process in that they assess the reliability of the product. The concept of simulation-driven design can help also to optimize the product at its early development stage, thus leading to the reduction of the required development time. In this research, virtual modelling techniques are used to support not only product development but also the development of the PHM approach; with such functions, these techniques can go beyond the state of the art. In this section, a short description is provided for the virtual modelling techniques that are available for product development in different development stages. These techniques are also summarized in Figure 2.2.1.

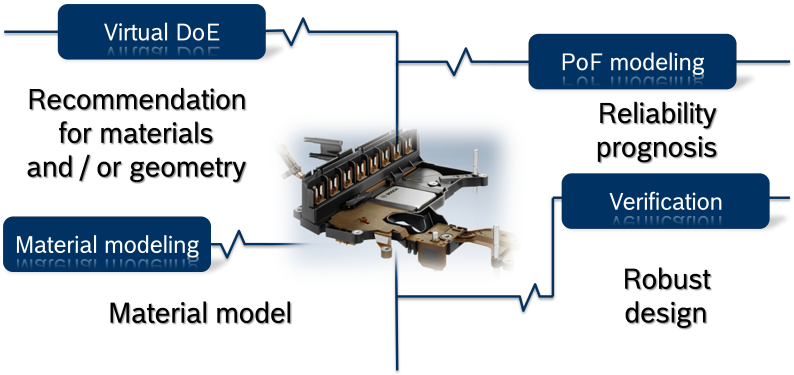

Figure 2.2.1: Schematic of the simulation driven design concept.

At the early design phase when very limited information is available regarding the designed component, numerical simulation allows a virtual study of the effect of the parameters, such as geometries, material properties, and loading conditions. As for PHM methodology development, the virtual modeling techniques can help to determine the optimal position of the sensors or canary devices so that they are subjected to the maximal load that can occur in the system (e.g., maximal temperature point). At this stage, there is no information on allowable loads that the designed component can withstand. Yet, it is still possible to

qualitatively optimize the design to minimize overall deformation and the stress/strain state. An example of such a simplified numerical method proposed for the very early design phase was presented in [4], in which virtual design of experiment (VDoE) was used to study the effect of molding compound on the stress state inside IC package. The results were used for recommending a molding compound for the package design.

Detailed material characterization is conducted as a next step. It is crucial to have correct material models implemented in order to obtain quantitative predictions on the system behavior. The studies in [5] and [6] have presented a characterization of epoxy-based thermosets. Linear viscoelastic and nonlinear viscoelastic models were developed based on the results obtained from dynamic mechanical analysis (DMA) finite stress tests. After this step, these models were implemented into a FEM simulation, and numerical predictions were compared with experiment results to confirm the accuracy of FEM prediction.

The third part of a simulation-driven design focuses on physics-of-failure modeling. To obtain the quantitative results required in this study, a couple of conditions must be satisfied. The process flow of the proposed physics-of-failure simulation is shown in Figure 6.3.1. First, a detailed geometry of all design elements must be taken into account. The geometry is typically validated by cross sectioning [7], x-ray inspection, or an etching of the molding compound. Additionally, the material models must be known at this stage. Furthermore, the boundary and loading conditions must be defined as accurately as possible. For an accurate prediction of thermo-mechanical behavior under an active power condition, the power dissipation in all design elements should be taken into account. The detailed modelling enables risk assessment for different failure modes. Additionally, a physics-of-failure based lifetime model for a given failure can be built, which can then be further used to predict the RUL using a model-based approach to PHM.

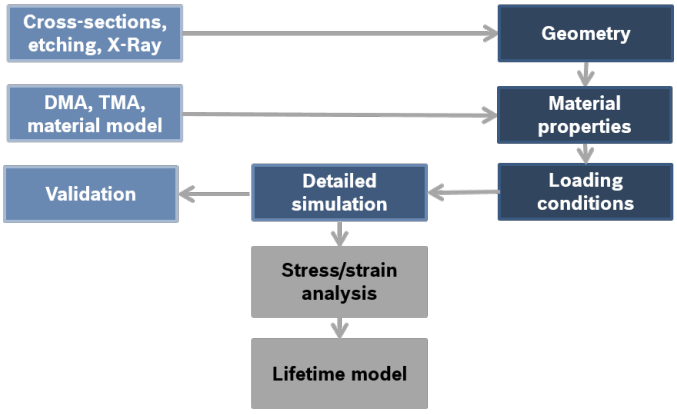

Figure 2.2.2: PoF modeling workflow.

The last step of the simulation-driven design is verification. At this point, the virtually optimized ECU is built and tested. The experimental results are used for verifying the numerical predictions. Depending on the simulation type, different experimental methods can be implemented. For the validation of thermal models, methods such as thermography [8] and temperature (e.g., using thermocouples) or thermal impedance measurements [9], [10] can be used. Various methods are also available to validate thermo-mechanical simulations. Most commonly utilized are optical methods that measure deformations (e.g., digital image correlation for warpage measurements [11]) or moiré interferometry for in-plane displacement measurements [12]. Other methods including stress [13] and strain [14] measurements can be applied successfully.

2.3 Model-based approach

The basis of the physics-of-failure approach consists of an in-situ monitoring of the system along with the prior knowledge on failure modes and the model of damage to assess the RUL [15]. The procedure of

physics-based prognostics is shown on Figure 2.3.1. The prognostics uses a mathematical representation of the system and thus requires prior knowledge concerning product life cycle, materials, construction, and failure mechanisms. The failure mode should be identified, and its appearance must also be described in a mathematical way to use this method. To be able to assess the level of stress in a design element and to compute accumulated damage, it is necessary to implement FEM modelling techniques. Additionally, the parameters related to the failure modes and mechanisms in question must be defined and monitored. These parameters must be directly related to the loading conditions of a system. After gathering data, it should be reduced in such a way that the load history evaluation is feasible. The reduced data is then used as input for the physics-of-failure model, and the derivation of RUL is also made possible.

The physics-of-failure method can predict RUL under varying loading conditions. It provides a full understanding of the system behavior. Thus, the information gathered in the process of developing this methodology for a given product can be used also to optimize the product. However, an assumption made with this method is that the failure model is accurate. This is not always true, especially when taking into account the complexity of various scenarios, such as loading conditions in modern electronic systems or new materials introduced in the systems. Furthermore, the system level RUL estimation may be challenging due to complexity of the problem. It is not possible to estimate the RUL for every component in the system; the focus must be put on critical components. Additionally, it is not simple to find sensors that directly measure the information that is relevant for failure models.

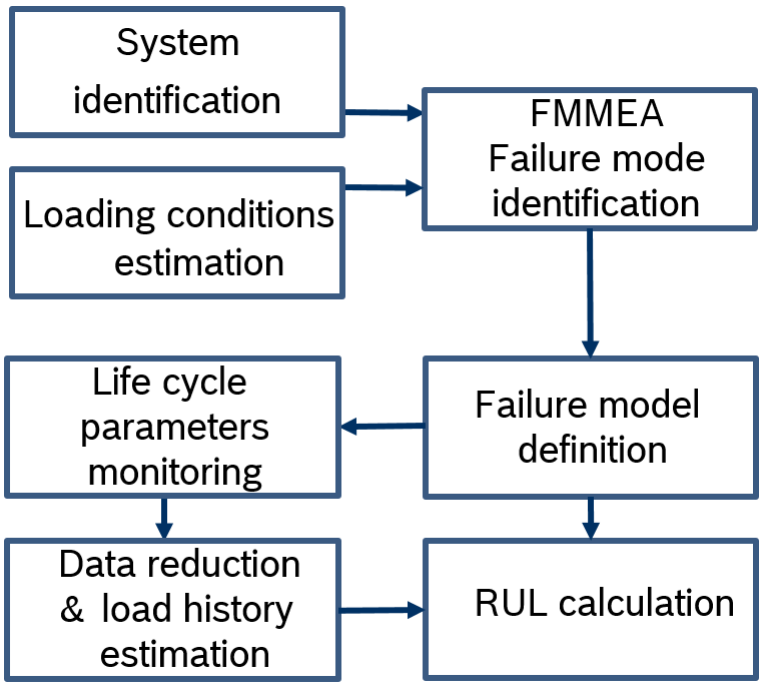

Figure 2.3.1: The process flow of physics-based approach to prognostics.

There are many examples of use of this method in the literature. Yin et al. [16] used it to evaluate the RUL of an IGBT power module. The measured parameter was current flowing through the component. Based on this, the junction temperature was calculated using a compact thermal model. The next step involved an analysis of the load profile using a rainflow algorithm; this is done to obtain the knowledge of the number of cycles with a given temperature change and mean. To construct the reduced order model that describes an accumulated plastic strain in dependence of temperature cycles, the FEM model was created, and the results were collected according to the design of experiment (DoE) with multiple values of temperature parameters. The value of the accumulated strain for every group of thermal cycles separately was used in a strain-based lifetime prediction model. The accumulated damage was then calculated using the Palmgren–Miner rule.

Another approach was presented in [17], [18]. These studies gathered and analyzed the data for the environmental loads on a printed circuit board (PCB) placed under the engine hood of a car. Temperature and vibration sensors were placed on the test board, as well as circuitry to monitor the resistance of solder joints. The data was used along with appropriate failure models to evaluate the damage in the solder joints. The thermal fatigue failure model was based on the temperature cycles amplitude and the rate of temperature changes. To extract needed information from the data gathered by the temperature sensor, both the ordered overall range method and rainflow analysis were used. Based on the vibration data gathered by the accelerometer, power spectral density was calculated. Then, the transformed data was used as an input for the failure model. Additionally, the damage due to shock load—which occurs during an accident—was evaluated. After this, the Palmgren–Miner rule was used to calculate the total accumulated damage in the solder joints. Finally, the data concerning accumulated damage was confronted with the signal from the resistance monitoring device. A good correlation was observed.

In [19], a PoF approach for solder joints was presented; this approach was based on materials behavior modelling. The study focused on the development of a software solution that would be able to accurately predict the damage accumulation within solder joints on a system level in an efficient way. For the basis for the calculations, the study developed microstructural failure models for the solder joint fatigue. A couple of different models was embedded into the software, mainly models of crack nucleation, microscopic crack growth, and crack propagation. Additionally, a Monte-Carlo simulation was introduced to account for a random grain structure of solder. The input to the failure models was the information on the initial state of the system and field usage conditions. To estimate the initial damage state, a couple of methods were used. First, using cross-sections of the investigated samples, the real geometry and its variability were determined. Then, the residual stress that is introduced by manufacturing processes and aging due to storage was assessed using modelling techniques. The information about field usage condition was gathered by temperature and vibration sensors and then translated by means of FEM simulations to obtain detailed data on loads in every point of a test vehicle. To make the analysis computationally efficient, the investigated system was modelled in a hierarchical manner—the system was divided into components which were then further divided into sub-components so that every interconnect can be analyzed separately.

More examples of the development of model-based approach methodology based on the external load measurements—such as temperature or vibration spectrum—can be found in [20]–[22]. As mentioned, this present study focuses on the implementation of the piezoresistive stress sensor that can directly monitor the mechanical load that causes the damage and thus may be more suitable for monitoring of the SoH. In the next sections, implementation steps of a physics-of-failure based approach are discussed in greater details. A similar implementation scheme is used in this work to develop the model-based approach using the piezoresistive stress sensor.

2.3.1 FMMEA

The first step that must be executed in order to implement a physics-of-failure prognostics approach is to perform a thorough analysis of the investigated system. This process starts with a detailed structure analysis, including the establishing of all functional relationships and physical connections between the components [23]. Then, the load acting on the system during its life cycle must be defined. It may be a single mechanical, thermal, electrical, chemical load or a combination of two or more load types. This leads to a failure mode, mechanism and effects analysis (FMMEA) that allows users to identify and prioritize potential failure modes.

The FMMEA was proposed by Pecht et al. [24]-[25] to address the limitation of the failure mode and effect analysis (FMEA). FMEA is widely used to identify potential failures and their effects on product reliability [26]. It also identifies measures that can be taken to minimize the risk of a failure. In the electronic industry, FMEA is used to analyze the system behavior early in the development process to enhance its reliability

[27]. Although FMEA is complex, it does not identify the failure mechanisms and models. It assesses which failures can occur but does not analyze the physical processes that lead to them—this is the main difference between FMEA and FMMEA. Thus, FMEA methodology is mainly used for safety analysis [28]-[30].

FMMEA allows users not only to identify the potential failure as well as its effect on the functionality of a product but also the mechanisms, which actually lead to failures under complex load conditions [31]. Failure mechanisms are the processes that induce failures under various loads (e.g., electrical, thermal, and mechanical) [32]. Proper identification of failure mechanisms is essential for understanding why the failure modes occur. This process should be supported by stress analysis in order to determine the stress levels in critical design elements under a known load. The stress analysis is usually supported by FEM simulations. This knowledge can be further used to plan the tests and optimize the nominal design. Additionally, failure models can be identified. They are mathematical descriptions used for quantitatively evaluating the susceptibility to failure, which is required for predicting the useful life span of a product. In summary, FMMEA requires a clear understanding of the relationship between the requirements of the product and its physical characteristics. Furthermore, it defines the interactions between materials and stress under operating conditions.

The results of the conducted FMMEA for the investigated ECU are presented in Section 6.2.

2.3.2 Life cycle monitoring

Once a failure model is established, the appropriate parameters that require monitoring during the life cycle of a product must be identified. The choice of load parameters to be recorded depends on several factors, such as the available methods, the type of investigated failure mode and mechanism, the conditions that lead to the failure, and the inputs of the defined failure model. After this, the monitoring of the relevant environmental load enables the in situ assessment of the accumulated damage. The novelty of present study is that a sensor that can directly measure mechanical stress is used for monitoring the system. Thus, the monitored parameter will not be an environmental load but the internal load in the ECU.

In most cases, the environmental loads acting on a product are monitored, and those may be of various nature — such as thermal, mechanical, chemical, or electrical. The thermal loading monitoring should take into account the steady state temperatures and temperature ranges, as well as the temperature gradients, ramp rates, and temperature cycles [15]. Similarly, for the mechanical loads, both vibration and shock should be considered. To gather useful information on loading conditions, a suitable sensors must be chosen. First of all, these sensors should be precise and should have short response time. Additionally, they should be easy to integrate within a monitored system, and hence they should be characterized by small size, small weight, low power consumption and be easy to install [33]. Moreover, they should be placed in a system in such a way where they are able to capture all the critical load parameters. The temperature sensors should be able to capture the temperature acting on a design element in question and thus should be located in its close vicinity. A separate vibration sensor should be provided for every mechanically independent part of the system.

The considerations on applicability of the piezoresistive stress sensor for the ECU monitoring can be found in Chapter 4.

2.3.3 RUL calculation

RUL calculation is based on a damage accumulation model. A damage accumulation model predicts, how the different loads over different time periods are influencing the reliability. Although various models for predicting the accumulation of damage have been proposed and reviewed [34], the most widely used is

Palmgren–Miner's rule [35]. There are several other linear models available, such as the models by Lundberg, Langer, or Smith, as well as nonlinear models like by Henry or by Corten and Dolan [34]. However, the simplicity and reasonable accuracy of Palmgren–Miner's method have made it the choice among scholars, as seen in the method's widespread application. Palmgren–Miner's model assumes linear accumulation of damage. The damage accumulated due to one stress level loading is directly proportional to the number of cycles performed at this stress level and can be described with the following equation:

$$D_n = \frac{n_f}{N_f} \tag{2.3.1}$$

Where:
n_f - number of cycles performed at a given stress level
N_f - total number of cycles at a given stress level that would provoke failure

The damage occurs when the combined damage indexes from different stress levels are totaled to 1:

$$\sum D_i = \sum_{i=1}^{n} \frac{n_i}{N_i} \leq 1 \tag{2.3.2}$$

The main disadvantage of this model is the fact that it does not take into account the order of load application, even though it has been shown that the history of loading has influence on the reliability [36].

Based on the damage index, the RUL of a product can be assessed. Additionally, it is necessary to assume the future loading conditions that act on a system. With this in mind, the calculation can be performed in two ways. First, the approach presented in [37] can be applied, according to this formula:

$$RUL_N = N \cdot \left(\frac{1}{D_N} - 1 \right) \tag{2.3.3}$$

Where:
N - number of cycles/days/hours of operation
D_N - damage ratio at the end of N cycles/days/hours

This method uses an average over the loading conditions from all time periods until N as the predicted future loading conditions. It can lead to problems in some cases — for instance, when the load during the previous usage cycle is much below average, the calculated RUL grows with respect to the last evaluation. Therefore, this method is recommended for the cases in which the loading conditions do not show big variability.

Another method was proposed in [17] to handle this limitation. Here, an iterative approach to RUL calculation is presented, according to the relation:

$$RUL_N = RUL_{N-1} - D_N \cdot PTL \tag{2.3.4}$$

Where:
RUL_{N-1} - remaining useful life calculated at the end of N-1 period
D_N - damage ratio at the end of N cycles/days/hours
PTL - predicted total life

The total life is calculated once at the beginning of product usage, assuming some average loading conditions. Then, according to the actual usage conditions, the RUL is calculated in the real time.

It is also worth noting that the prediction of RUL based on the physics-of-failure model is always related to some uncertainties. According to [38], there are four main sources of uncertainty in the lifetime predic-

tion, namely measurement uncertainty, parameter uncertainty, failure criteria uncertainty, and future usage uncertainty. These should be evaluated and taken into account in the process of RUL calculation.

In this work, an iterative approach to calculate RUL is adapted, and its realization is presented in Sections 6.4 and 7.2.

2.4 Data-driven approach

Data-driven approach is used in the case where system model is not available. This approach uses historical data and knowledge on failure influence on the system along with statistical and machine learning methods to estimate RUL. It is generally used for system-level degradation, and it puts focus on obtaining patterns and describing relationships that exist in the data gathered from the system. Such data can consist of the temperature, vibration, voltage, and currents.

A data-driven approach does not require either knowledge regarding material properties or the construction of the investigated system; the approach is able to capture complex relationships and learn trends without specific failure modes knowledge. However, the historical data on the system in its healthy and damaged states are needed. The challenge in obtaining the data is that it is impossible to collect the data about all possible failures, given that the modifications of the design are introduced constantly. Moreover, in this method, damage models are created based on the data gathered under specific loading conditions and corresponding failures. Thus, a change of loading condition can lead to different failure and detection problems. Additionally, the root cause analysis of damage is limited when using this method. Furthermore, the non-exact, non-linear, and non-stationary characteristics of a system can constitute a challenge to the detection algorithms and can lead to incorrect prediction [39]. Aside from this, a question of reliability of the sensors must be raised since erroneous monitoring data can provide unexpected responses.

The process flow of the data-driven approach is presented on Figure 2.4.1. Usually, the employment of the data-driven approach to prognostics includes gathering data, describing how the measured signals change during different kinds of failures, constructing the diagnostic matrix, and then applying correlation algorithms during the real-time monitoring of parameters in order to predict possible impending failure. The process starts with analysis of the system in question. To identify the monitored parameters, it is necessary to determine the most crucial elements in the product as well as the environmental and loading conditions. Additionally, the feasibility and limitations of monitoring must be assessed, and the economic justification for the system monitoring must be provided. This stage also includes gathering data in the test setup and creating a database on healthy and failed behavior. Following this, the data is gathered in situ from the system in the real working conditions. The reduction, compression, and normalization algorithms should be used for effective data transmission and storage. The information may be stored locally or in a cloud, and from time to time it is sent to a maintenance station. After this, the data must be analyzed so that its important features can be extracted. This can be done in a number of ways, such as using statistical methods or calculating error functions. By correlating the data from the database and the current measurement of the system, the state of health of the system is assessed using methods such as neural networks or statistical classification. The algorithms used for the data correlation include particle filtering [40], Mahalanobis distance (MD) [41], SVMs [42], and wavelet decomposition [43]. If the information regarding the behavior of the system with different failures is available, the anomalies in the gathered data can be detected and the fault can be identified. Additionally, by observing some trends and features of the data, a RUL can be calculated.

This methodology was used in [44] to detect failures in automotive engines. In the study, the signals from different sensors were used to detect and classify the fault. The preprocessing of obtained signals was conducted using a wavelet method, which enables significant features extraction from the data collected

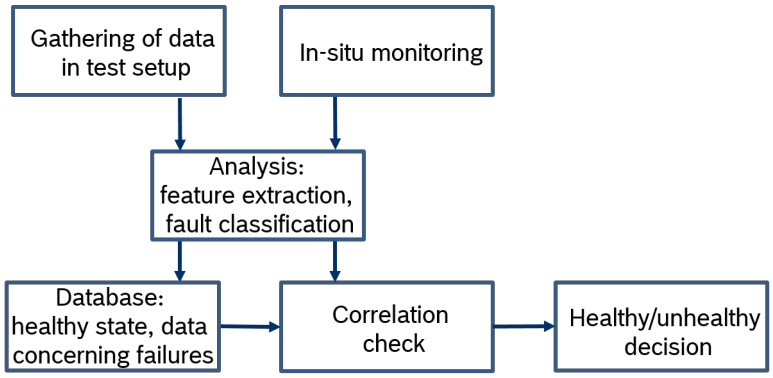

Figure 2.4.1: The procedure of data-driven prognostics.

in various engine operating conditions. The wavelets capture transient pre- and post-failure characteristics very efficiently. Afterwards, pattern recognition techniques were used to isolate the failure. In addition, the fault diagnostic matrix was constructed, which can be used to classify a fault based only on the wavelet coefficients derived from sensor signals.

Another approach to a failure prediction of an induction motor was investigated in [45]. In the study, the current spectrum of a motor was chosen as a monitored signal because it depends on the vibration of a motor. Thus, the spectrum can be used to identify a mechanical fault. An additional advantage is the low cost of this solution, as it does not require any additional sensor use. However, the current spectrum also depends on the current load of a motor. Hence, a data processing method based on the neural network approach was developed in the study. This method is able to detect anomalies in the signal that are not caused by loading condition changes. The methodology was tested using experimental data gathered from different motor types and was proven to be effective. Furthermore, the developed monitoring system was installed in various fields, such as in an oil refinery. The system was able to detect the fault of the motor when an inlet to a water pump was blocked because of a clogged filter.

A data driven approach was also used in [46] for enterprise servers prognostics. The investigated system was monitored using an established monitoring method called a continuous system telemetry harness (CSTH), which was developed by Sun Microsystems. The CSTH allowed the gathering the information not only on hardware and software performance but also on the physical conditions in which the system works, such as the temperature and humidity. The first step of data processing consisted of establishing the statistical distributions of measured parameters. Then, the data was processed with the multivariate state estimation technique (MSET) and the sequential probability ratio test (SPRT). MSET was designed to analyze the complex systems that identify the correlations between different parameters. In a training phase, it created empirical models for every monitored parameter that were used for estimating the expected behavior of the system for every observation time. Afterwards, the predicted and measured state were compared, and the difference between them was provided to the SPRT algorithm. The SPTR then checked whether the difference between the actual and forecasted states of the system was statistically significant and if the needed alarm was raised.

Other applications of a data-driven approach include specific electronic components prognostics [47]-[49], process control [50], avionics and space application systems prognostics [51]-[53], telecom systems prognostics [54], nuclear structures, systems and components diagnostics [55], industry maintenance [56], and many more. A common point for the approaches presented in the literature is that they are based on the monitoring of high level performance parameters. The piezoresistive stress sensor used in this work allows to monitor the structural health of the ECU based on mechanical stress measurement, which is directly related to the mechanical fault.

2.4.1 Monitoring

With a data-driven approach, the monitoring methodology is different than in the physics-of-failure approach. Here, the direct monitoring of loading conditions is of less importance. The monitored parameters should be chosen based on their value as a damage indicator. The parameter can be a voltage or current signal that shifts over a lifetime of a product, or vibration signature in case structural damage occurs; it can also be high level performance parameters (e.g., user wait time or the number of executed operations per minute) or other parameters related to the performance of a product. The physical working conditions such as the temperature of the device, ambient temperature, or relative humidity may also be measured, but this is done mainly to correlate the working conditions with monitored signals. In many cases, the characteristics that are already monitored in the system can be used. This reduces the cost of developing such a system, namely by the cost of additional sensors. The advantage of the piezoresistive stress sensor investigated in this work for PHM is that its signal can be used for both load monitoring for the model-based approach and performance monitoring for the data-driven approach. The values measured by the sensor are also directly related to the damage and can thus provide a more accurate evaluation of SoH of the system.

2.4.2 Database creation

A database containing information on the healthy behavior of a system must be created to train the data driven algorithms. As mentioned before, it should take into account the fact that the response of the system is usually strongly dependent on the operating and environmental conditions. Moreover, the variability that exists between different products of the same type should be taken into account. In the cases, when it is desired not only to predict failure but also to classify the failure, a database containing information on system behavior under different failure modes must be established.

The data acquisition can be done during the development stage of a product, which takes place typically during reliability testing. In cases where historical data is available, the data can be used for training. It should be noted that the patterns and trends present in the data can actually be generalized for the same type of product. However, the exact training data should be gathered in the specific system that the methodology is developed for, given that the data characteristics may differ. In some cases, it is also possible to use the data that is measured at the beginning of the product lifetime as healthy data. The training datasets for the damage detection algorithms implemented in this work are discussed in Chapter 7.

2.4.3 Data analysis

As mentioned before, a large variety of numerical methods for the data-driven approach are available. They are generally divided in three groups: statistical methods (e.g., chi square test and Bayesian classifier), machine learning techniques (e.g., neural networks and decision tree classifier), and supervised classification methods (e.g., particle filtering and fuzzy c-classifier method) [3]. For this present study, the methods implemented are MD, SVD, and SVMs. A brief description of each of these methods along with examples of its applications is presented in this subsection.

Mahalanobis distance

MD is a statistical pattern recognition method that is able to identify the data groups that show anomalous behavior. It calculates a distance in a multidimensional space while taking into account the correlation between parameters. It requires a database of healthy states to create a reference correlation matrix. It can be used for an efficient monitoring of a multidimensional system state. The main advantage of this method

is that it does not require prior knowledge concerning the failures in the monitored system. This means that the only thing needed to implement the algorithm is the healthy baseline, which in principle can be created based on the initial measurements in the system. Another advantage is that this method does not reduce the data dimensionality, preserving all the information. The fault identification is possible when the relation of MD values with different failure types is established. Additionally, the calculation is performed based on normalized data, which eliminates the problem of scaling. Other advantages of this method include good accuracy and easy implementation, but the method can be affected by masking effects. This algorithm is discussed in greater detail in Chapter 7.

The MD approach has been widely used in the literature for the diagnostics and prognostics of different electronic devices and systems. Some of the application examples are described in this subsection.

The studies in [41] and [57] have developed the MD approach with probabilistic determination of warning and fault detection threshold. The presented method was illustrated with an example of health state monitoring for a commercial notebook. Multiple performance parameters were recorded in situ, such as fan speed, CPU temperature, motherboard temperature, and the percentage of CPU usage. The data was gathered under different environmental and loading conditions; such conditions include various humidity environments, at various temperatures, and with different power supplies. The investigated conditions have exceeded the manufacturer's specified range in order to produce data on overstress operation. Based on the gathered data, a healthy baseline was constructed. Two types of threshold values were determined—one general threshold value for a system level failure detection and individual thresholds for specific failures. The methodology has been tested using both training and test data. The two studies have confirmed that this method is suitable for fault identification based on multi-parametric data.

Another example of MD implementation is presented in [58], where the damage in solder joints caused by mechanical shock and vibration was investigated. The data concerning strain evolution during controlled impact were used as input for the method. The tests were performed according to JEDEC standards. The data for training and testing the algorithm were gathered by both FEM simulation and in experiments. The local strain values were gathered experimentally by strain gages, and a full field strain was recorded using a digital image correlation technique. The transient strain signal was used as a health indicator. Both fast Fourier transform (FFT) and time frequency analysis (TFA) methods were used for feature extraction. After this, three different statistical pattern recognition techniques were used for health state assessment, namely the techniques of MD, wavelet packet energy, and joint time frequency analysis. All of them could detect progressing failure and showed similar performance.

The studies in [59]-[60] investigated the MD approach for the health monitoring of a light emitting diode. First, the useful life of a LED was defined according to the recommendations given by the Alliance for Solid-State Illumination Systems and Technologies (ASSIST); specifically, it was defined as the time until the 30% decrease in light intensity of a device. Then, the parameters for monitoring during experiments were defined. Since current through the p-n junction and the p-n junction temperature are known to be good performance indicators, it was decided that these parameters would be monitored. The failure of a diode was captured using a light detector, with an output proportional to the light intensity. The training and testing data were gathered during the accelerating of lifetime testing. After this, the Euclidian and MD approaches were applied. Both of them successfully detected the impending failure based on measured parameters. Additionally, the studies noted that the light intensity of a LED decreases linearly at the end of the lifetime. This enabled a lifetime model formulation and consequently RUL prediction based on monitored values.

In [61], the health monitoring methodology based on MD was implemented for a hard disk drive (HDD). The major failure modes of HDDs were identified and prioritized. It was established that the head disk interface causes usually most of the reliability problems. Then, the parameters to monitor were determined. In the case of HDD, the monitoring technology already exists and is established on the market. It is called S.M.A.R.T. (which stands for Self-Monitoring, Analysis and Reporting Technology), and it enables

monitoring of such parameters, such as head flying height, data throughput performance, spin up time, and re-allocated sector count. The existing signal processing is based on threshold methods and shows low detection rate. Therefore, a more robust approach to data evaluation was investigated. The authors proposed a method based on MD calculation. The performance of the method was evaluated based on data gathered from a large sample of healthy and broken hard drives. Two versions of algorithm were tested—one took into account all monitored parameters, and the other only considered the parameters that are relevant in a head disk's interface reliability issues. It was shown that considering a smaller number of parameters leads to a better failure prediction performance (i.e., a lower false alarm rate and failure detection rate).

Numerous further examples of MD use in health monitoring can be found in [62]-[67]. In the presented examples, the developed PHM approaches are based on high level performance signals. That means that the failure can be detected only after the system performance started to deteriorate. In this work, MD applied as the damage detection algorithm is based on the stress pattern on the surface of the measurement chip. Thus, the developed methodology has the potential to detect structural fault in the system in situ before the system performance is affected.

Singular Value Decomposition

Singular value decomposition (SVD) is a discrete version of the algorithm known as proper orthogonal decomposition (POD). It is a multi-variate statistical method for data analysis. Its primary use is order reduction as it enables the projection of high-dimensional data into lower dimensional space [68]. It also enables feature extraction from the data by unveiling its structure. The main idea is to decompose the matrix into a product of two orthonormal matrices and one containing the singular values of the original matrix. When the investigated matrix contains data with damage, the calculated decomposition components are different from the ones calculated only with data from intact structures. The detailed description of this method is provided in Chapter 7. This method is widely used for damage detection, especially for structural applications based on vibration data. Some examples of SVD implementations from literature are presented in this section.

In [69], the POD method was applied to damage detection in the composite antenna structure for avionics applications. The signal which indicates failure was the vibration spectrum gathered by piezoelectric elements. The SVD method was used to find the proper orthogonal modes and values from the gathered data. In the study, it was shown that the structural damage changes the structure of a data matrix, consequently affecting its proper orthogonal modes. The damage index was defined as an angle between the healthy and tested subspace, which is a product of matrix decomposition. A detection threshold was defined based on normal distribution statistics within 95% confidence intervals. The proposed approach was tested using two kinds of data containing damage, namely a structure with impact damage and a structure with an additive mass. The study showed that the developed approach was efficient in damage detection with no false alarms.

Another approach to damage detection using SVD based on vibration spectrum is presented in [70]. The introduced method should be applicable to the structure of arbitrary complexity. Additionally, the method should be able to distinguish between the vibration spectrum changes caused by damage and those caused by different loading conditions. This method was based on determining a rank of the matrix that contains characteristic vectors of a structure that are defined for different loading conditions. The characteristic vector could consist of data such as natural frequencies, mode shapes, frequency response functions, and transmissibility. Next, the data measured in situ was placed in the last column of such a matrix. The study demonstrated that the rank of the matrix remains unchanged if the measurement data corresponds to a healthy state and grows if the structure is damaged. In the proposed approach, the rank of a matrix was estimated using SVD algorithm as the number of singular values that are larger than measurement noise. The proposed methodology was tested using two sets of data—data from the simulation of a truss structure and data from cantilever beam measurements. Different working conditions were investigated using

different mass conditions, both in simulation and measurements. In the simulation, the structural damage was modelled as the change in the structure stiffness; in the measurements, different sized indents were cut in the beam. In both cases, the damage was detected with satisfactory efficiency.

Further examples include fault detection in industrial manufacturing processes [72]-[74], engines of various applications [75]-[77], and power electronics [78]-[79]. In the present study, the SVD algorithm is tested to verify whether it can be used for structural fault detection with a completely different type of data—stress distribution on the surface of a chip.

Support Vector Machines

A support vector machine (SVM) is a machine learning algorithm that can solve classification problems. It was introduced by Vapnik in [80]. Its main advantage is that it can form accurate boundaries between datasets even with small amount of training data [81]. Additionally, it often provides a good generalization and finds a single global minimum for a problem. The basic idea behind it is to locate the plane separating the distinct datasets in such a way that the distance between the datasets is maximized. When input data sets have n-dimensions, the algorithm search for an n-1-dimensional hyperplane that separates them. This hyperplane can constitute linear or non-linear boundary. A more detailed description of the algorithm can be found in Chapter 7. This algorithm is widely used for damage classification. Examples of SVM implementation are presented in this section.

In [82], the SVM method was investigated for fault classification in an induction motor. Three different parameters for fault classification were studied—the stator line current, currents circulating between parallel branches of a motor, and the force on a rotor. Multiple failure modes were considered; these include a shorted turn or a shorted coil in stator winding and a broken rotor bar. First, data concerning behavior of a motor under these failure modes were gathered using simulation approach. The SVM algorithm was performing best when trained with the force on the rotor and circulating current data. The classification based on the stator current data was not explicit. Additionally, the data from an experiment was gathered. In this case, the SVM algorithm was able to classify correctly all investigated failure modes based on stator line current measurements.

In [83], the SVM algorithm was used to detect faults in analog electronic circuits. Three health states were defined—healthy, sub-healthy and failed. The classification should be done between these three classes for the data concerning different faults. Additionally, a method for health degree estimator calculation based on the distance of an investigated point from the respective data sets was presented. This parameter could be used to estimate whether the component would change its class soon. The proposed approach was tested on data gathered by simulating a voltage regulator circuit. The mean value of the voltage and ripple coefficients at the outputs of the circuit were chosen as monitored values. The tolerances of parameters of the used components were taken into account in healthy state data collection. Then, the faults of different severity were inserted. An analysis of the gathered data has shown that the proposed approach qualified the state of the system properly in 80% of the cases.

In [84], a comprehensive approach to fault identification in a gearbox by means of SVM was proposed. The developed method used a vibration spectrum of a gearbox as a damage indicator. Before training the SVM algorithm, the input signal was preprocessed to extract the data features. First, a time domain averaging was applied in order to filter the noise. A wavelet packet decomposition method was then used for the feature extraction. Next, the data was normalized and its dimensionality was reduced using a principal component analysis algorithm. Additionally, the study recognized a great effect from the SVM algorithm parameters on the algorithm behavior. The identified parameters were the penalty parameter in the optimization formulation and the constant in radial basis function kernel. Thus, they were optimized using the particle swarm optimization (PSO) method. The proposed approach was tested with two sets of data, namely the

theoretical and the gathered data in an experiment. The investigated failure modes included a broken tooth, cracks, and wear-out. The proposed approach correctly classified over 90% of the failures from the data gathered under different load conditions. Additionally, it was demonstrated that without the preprocessing, the same algorithm showed much poorer performance.

Another prognostics and health monitoring method using SVM algorithm for automotive applications was proposed in [85]. The developed system consisted of a number of components, namely 1) a communication module in a car, 2) a smartphone that establishes connection between the car and service center, and 3) the logistics, maintenance and emergency centers. Every element of this system had different tasks—from gathering the systems performance data through data analysis and health estimation, to maintenance action scheduling and organization. The presented system did not require any additional hardware installation; it could use the signals from sensors already available in a car. The proposed prognostics algorithm is the least squares SVM (LS-SVM)—a time optimized version of classical SVM—which is suitable for real-time calculations. The healthy and failure data for training should be provided by the reliability experts. Four classes of health state were proposed: healthy state, 40% RUL, 10% RUL and failure. The approach is tested with the data from transmission control unit. The monitored parameters included revolutions per minute, vehicle speed, and gearbox temperature. The training database was constructed based on expert knowledge; the proposed approach was effective in the correct classification of a system health state. Additionally, the performance of the SVD algorithm for this problem was compared with this of k-nearest neighbor classifier method. The LS-SVM algorithm was not only more accurate, but it also demonstrated a higher degree of specificity and sensitivity.

Some further applications of the SVM technique include avionics [86]-[87] and spacecraft prognostics [88], battery lifetime prediction [89], and nuclear power plant diagnostics [90]. In this work, the SVM technique is investigated for a structural fault classification based on the stress sensor signal.

2.5 Fusion approach for prognostics

The basic idea of a fusion approach for prognostics is to use both model and data-driven approaches, since they complement each other and limit each other's deficiencies. The concept was introduced in [91] by Zhang et al. It reduces the uncertainty in system damage prediction and takes into account both normal loading conditions and anomalies.

A workflow of a fusion PHM approach is presented in Figure 2.5.1. It starts with the definition and analysis of an investigated system, usually using a FMMEA method. It allows for the definition of the critical components of a system, the expected failure modes and their models, as well as the parameters to monitor. The monitored characteristics should include both operational loads and performance parameters of the investigated product. The gathered data is processed further in two ways. First, the RUL is estimated based on an established physics-of-failure model and the environmental loads measurements. Additionally, the performance parameters are compared with the database in search for anomalies and trends that could indicate damage progression. The detection of product degradation by a data-driven algorithm leads to the update of an established failure model for more accurate failure prediction. In such a way, a data-driven approach is utilized to adjust the PoF model. On the other hand, the PoF model can be used in this methodology to determine thresholds and failure criteria for data driven algorithm. This improves the accuracy and efficiency of RUL prediction.

This method is especially well suitable for a system level prognostics. The components degradation can be monitored based on their performance parameters. When an anomaly is detected, the degrading component can be identified and matched with a specific failure mechanism. A PoF model can then be determined and used for RUL calculation. This enables an accurate and efficient identification and assessment of a damage accumulation and progression on a system level.

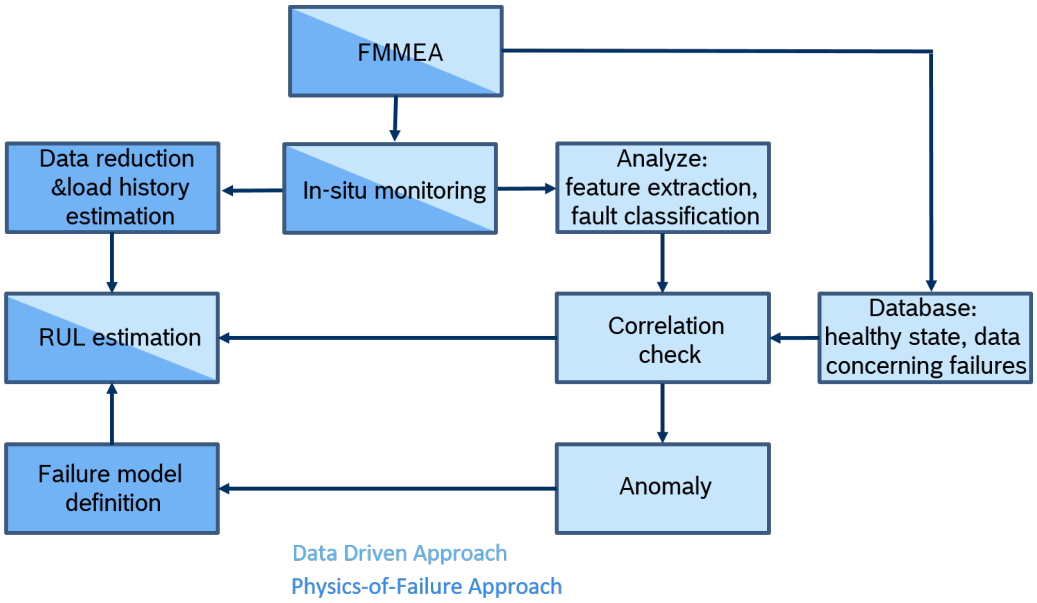

Figure 2.5.1: Procedure of fusion prognostics.

This is a relatively new concept, but it has already gained much popularity because of its obvious advantages. Some implementation examples of fusion approach to PHM are described further in this section.

An early example of this method implementation is presented in [92], which showcases a physics-of-failure model that was implemented to predict the RUL of a helicopter gearbox. This model calculated the probability of failure as a joint probability of crack initiation and propagation. It was created based on detailed FEM modelling results used for extracting strain values that act on the design elements, and accelerated reliability tests to determine the constants present in a lifetime equation. The model was updated only to take into consideration the probability of a critical crack propagation when a crack has been detected in the tested structure. The system state was monitored using its vibration spectrum.

An implementation of fusion prognostics methodology for solder joint failures prediction in digital electronics is presented in [93]. The physics-of-failure model was based on inelastic strain range as a damage parameter and was used along with Miner's rule for damage accumulation estimation. To implement a data-driven approach to consider prognostics uncertainties, an uncertainty adjusted prognostics (UAP) method was developed. The in-situ measurements for temperature as well as the resistance in a daisy chain of different type of packages were taken as inputs to the algorithm. Historical data concerning failures were provided and were further utilized to estimate the RUL using extrapolation techniques. A database of possible kernels for fitting was given in order to achieve the best possible prediction quality. The uncertainties in RUL prediction were calculated based on goodness of fit. The RULs computed using both approaches were then combined using the transferable belief model (TBM) as this method does not require knowledge on probability distributions of the respective RUL estimates. The proposed approach was tested using thermal cycling data with an irregular load profile in order to simulate field conditions. The study showed that a fusion of both data driven and physics-of-failure techniques improved the performance of lifetime prediction methodology.

Another implementation is proposed in [94] for multilayer ceramic capacitors (MLCCs) under thermo-mechanical loading and humidity exposure. Two main failure mechanisms were identified, namely silver migration—which can cause short circuit failure—and degradation of dielectric material, which results in lowering of insulation resistance. The insulation resistance, capacitance, and dissipation factor were chosen as parameters to be monitored. A sample of capacitors were subjected to reliability testing, and some of them failed. The healthy baseline was constructed based on data gathered from capacitors that survived the

tests. The study then used a MSET technique to calculate the residual between the predicted and actual states of a component. Moreover, a SPTR method was used for anomaly detection. When an anomaly was observed, the failure mode could be identified based on a previous analysis of possible damage mechanisms. In this way, a PoF model could then be applied to calculate RUL. In the presented approach, the PoF model was created for silver migration based on testing data. The proposed methodology was able to predict the end of a lifetime before the failure occurred.

In [95], a fusion approach to lithium-ion batteries prognostics was presented. The physics-of-failure methodology was established using the exponential capacity fade model. The largest uncertainty in the predictions of this model was introduced by the inaccurate estimation of parameters, as they depended on a sample variation, as well as differences of operational and environmental conditions. Thus, a method to update the model parameters in the real time was proposed. For this purpose, the last n measurements were stored and used for an in-situ parameter optimization using the Levenberg–Marquardt method. A particle filtering technique was then used to estimate the distribution of capacity values calculated with the updated model, and the RUL was assessed. This approach was tested with four sets of data coming from different battery types and with different aging behavior. The study found that the developed approach which combined data-driven and model-based methodologies was more effective in predicting the battery lifetime than pure data driven algorithm.

The examples of fusion approaches found in literature, similar to the cases of model-based approaches and data-driven approaches, are mainly based on the environmental load measurements or high level performance parameters. Additionally, in most of the cases the applicability of the measurement techniques in field conditions were not considered. The main advantage of the fusion approach developed in this work is that it can be realized using one sensor that can monitor both the load in the system and its structural health. The use of a novel sensor is the main reason why this work goes beyond state of the art.

2.6 Summary

Most of the presented examples of the implementation of PHM methodology focuses on development of PHM based on signals that can only be indirectly related to the failure (i.e., performance parameters or external loads such as temperature or vibration). In some cases such as in [19] or [92], the mechanical load acting on the monitored design element is calculated based on external load measurement and numerical models. In [58], a methodology based on strain measurement during shock and vibration loads was proposed, but in practice it would be impossible to use DIC technique to measure strains in the field. This work fills a gap in PHM research because it concerns the applicability of a piezoresistive stress sensor to the ECU level monitoring. The main advantage of this sensor is that it can directly measure the mechanical stress that act upon the electronic system. The mechanical stress can be related to both load and damage in the electronic system; hence, a fusion approach for prognostics for ECU can be developed based on stress sensor measurement. The established methods and algorithms used in PHM fields—such as FMMEA, Miner's rule, MD or SVM—are adapted in this research. This work goes beyond the state of the art because of the system level application of piezoresistive stress sensors to PHM.

Chapter 3

Investigated system

3.1 Electronic control unit

The system investigated in this thesis is an electronic control unit (ECU) that was developed for automotive applications. In a modern vehicle, there are multiple control units, such as units for engine control, transmission control, and steering control (see Figure 3.1.1). The use of electronics in automotive applications brings in many advantages; some of these include the enhancement of on-road performance, the improvement of fuel consumption, the reduction of exhaust gas, and the extension of battery life.

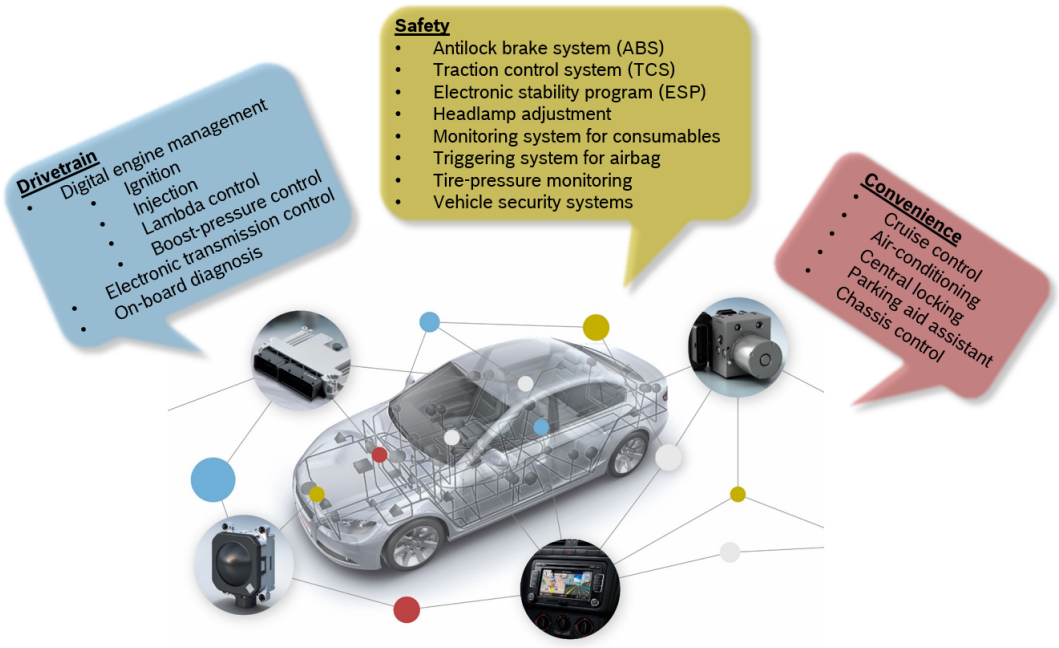

Figure 3.1.1: Overview on electronic modules used in a modern vehicle [96].

An ECU is a complex electronic system that integrates a large number of electronic components. It is mounted under the engine hood where it is subjected to harsh environmental conditions, such as temperature changes and vibration. Reliability is one of the most important issues as an ECU module is directly related to vehicle safety. For this reason, a significant amount of time and effort has been dedicated to develop reliable devices. A common way to protect the electronic module from its environment is to use a metal case

(a) (b) (c)

Figure 3.1.2: ECUs with and without cases. (a) ECU without a case. (b) ECU encased in a metal case. (c) ECU encapsulated by epoxy molding compound (EMC).

as depicted in Figure 3.1.2(b). Such a hard case would not only protect the module from chemical loads and impact damage but also minimize electromagnetic interference (EMI) problems. However, this technology is rather expensive. Thus, a transfer molding technology has been adopted instead to protect the ECU. An example of an overmolded ECU is shown in (c) of Figure 3.1.2. At present, the epoxy molding compound (EMC) can be obtained at a low cost, which is an advantage; moreover, the EMC ensures protection of the module from a harsh environment. It is especially effective against vibration and chemical loads.

However, the outer mold introduces some additional mechanical stresses on the ECU. First, chemical curing shrinkage occurs during the molding transfer process; this shrinkage is caused by the cross-linking of a polymer. The EMC volume decreases due to curing shrinkage, and the module deforms accordingly, as shown in (a) of Figure 3.1.3. Moreover, due to a CTE mismatch between the EMC and other materials present in the system, additional thermo-mechanical stresses are introduced, as shown in (b) of Figure 3.1.3. These issues create additional reliability challenges, which are investigated in this thesis.

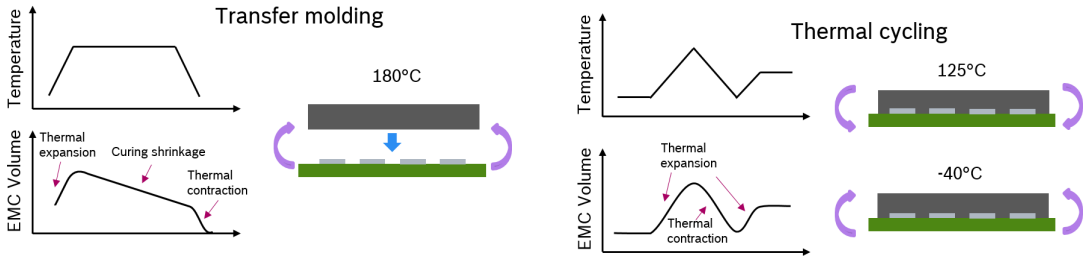

(a) (b)

Figure 3.1.3: Mechanical stress in ECU is caused by (a) curing shrinkage and (b) CTE mismatch [12].

3.2 Investigated package

In this investigation, the package of interest is the DPAK (Discrete Package). It is an SMD power package that has excellent current handling and thermal dissipation capabilities. It is widely used to encapsulate power transistors, such as MOSFETs and IGBTs.

Figure 3.2.1 shows the DPAK package and its components. In this package, a semiconductor die is soldered onto the copper-lead frame. The top terminals of the semiconductor device are connected to external pin bars by a metal wire bond. The whole construction is overmolded using EMC.

The device in the DPAK package investigated in this thesis is an IGBT transistor. IGBTs are high voltage power devices that are able to operate with a very high current density. They have a high peak current capability, good ruggedness, and simple gate drive requirements [97]. Additionally, they are fast like power

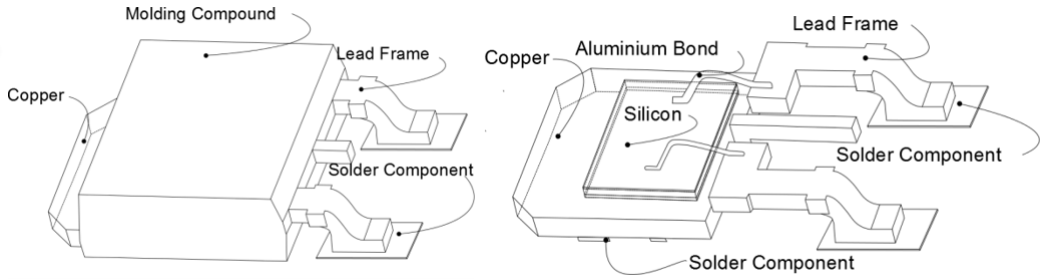

Figure 3.2.1: DPAK package.

MOSFETs, and they have low conduction losses, much like bipolar transistors. This makes them suitable for a wide range of switching applications. The investigated device is used as an automotive ignition switch. The current IGBT technology ensures good power dissipation and switching speed for this application.

The ignition system in a car uses an inductive discharge. The basic structure of an ignition circuit consists of a control unit, a drive circuit, an ignition IGBT, a coil, and a spark plug (see Figure 3.2.2) [98]. The control unit consists of a processor that creates a timing signal for the drive circuit. The signal timing is optimized in order to save fuel, limit emissions, and maximize power efficiency given instantaneous engine speed, temperature, and torque. The drive circuit is a simple amplifier that turns the IGBT switch on and off, which in turn controls the energy delivered to the ignition coil. Switching of current in the ignition coil causes an abrupt change in the magnetic flux in the ignition coil. According to the Faraday's law of induction, this generates a large over-voltage pulse that is used to create an ignition spark.

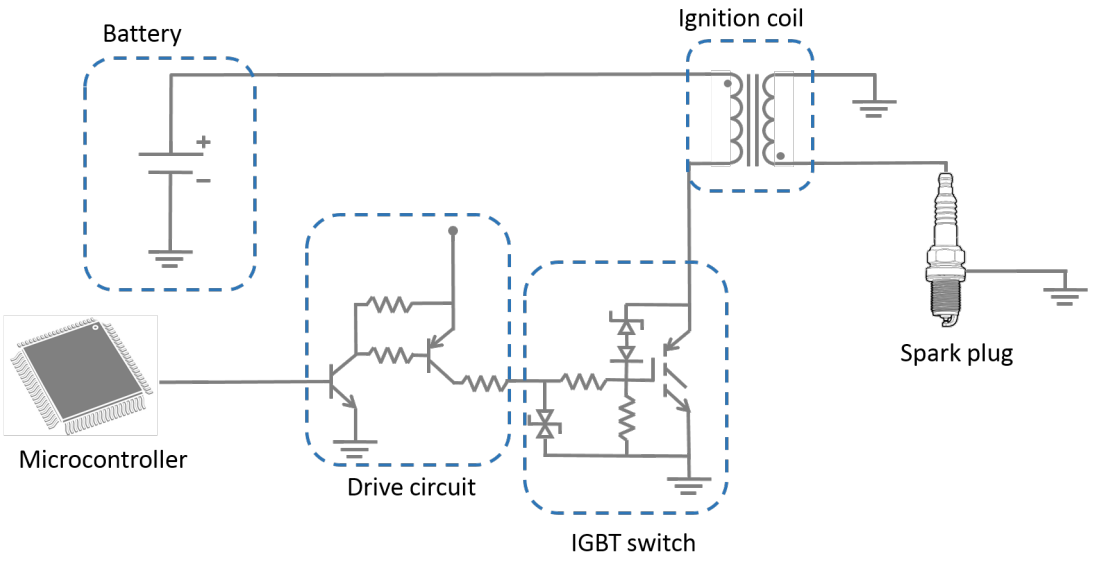

Figure 3.2.2: General scheme of the inductive discharge ignition system[98].

Thus, during the operation of the ignition system a large amount of power is dissipated in the DPAK package, which then causes the local temperature to rise. The temperature gradients are created, consequently provoking thermal strains even within the same material. This creates a much more complex stress situation, where in addition to the stresses introduced by the mismatch of thermal expansion coefficients in different layers, the stresses within the same material exist. Hence, a careful analysis is needed in order to assess the proper reliability.

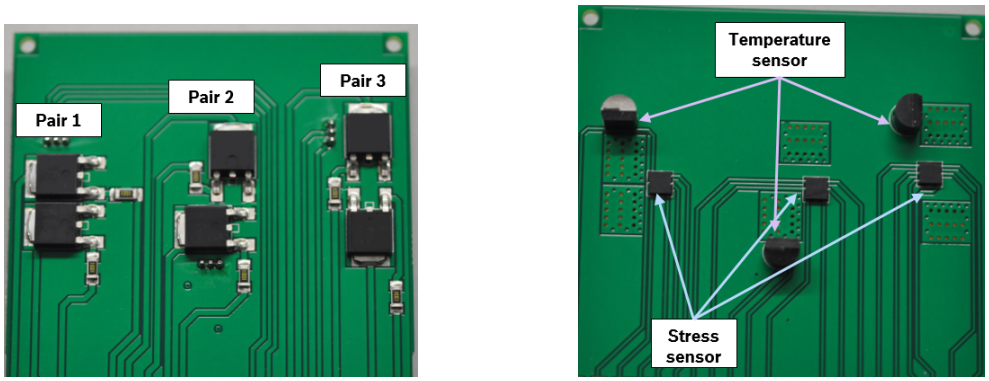

(a) (b)

Figure 3.3.1: Test vehicle a) top view b) bottom view.

3.3 Test vehicles

For this study, a special set of samples based on a construction of an overmolded ECU product has been manufactured as shown in Figure 3.3.1. They will be referenced to as test vehicles. It is an ignition control ECU that is using DPAK components as the IGBT switch. Exactly as in the product, the test vehicle is an overmolded structure with four full copper-layered PCB containing six DPAK packages. The packages are placed in pairs at three different positions on the PCB; two pairs are located along the edges of the PCB. The DPAKs within these two pairs have different relative orientations and the orientation toward the edges of the PCB. Pair 1 is placed next to each other and perpendicularly to the edge of the PCB; Pair 3 is placed parallel to the edge but against each other. Pair 2 is located in the middle; one of the DPAKs is rotated by 90°toward the other. The goal of this design is to investigate the influence of the orientation of the package on the internal stress state. In addition, the test vehicle can be used to study the effect of orthotropic properties of the PCB caused by a different amount of glass fibers in the ply in x- and y-direction of the PCB.

During the active cycling condition, a power of 1.2 W is dissipated in every DPAK package to reproduce the real loading situation in the product. To dissipate the heat effectively, thermal vias are placed on the PCB directly under the power packages according to the product design. The passive thermal cycling experiments are performed according to product requirements (i.e., between -40°C and 125°C). The mechanical fixation of the test vehicles during reliability testing also corresponds to the field use case, and it is of a free expansion type.

Figure 3.3.2: Overmolded sample.

On the other side of the PCB, three piezoresistive stress sensors are placed underneath each DPAK pair where the highest temperature during active operation is expected (see Figure 3.3.1(b)). These are the locations where the largest load occurs during reliability testing, and thus the failure is likely to occur there

first. Hence, it is the main region of interest, since the ultimate goal is to detect the failure that occurs in DPAK package. The stress sensors are to be used for feature extraction, from which the state of health of the control unit is estimated. The sensor chip size is much smaller than the size of the monitored DPAK package. A larger sensor would have a better sensitivity and would be able to detect potential structural faults in the larger area. However, the small sensor used here has a particular advantage in that its stiffness does not have a significant influence on the stiffness of the system. Increased local stiffness could lead to an earlier failure in the system.

In addition to the stress sensors, three temperature sensors are used for in-situ temperature measurements, which is critically required for an active operation of the designed test vehicle during active power cycling.

The test vehicles are produced in bare PCB and overmolded version. The overmolded sample is shown in Figure 3.3.2. The outer mold protects the module from harsh environmental conditions. It is produced in a separate molding process and has a significant influence on the thermo-mechanical behavior of the module. Investigation of both bare PCB and overmolded samples enables analysis of the influence of outer mold on the system reliability.

Chapter 4

Piezoresistive stress sensor

4.1 Introduction

As mentioned, this thesis investigates how a piezoresistive silicon-based stress sensor can be a possible tool for implementing PHM methodology. To reach this goal, it is imperative to overcome the challenges posed by the measurements with this sensor.

First, it is necessary to design a new measurement system that enables measurements with multiple sensors at a time [99]. To achieve this goal, this study constructs a system that is able to gather the data from eight sensors at a time. Additional advantages of the designed solution is mobility, flexibility, and capacity to store a large amount of data.

Next, it is crucial to understand the measurement uncertainties. Extensive analytical and experimental analyses were performed in this work based on both theoretical and experimental data. The uncertainties were evaluated at different complexity levels. The investigated samples included:

- a sensor glued onto a LTCC
- a sensor encapsulated in a 3x3 mm LGA package
- a sensor encapsulated in a 3x3 mm LGA package soldered onto a PCB
- a sensor encapsulated in 3x3 mm LGA package soldered onto a PCB and overmolded

In this study, possible sources of calculation errors were identified, such as in cases where the piezoresistive coefficient depended on temperature and on measurement current. After this, a thorough analysis of the systematic errors present in the measurements was conducted. The analyzed errors resulted from the simplifications made in the stress calculation from measured currents. Finally, random errors were evaluated based on measurements performed on eight samples of each kind, and the uncertainties related to the measurement process were separated from the uncertainties related to the samples variability [100].

4.2 Potential

Piezoresistive stress sensors have continued to garner more attention, especially for high reliability applications. The main advantage of this type of sensor is that it measures mechanical stress, which is a parameter directly related to damage. Additionally, the sensor can be easily integrated within electronic systems as it consists of a silicon die and can be encapsulated in any microelectronic package.

A resistance-based sensor was initially introduced, but its applications have been limited due to its large size (about 300 µm times 300 µm), which additionally can affect the accuracy of measurement. The stress can be different in resistors throughout the rosette, and thus the measurement result is an average over the surface. The second limitation of resistive stress sensors is the need to have a reference measurement in a state without stress. Moreover, to have a reliable measurement results in various temperatures, a reference value is needed at every measured temperature [101]. This makes it impossible to use these sensors on a wide scale since characterizing every one of them is unpractical.

The CMOS-based sensors have been developed to cope with the critical limitation of the resistance-based sensor. They do not need calibration due to placement of transistors in current mirror configuration. Additionally, the measurement technique is simpler because the output signal is of a current type instead of resistance. Moreover, the sensitivity of the sensor is enhanced because of the light doping of silicon. The CMOS sensor also allows the stress to be measured in a localized manner. A single measurement cell has the dimensions of 50 µm x 50 µm; in practice, sensors with multiple stress-sensing cells on one chip are used. Furthermore, it is easy to integrate the sensing element with active circuitry. Multiplexers allow data acquisition from all of measurement cells.

The CMOS stress sensor has been used by various research groups. Jaeger et al. [102]-[108] made an analysis of CMOS stress sensor behavior in various measurement circuits. The sensor in a cascade current mirror configuration was produced, and an investigation was conducted on how the encapsulation process affects the stress in the package. The results of measurements were compared with FEM simulation to confirm the accuracy of the measurements. The group from Freiburg University IMTEK designed a CMOS stress sensor, which uses the pseudo hall effect in silicon for stress measurement. In their research, they characterized the sensor [109]-[111], created a matrix of cells with active circuitry [112]-[113], and used this sensor for monitoring of wire bonding process [114]-[115].

More recently, the possibility of using this sensor for PHM has been realized. In [116]-[118], Roberts et al. studied both the evolution of stress during packaging processes and thermal cycling reliability testing using a resistive type of stress sensor. They found that the stress changes rapidly at the beginning of cycling, and after this stage only minor changes are seen. In [119], Rahim et al. showed the changes of the signal of a stress sensor due to delamination. Similar results during thermal cycling have been presented in [120] and in [121]-[122]. In [123]-[124], Lall et al. observed the changes in stresses measured by the sensor at the point as delamination appears but only before the change could be detected by other available methods. From this, stress sensor measurement was identified as a possible technique to detect leading indicator of failure.

In the course of this thesis, a further investigation has been conducted concerning the potential application of a piezoresistive silicon stress sensor for PHM methodology at a system level. The stresses measured during both the thermal cycling of PCB-based ECUs and overmolded modules have been analyzed and compared [125]. The induction of the stresses during active thermal cycling was also investigated [125]. In [126], the evolution of stresses during reliability testing was presented. The time effects on the material behavior has also been studied [127].

4.3 Fundamentals of IForce sensor

The sensor used in this research is designed in CMOS technology. It means, that a pair of MOS transistors is connected into current mirror circuit (see Figure 4.3.1). The current mirror configuration forces the same current in both branches of the circuit as long as the parameters of both transistors match one another. The stress sensitive channels of MOSFET transistors in both branches of the current mirror are oriented at a different angle to the crystallographic axes of the silicon. Mechanical stress acts on the properties of these transistors in a different way, thus forcing the circuit out of balance. This effect can be measured as a

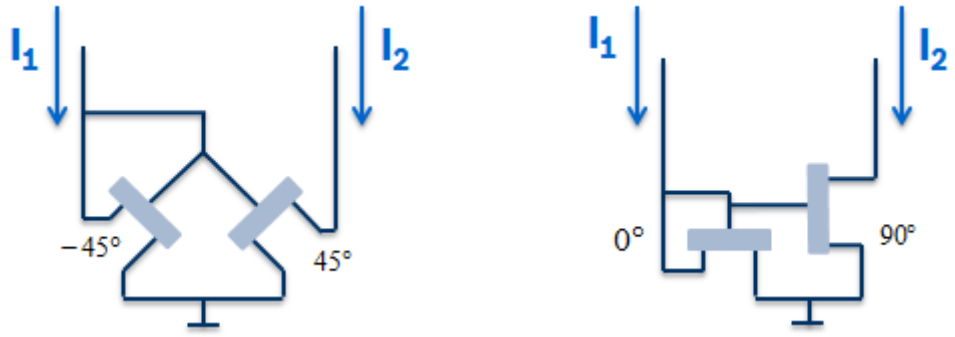

(a) (b)

Figure 4.3.1: Current mirror circuit used for stress measurement. (a) nMOS current mirror used for xy shear stress measurement. (b) pMOS current mirror used for difference in normal in-plane stress measurement.

difference in currents in both branches of the current mirror. Based on the current difference, the mechanical stresses acting in a circuit can be determined.

4.3.1 Basic formulas for stress calculation

There are two current mirrors in a sensor—one is of a p conductivity type, and the other is of an n conductivity type. This enables measurement of two stress components, namely shear stress in the xy-direction and a difference in normal in plane stress. The nMOS current mirror is used for calculation of an xy-shear stress, according to the formula [128]:

$$\sigma_{12} = \frac{1}{\pi_D^n} \frac{I_1 - I_2}{I_1 + I_2} \tag{4.3.1}$$

Where:
I_1, I_2 - currents in both branches of current mirror
π_D^n - piezoresistive coefficient of n doped silicon ($\pi_D^n = \pi_{11}^n - \pi_{22}^n$)

The pMOS current mirror is used for difference in normal in plane stress calculation, according to the formula [128]:

$$\sigma_d = \sigma_{11} - \sigma_{22} = \frac{1}{\pi_{44}^p} \frac{I_1 - I_2}{I_1 + I_2} \tag{4.3.2}$$

Where:
π_{44}^p - piezoresistive coefficient of p doped silicon.

The choice of type of conductivity (p or n) of channels of current mirrors was made in a way that resulted in possibly largest sensitivity to stress—the π_D coefficient is the largest in an n-type silicon and π_{44} is the largest in the p-type silicon. Table 4.3 shows the values of the relevant piezoresistive constants. (4.3.1)–(4.3.2) show that no reference current is needed. The calculations are made using the instantaneous current values. These equations will be derived and further discussed within the next sections of this chapter.

4.3.2 Basics of construction

Figure 4.3.2 shows the construction of a sensor used in this study. Each measuring cell contains eight transistor pairs; there are two pMOS and two nMOS stress sensitive transistor pairs, and these two current

mirrors have a different transistor orientations on the input. This means that for a p-type current mirror, one mirror has the input on the transistor oriented at 90˚and the other mirror at 0˚; for n-type mirrors, the analogical situation occurs.

The remaining transistor pairs are stress insensitive, and their channels have the same orientation towards crystallographic axes. In this case as well, there are two versions of current mirrors that have different orientations. These stress insensitive current mirrors were necessary at the early development stage of the sensor. They were used for obtaining the electrical characteristics of the produced devices in order to characterize their dependence on temperature independently of stress.

Additionally, in every sensing cell there is a bipolar transistor for temperature measurement. Having accurate information on the temperature is crucial because the piezoresistive constants are dependent on temperature. This effect and its influence on the measurement uncertainties is discussed in greater detail in further sections of this chapter.

This configuration that consists of a set of eight MOSFET transistor pairs combined with the bipolar transistor is referred to as a single measurement cell in this thesis, as depicted in (a) of Figure 4.3.2. It can be seen, that in one sensor there are multiple measurement cells. As shown in (b) of Figure 4.3.2, the sensor considered here has 12 measurement cells placed in a 4x4 matrix; cells in the corners are inactive, because the place is needed for bonding pads. The exact die used in this work consists of two sensors (see Figure 4.3.2(c)). For the sake of simplicity, only the results gathered from one of the sensors are presented in here. This can be done without any information loss since the stress distribution in the cases considered in this thesis is close to symmetrical along the y-axis.

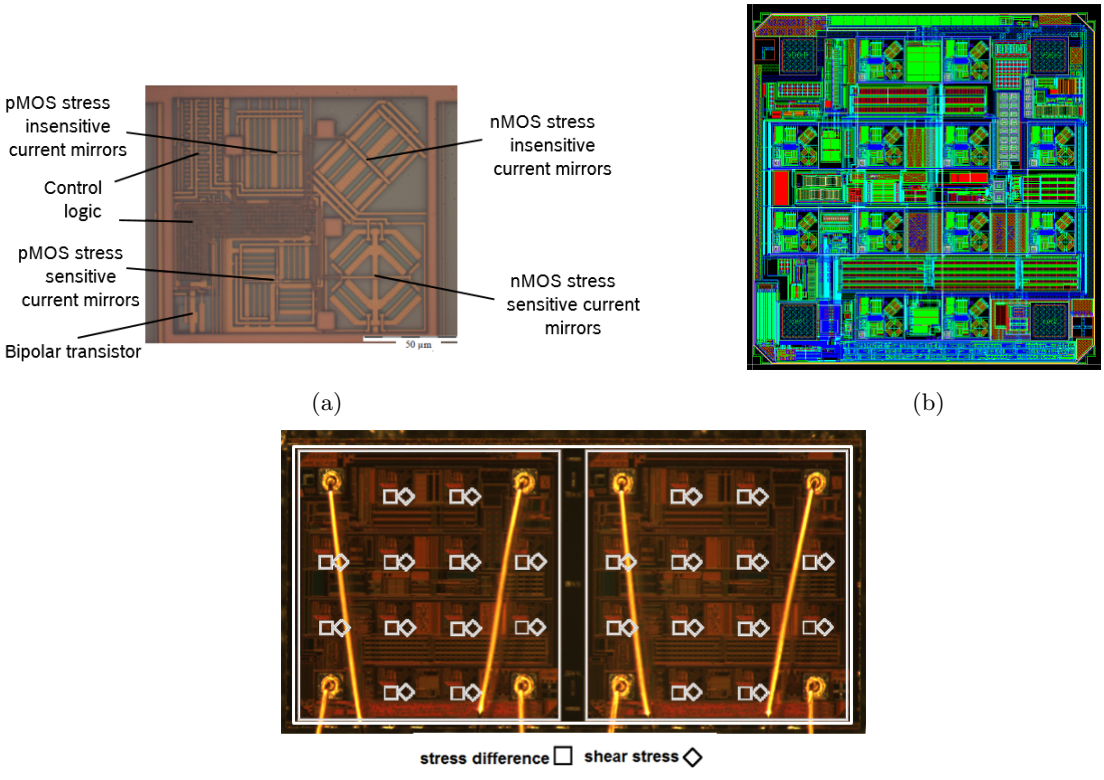

Figure 4.3.2: : Construction of a sensor. (a) The single measurement cell. (b) Cells placed in a matrix, creating a chip. (c) Configuration used in this study, consisting of two 4x4 sensors with exact places of measurements marked.

4.3.3 Communication protocol

The chip used in this work was developed in a project founded by the German Federal Ministry of Research and Technology; the project focused on the characterization of the stress induced during encapsulation process [129]. This chip was designed in such a way that enables adaptation of both the size and shape of the silicon die to the investigated package. It is possible to cut the dies containing multiple sensors from a wafer and encapsulate them within one package; it should also be noted that a sensor consisting of two separate devices is used in this thesis. This process produces the proportional growth of the number of pins that is necessary for measurements. To minimize the number of used pins within one device, a custom communication protocol with a sensor was developed. The communication is done over power supply terminal, both by current and voltage modulation. There are four pins per device: ground potential terminal (GND), power supply (VDD), and two current measurement pins labelled CUR1 and CUR2.

The measurement sequence of one cell consists of 17 measurement phases. During first four phases, the NMOS current mirrors are measured. First, the stress sensitive mirror is measured in a forward and backward configuration; it should be noted that the input terminal is changing at this time. Then, the same is conducted for stress insensitive current mirrors; the following four phases correspond to PMOS current mirrors measurement. Afterwards, one phase is dedicated to temperature measurements using a bipolar transistor. The final eight phases enable communication with the chip. In these phases, using current modulation on power supply, the address of a currently measured cell is sent—on the first four bits the row number is coded, and the last four bits correspond to a column number. When the communicated bit has a value of 1, the supply current increases by 4 mA for the duration of a given measurement phase. When it has a value of 0, the current remains at the default level. Figure 4.3.3 shows the time diagram of the communication phase, and Table 4.1 summarizes the measurements phases.

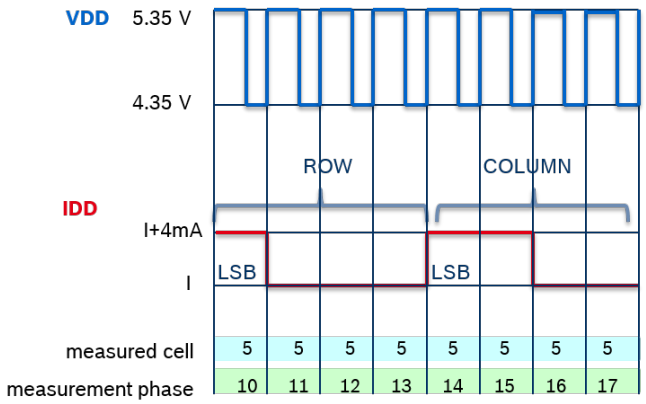

Figure 4.3.3: Communication phase protocol of the IForce sensor.

The information from the consecutive measurement cells and phases is gathered in series. Switching between them is realized through voltage modulation on the power supply terminal. There are three logical power supply levels, as marked in Figure 4.3.4. The measurement of the current for stress calculation is always conducted on the highest power supply level, VDD_{high}. A change between successive measurement phases is executed on the falling edge when the power supply level is changed from VDD_{high} to VDD_{medium} and when a change occurs between successive cells on the falling edge from VDD_{medium} to VDD_{low}. The current cell number and phase number are independent from each other. This means that when a cell number is changed, the phase remains the same. Figure 4.4.1 presents a diagram with the communication protocol.

No.	Measurement phase
1	stress sensitive NMOS forward measurement
2	stress sensitive NMOS reverse measurement
3	stress insensitive NMOS forward measurement
4	stress insensitive NMOS reverse measurement
5	stress sensitive PMOS forward measurement
6	stress sensitive PMOS reverse measurement
7	stress insensitive PMOS forward measurement
8	stress insensitive PMOS reverse measurement
9	temperature measurement using bipolar transistor
10	communication row number (LSB)
11	communication row number (second bit)
12	communication row number (third bit)
13	communication row number (MSB)
14	communication column number (LSB)
15	communication column number (second bit)
16	communication column number (third bit)
17	communication column number (MSB)

Table 4.1: IForce sensor measurement phases.

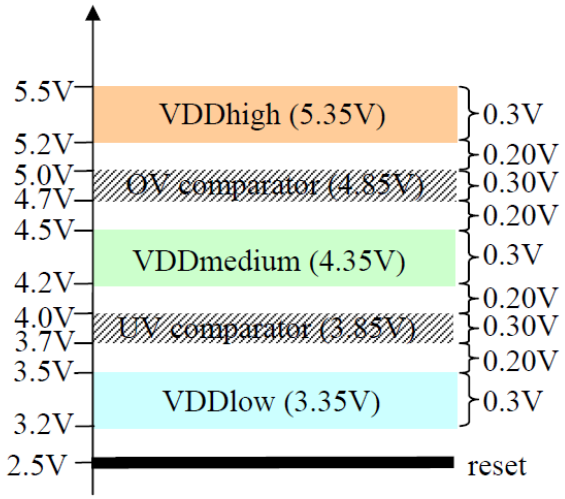

Figure 4.3.4: Logical power supply levels of the IForce sensor.

4.4 Challenges

This section discusses the main challenges posed by the application of the IForce piezoresistive silicon-based stress sensor. First of all, at the initial stage of this work, there was a fundamental lack of an appropriate acquisition system dedicated to the sensor. The communication protocol is custom made, and hence a special dedicated solution for gathering data from multiple sensors had to be created; the developed acquisition unit is described in this section. Furthermore, there are challenges posed by temperature and current dependency of piezoresistive constants; these are also discussed in this section. Finally, the derivation of formulas for stress calculation is performed in order to present all the assumptions that are made in the process. Some of them may induce systematical errors in measurements. The systematical errors are evaluated on different packaging levels.

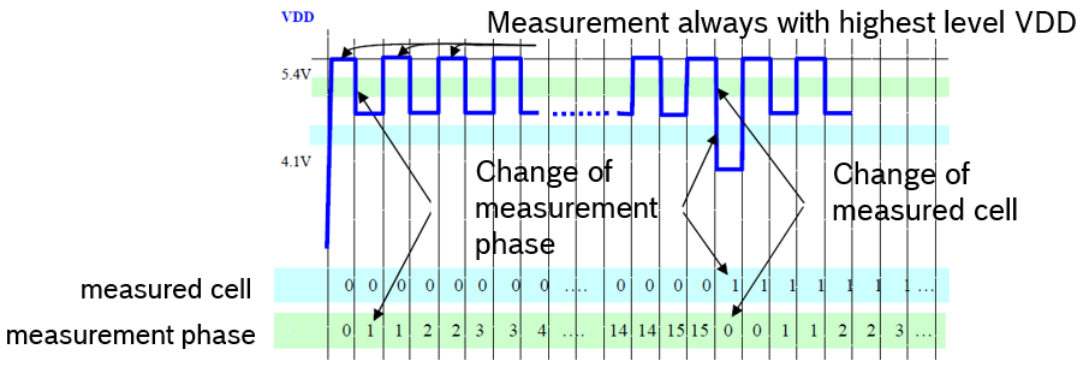

Figure 4.4.1: Steering protocol of the IForce stress sensor.

4.4.1 Acquisition system

Up until this point, the data from IForce sensors were gathered by a dedicated acquisition unit called ChiRP Control Unit, which was developed by TZM company. This unit consists of several functional units (see Figure 4.4.2). Multifunction input/output (I/O) is a block that generates the signal to communicate with a sensor over the power supply signal; it also digitalizes the output of the sensor (i.e., the input and output currents of current mirrors). The current source and waveform amplification unit provides a sufficient and stable amount of current to the chip; it also amplifies the signal from the generator and from the sensor. Programmable control logic (PLC) and PC have controlling functions—PLC is dedicated to only control the current source with the waveform amplifier while PC controls the whole measurement process. In addition, a dedicated software was developed that allows the process of gathering the data to be managed. This makes the procedure user-friendly in that the software enables the whole measurement sequence to be set—such as which measurements should be taken on which cells or in which order—and it also processes and presents the acquired data in a way that is readable and easy to interpret.

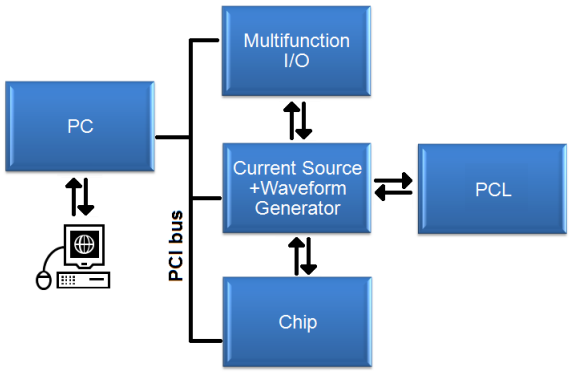

Figure 4.4.2: Functional scheme of an existing acquisition unit [130].

The major disadvantage of this system is the lack of mobility. It is rather large—in size, it is similar to that of a stationary PC. Moreover, it requires some peripherals and a supply from a common power line. In practice, it cannot be used outside the laboratory. It also allows measuring to be performed only for one chip at a time, and for the current study, it is required to handle multiple sensors in parallel. Figure 4.4.3 depicts the existing acquisition unit.

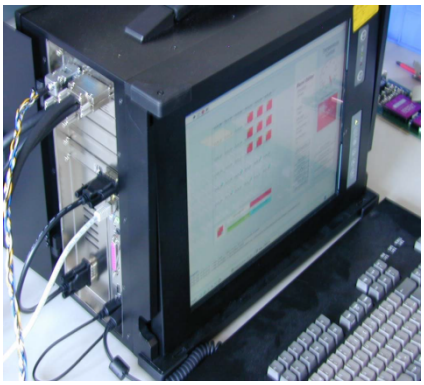

Figure 4.4.3: Photograph of an existing commercial solution.

For this thesis, it was necessary to minimize this system to a point where it is small enough to be mobile in order to conduct in-situ measurements for a large number of sensors. The developed acquisition system is based on the microcontroller discovery board STM32F4, and other modules of the system need to be compatible with it. All inputs of the sensors are controlled by a digital-to-analog converter (DAC). The systems steered from a converter include the voltage generator, which ensures that there is a power supply to the chip and the communication with it, as well as the driving of the current source. Outputs from the chip are digitalized by analog-to-digital converters (ADC). There are three signals that should be read from the sensor, namely the input and output currents of the current mirror and the supply current, over which the data concerning the outgoing measurement are transmitted. Since all of these signals are of a current modulation type, they have to be measured in a differential mode. The whole system is also designed in such a way that the power supply can be taken from the car battery to enable data to be gathered in real working conditions. Figure 4.4.4 presents the functional scheme of the developed solution.

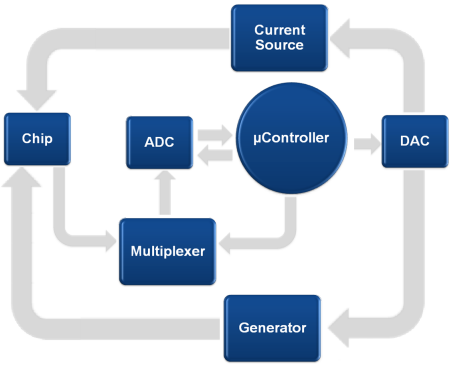

Figure 4.4.4: Functional scheme of the developed acquisition unit.

The functioning acquisition unit was built and tested (see Figure 4.4.5). The dimensions of the developed acquisition unit (WxHxD) are 96x33x65 mm. Both the current source and voltage generator are found to be stable and accurate [131]. The differences of the actual and designed values of the signals are the result of the scattered values of the resistors used; they do not exceed 2.5%. This is not crucial because the only values that are needed to calculate the stress are the currents in both branches of the current mirror. Thus, the most important task is to measure the currents as accurately as possible.

The ADC has a 12-bit resolution. The nominal reference voltage is 2.048 V, and thus the measurement resolution is 0.5 mV. However, for the measurements of the current mirror signals, a PGA gain functionality is used, and this further improves accuracy. This gain is an internal amplifier circuit that can be used if the full scale of conversion is not used. In here, the PGA gain is set to 8. This means that the resolution is increased by 8 times to 0.0625 mV. The current is measured over a 1 kΩ resistor with a tolerance of 0.1% to

ensure good measurement accuracy. This also ensures that the resolution of the current measurement would be at a 0.0625 µA level. The total error of conversion does not rise above ± 2 least significant bit (LSB) [132]. The conversion rate is around 50 samples/sec; this is not critical because the planned measurements do not concern rapidly changing phenomena. This is also the reason why the tests can be executed sequentially. Thus, in order to gather information from multiple sensors, a multiplexer can be used.

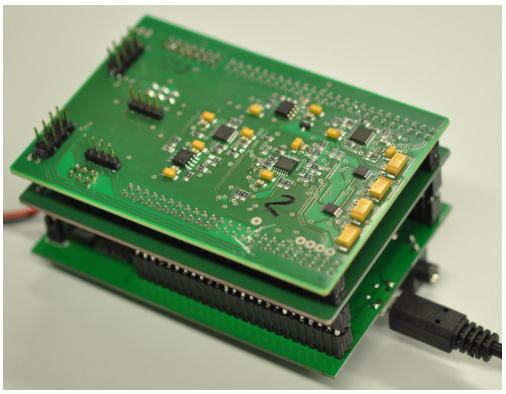

Figure 4.4.5: The created acquisition unit.

The developed device can measure up to 8 sensors at the same time. In the designed solution, two separate multiplexers are used—one for multiplexing the measurement current signals and one for multiplexing the power supply voltage. The multiplexer used for measurement signal is of a differential type. To ensure a good accuracy of measurement, the on-resistance difference between the channels should be minimized. In the chosen device, it should typically not go beyond 0.2 Ω [133]. The main requirement for the multiplexer used for switching the power supply signal is that it should be able to switch high enough currents [134]. The typical supply current should not exceed 10 mA, but in some cases it can be higher and reach up to 100 mA.

The gathered data is saved in an USB flash drive. The data is saved in an unprocessed way, meaning that only the measured values of the currents and voltages are saved. In addition, the time of the measurement is saved for every sensor separately. The data evaluation is done in a Matlab environment. Based on the measured values difference of in-plane stresses, shear stress and temperature can be calculated. The communication with the IForce sensor can also be analyzed.

Every change in the measurement process must be introduced from the program level; such changes can include the change of the type of sensor or the number of sensor measured. This makes this solution less user friendly than the one from TZM. However, for an aware user, the handling of the device should not pose any problems.

The validation of the results obtained from the developed acquisition unit is done using results acquired with the established PC-based system as a reference. First, a distribution of stresses measured at room temperature is compared, as shown in Figure 4.4.6. The accordance of results is very good, in that only minor differences are shown, and they do not exceed a value of 1 MPa. Following this, the stresses measured during a whole temperature cycle -40°C to 150°C is compared. This is the temperature range in which the IForce sensor is rated; the results are shown in Figure 4.4.7. Again, only minor differences are observable. It is worth noting that in the case of measurements within a full temperature cycle, the difference in the obtained results is caused also by the differences in the temperature cycles itself. These differences in turn are caused by factors, such as the specifics of a climate chamber setup, the difference in humidity levels, and the time dependent properties of materials.

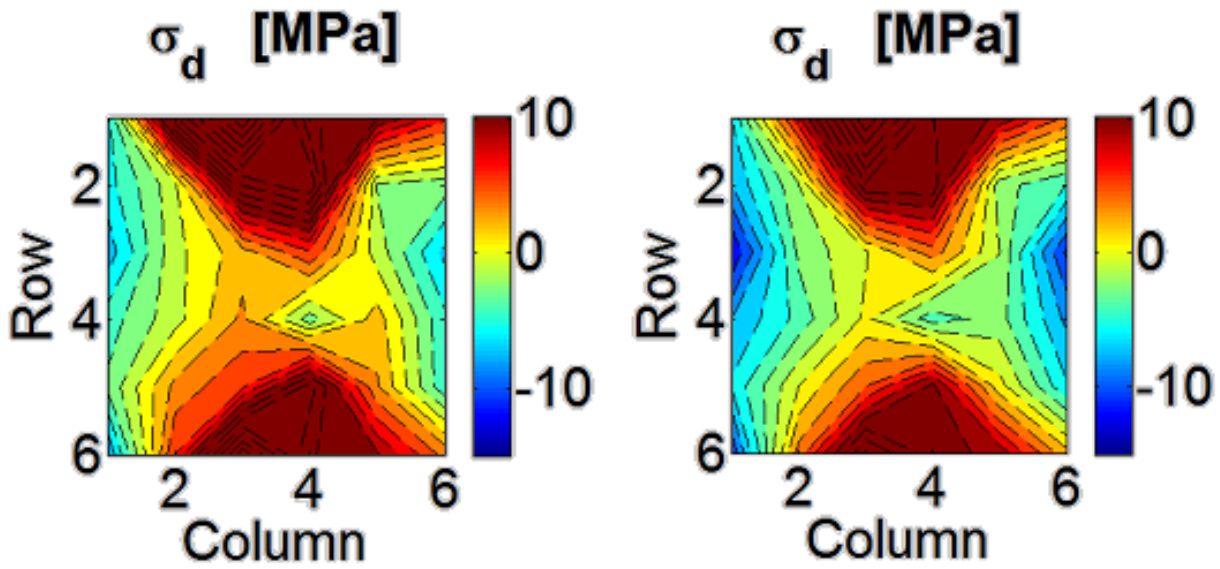

(a) (b)

Figure 4.4.6: Comparison of measurement results at room temperature. (a) Old acquisition system. (b) New acquisition system.

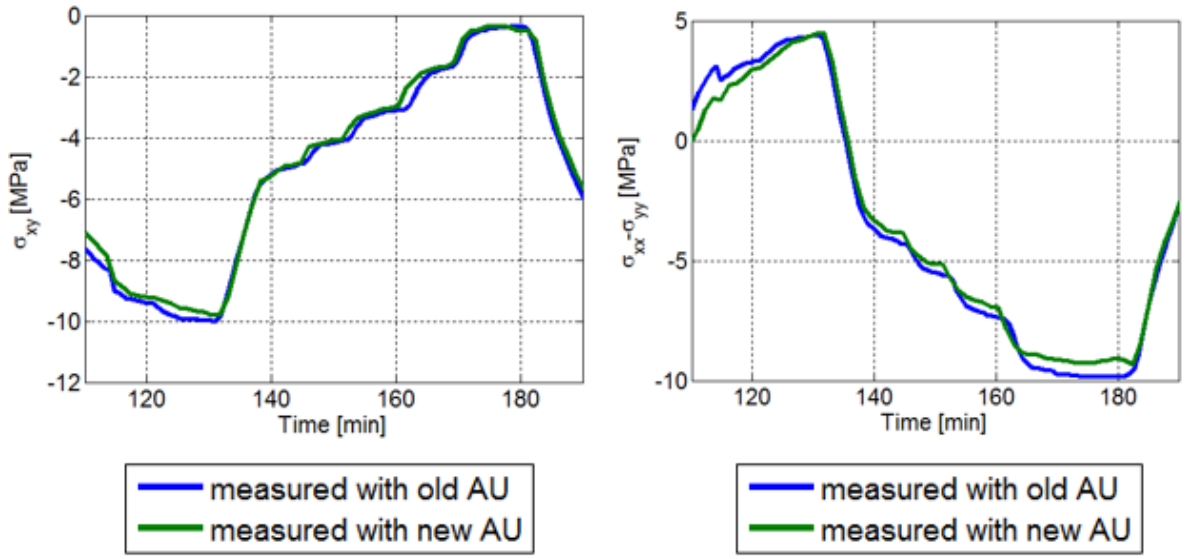

(a) (b)

Figure 4.4.7: Comparison of measurement results during a temperature cycle. (a) Difference stress. (b) Shear stress.

4.4.2 Simplification in stress calculation

In this section, the formulas for stress calculation are derived and discussed. In the derivation of these equations, some assumptions that affect the uncertainties of measurements are made. It is crucial to take note of these assumptions when using a CMOS piezoresistive silicon-based stress sensor.

The starting point to these considerations are the equations that describe the piezoresistive effect in (100) silicon. When a coordination system as in Figure 4.4.8 is chosen (x-axis aligned with [110] crystallographic axis and y-axis aligned with [$\bar{1}$00] crystallographic axis], resistivity in the chosen direction is described by following set of equations [101]:

$$\left.\frac{\Delta\rho_{Si}}{\rho_{Si}}\right|_{0^\circ} = \frac{\pi_S^p}{2}(\sigma_{11}+\sigma_{22}) + \frac{\pi_{44}^p}{2}(\sigma_{11}-\sigma_{22}) + \pi_{12}^p\sigma_{33} + f_p(\Delta T) \tag{4.4.1}$$

$$\left.\frac{\Delta\rho_{Si}}{\rho_{Si}}\right|_{90^\circ} = \frac{\pi_S^p}{2}(\sigma_{11}+\sigma_{22}) - \frac{\pi_{44}^p}{2}(\sigma_{11}-\sigma_{22}) + \pi_{12}^p\sigma_{33} + f_p(\Delta T) \tag{4.4.2}$$

$$\left.\frac{\Delta\rho_{Si}}{\rho_{Si}}\right|_{45^\circ} = \frac{\pi_S^n}{2}(\sigma_{11}+\sigma_{22}) + \pi_D^n\sigma_{12} + \pi_{12}^n\sigma_{33} + f_n(\Delta T) \tag{4.4.3}$$

$$\left.\frac{\Delta\rho_{Si}}{\rho_{Si}}\right|_{-45^\circ} = \frac{\pi_S^n}{2}(\sigma_{11}+\sigma_{22}) - \pi_D^n\sigma_{12} + \pi_{12}^n\sigma_{33} + f_n(\Delta T) \tag{4.4.4}$$

Where:
ρ_{Si} - resistivity of silicon in chosen direction
$f(\Delta T)$ - function describing temperature effects on resistivity change

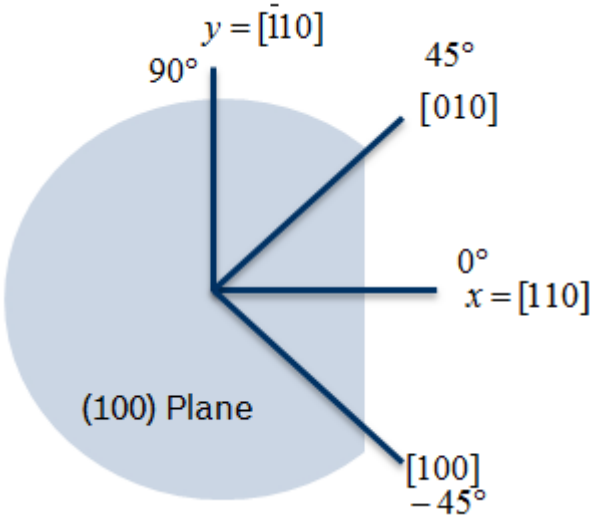

Figure 4.4.8: Chosen coordinate system for (100) Silicon.

However, the physical value measured by this sensor is not resistance but drain current. The widely known equation describing the MOSFET drain current behavior in saturation region is [102]:

$$I_D = \frac{1}{2}\,\mu_e\,C_{ox}\,\frac{W}{L}(U_{GS}-U_{th})^2 \tag{4.4.5}$$

Where:
U_{GS} - voltage between gate and source

U_{th} - threshold voltage of MOSFET
μ_e - mobility of electrical carriers in the channel of MOSFET
C_{ox} - capacitance of the oxide layer
W - width of the MOSFET channel
L - length of the MOSFET channel

In this equation, the dimensional changes due to mechanical stress can be neglected. Deformation of silicon is small, even at relatively high stress values because of its high Young's modulus. The threshold voltage is independent of mechanical stress, as proven in [102]. Thus, the change of drain current induced by mechanical stress mainly depends on mobility changes, and for small fractional changes, the following can be used [102]:

$$\frac{\Delta I_D}{I_D} = \frac{\Delta \mu_e}{\mu_e} \tag{4.4.6}$$

Mobility is also directly related to resistivity of silicon, according to [135]:

$$\rho_{Si} = \frac{1}{q_e \mu_e N_d} \tag{4.4.7}$$

Where:
q_e - electrical charge of majority carrier
N_d - net impurity concentration

Again, for small fractional changes, the following can be written:

$$\frac{\Delta \rho_{Si}}{\rho_{Si}} = -\frac{\Delta \mu_e}{\mu_e} \tag{4.4.8}$$

Thus, in combining (4.4.6) and (4.4.8), the result is as follows:

$$\frac{\Delta I_D}{I_D} = -\frac{\Delta \rho_{Si}}{\rho_{Si}} \tag{4.4.9}$$

(4.4.1)–(4.4.4) can be applied for the recalculation of stresses based on drain current measurement. However, the actual values measured are calculated in this way:

$$I_D = I_{D0} + \Delta I_D = I_{D0}(1 - \frac{\Delta \rho_{Si}}{\rho_{Si}}) \tag{4.4.10}$$

Where:
I_{D0} - reference current (in an absence of mechanical stress)

By substituting (4.4.1)–(4.4.4) into (4.4.10), the following is obtained [102]:

$$I_D|_{0^\circ} = I_{D0}\left[1 - \frac{\Pi_S^p}{2}(\sigma_{11} + \sigma_{22}) - \frac{\Pi_{44}^p}{2}(\sigma_{11} - \sigma_{22}) - \Pi_{12}^p \sigma_{33} + f_p(\Delta T)\right] \tag{4.4.11}$$

$$I_D|_{90^\circ} = I_{D0}\left[1 - \frac{\Pi_S^p}{2}(\sigma_{11} + \sigma_{22}) + \frac{\Pi_{44}^p}{2}(\sigma_{11} - \sigma_{22}) - \Pi_{12}^p \sigma_{33} + f_p(\Delta T)\right] \tag{4.4.12}$$

$$I_D|_{45^\circ} = I_{D0}\left[1 - \frac{\Pi_S^n}{2}(\sigma_{11} + \sigma_{22}) - \Pi_D^n \sigma_{12} - \Pi_{12}^n \sigma_{33} + f_n(\Delta T)\right] \tag{4.4.13}$$

$$I_D|_{45^\circ} = I_{D0}\left[1 - \frac{\Pi_S^n}{2}(\sigma_{11}+\sigma_{22}) + \Pi_D^n\sigma_{12} - \Pi_{12}^n\sigma_{33} + f_n(\Delta T)\right] \tag{4.4.14}$$

Where:
Π_D^n, Π_{44}^p, Π_S^n, Π_S^p, Π_{12}^n, Π_{12}^p - effective piezoresistive coefficients (influenced by the circuit)

To make the equations independent of reference current, the difference in the current from both branches of a circuit is divided by the sum of the currents. The resulting equations take the following form:

$$\frac{I_D|_{45^\circ} - I_D|_{-45^\circ}}{I_D|_{45^\circ} + I_D|_{-45^\circ}} = \frac{-\Pi_D^n\sigma_{12}}{1 - \Pi_S^n\left(\frac{\sigma_{11}+\sigma_{22}}{2}\right) - \Pi_{12}^n\sigma_{33} + f_n(\Delta T)} \tag{4.4.15}$$

$$\frac{I_D|_{0^\circ} - I_D|_{90^\circ}}{I_D|_{0^\circ} + I_D|_{90^\circ}} = \frac{-\Pi_{44}^p(\sigma_{11}-\sigma_{22})}{1 - \Pi_S^p\left(\frac{\sigma_{11}+\sigma_{22}}{2}\right) - \Pi_{12}^p\sigma_{33} + f_n(\Delta T)} \tag{4.4.16}$$

The temperature term is taken into account as the temperature dependent piezoresistive coefficient. As for stress-related terms in the denominator, an assumption is made that these can be omitted, given they should account for only a low percentage of error. Here, the analysis of errors introduced by this assumption is made. The neglected terms are firstly written in this way:

$$D = 1 - \Pi_S(T)\left(\frac{\sigma_{11}+\sigma_{22}}{2}\right) - \Pi_{12}(T)\sigma_{33} \tag{4.4.17}$$

After this, (4.4.16)–(4.4.15) are rewritten to a form that can be used for stress calculation:

$$\sigma_{12} = -D^n\frac{1}{\Pi_D^n(T)}\frac{I_D|_{45^\circ} - I_D|_{-45^\circ}}{I_D|_{45^\circ} + I_D|_{-45^\circ}} \tag{4.4.18}$$

$$\sigma_{11} - \sigma_{22} = -D^p\frac{2}{\Pi_{44}^p(T)}\frac{I_D|_{0^\circ} - I_D|_{90^\circ}}{I_D|_{0^\circ} + I_D|_{90^\circ}} \tag{4.4.19}$$

In (4.3.1) and (4.3.2), the assumption is made where $D = 1$. The influence from additional stress terms in the relevant application can be directly evaluated by taking into account the term D. Table 4.3 shows values of relevant piezoresistive coefficients; these values are theoretical and concern only resistors produced in silicon. However, due to the lack of more accurate information for the sensor used, this study continues to use these values for a further evaluation of errors induced by other stress components.

Piezoresistive coefficient	n-type silicon	p-type silicon
π_{11}	-1.022	0.066
π_{12}	0.534	-0.011
π_{44}	-0.136	1.381
$\pi_S = \pi_{11} + \pi_{12}$	-0.488	0.055
$\pi_D = \pi_{11} - \pi_{12}$	-01.556	0.077

Table 4.2: Piezoresistive coefficients for n-type and p-type silicon with net impurities level smaller than 1018 cm^{-3}

The error introduced by the sum of stress and z-direction stress in the calculation of shear stress is shown in Figure 4.4.9. The errors coming from the sum of stresses and z-direction stress are not linearly combined, and thus they are represented jointly on one plot. The fracture strength of silicon is 300 MPa; for this reason, the calculation were made to 300 MPa for z-stress and to 600 MPa for the sum of the stresses. The error introduced in shear stress calculation can be as high as 40% in the worst case scenario. The error in the

calculation of difference stress is shown in Figure 4.4.10. In this case, the maximal error is much smaller and reaches 2%. This error can be compensated only if the values of out-of-plane stress and the sum of in-plane stresses are known. In the use cases where this error has a considerable effect on the results, these values have to be calculated using FEM simulation. In this way, they can be provided to the acquisition system that can compensates the error of the measurement using (4.4.18)–(4.4.19).

In further parts of this chapter, the real values of the sum of stress and the z-direction stress in the investigated samples are evaluated based on FEM simulation. This procedure is conducted on different packaging levels, namely concerning sensor glued on low temperature cofired ceramics (LTCC), encapsulated in LGA package, and soldered onto the PCB. This enables an evaluation of error propagation with growing packaging level.

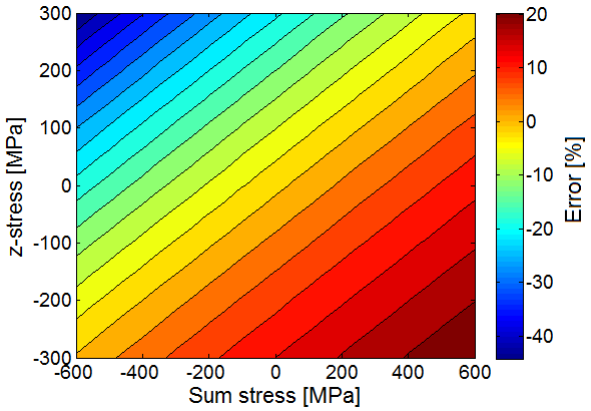

Figure 4.4.9: Error introduced in a shear stress by the sum of normal in-plane stress and z-stress components.

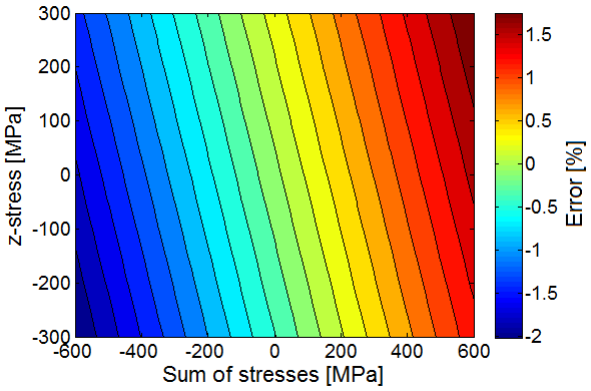

Figure 4.4.10: Error introduced in difference stress calculation by the sum of normal in-plane stress and z-stress components.

4.4.3 Piezoresistive coefficients dependence on temperature

As mentioned, the effect from temperature is taken into account in the form of temperature dependent piezoresistive coefficients. Our sensors were characterized in a temperature range from 22°C to 170°C. The measured characteristics were linear, and the temperature coefficient of piezoresistive constants were calculated (see Table 4.3) [129]. However, these values were measured using silicon bare dies by applying stress to the samples in four point bending test. Thus, the values of the components of stress in the D term are minimal, and the effect on their dependence on temperature cannot be evaluated.

Because of a strong dependence of piezoresistivity on temperature, it is crucial to accurately measure the

	Coefficient $[GPa]^{-1}$	Thermal coefficient $[GPa \cdot K]^{-1}$
π_{11}	-0.78	0.83e-3
π_{12}	1.008	-1.3e-3

Table 4.3: Piezoresistive coefficients for n-type and p-type silicon with net impurities level smaller than 10^{18} cm^{-3}.

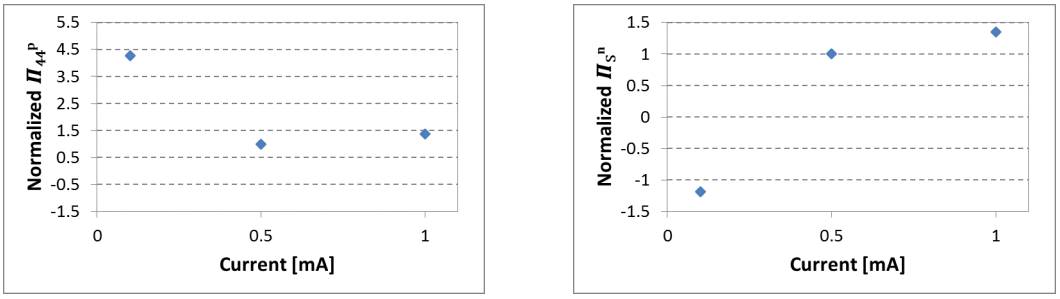

(a) (b)

Figure 4.4.11: Dependence of (a) Π_{44}^{p} and (b) Π_{S}^{n} piezoresistive coefficients on measurement current.

temperature in which the stress measurement is taken. As mentioned, every cell of the IForce sensor contains a bipolar transistor for temperature measurement. However, in practice this way of temperature measurement turned out to be too inaccurate, and thus another method is implemented. This method uses the linear dependency of MOSFET's threshold voltage U_{th} on temperature. As mentioned, the threshold voltage of MOSFET is independent of mechanical stress, which makes it suitable for this application. To calculate U_{th}, a measurement of drain-source voltage U_{DS} at three drain level currents must be made. Then, the threshold voltage is determined, and the temperature can be calculated according to the formula:

$$T = \frac{(U_{th} - U_{th0})}{\alpha_{U_{th}}} + T_0; \tag{4.4.20}$$

Where:
U_{th} - threshold voltage at the measured temperature
U_{Th0} - threshold voltage at the reference temperature
$\alpha_{U_{Th}}$ - temperature coefficient of threshold voltage
T_0 - reference temperature

The temperature coefficient $\alpha_{U_{Th}}$ must be calculated empirically using a calibration procedure. It is worth mentioning that this measurement method is a relative one; therefore, a reference measurement at a known temperature is needed at the beginning of every experiment. However, this approach to temperature measurement has a good accuracy and was used throughout this work.

4.4.4 Piezoresistive coefficients dependence on measurement current

In the recent studies [108], the dependence of piezoresistive coefficients on the measurement current was reported. This observation was verified with measurements taken in this thesis. Figure 4.4.11 shows the piezoresistive coefficient dependence on the current of a sensor used in this paper. The sensor was characterized using a 500 µA measurement current, and the presented values were normalized using known piezoresistive coefficients at this level of current. This property does not affect the accuracy of measurement but users should be aware of it.

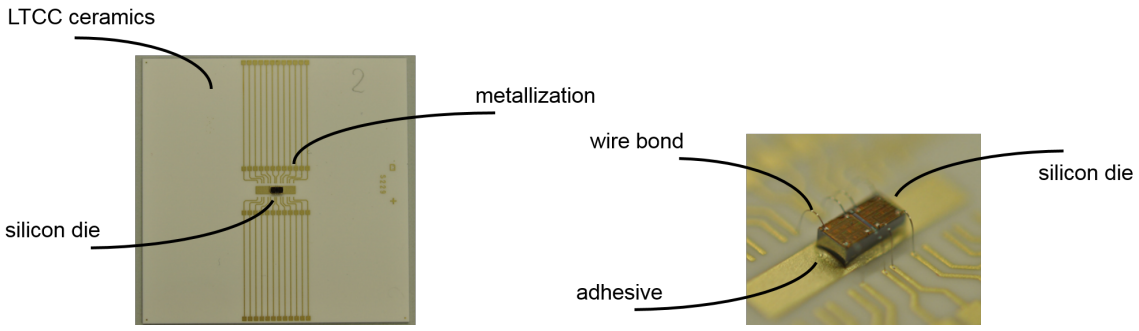

(a) (b)

Figure 4.5.1: The LTCC sample used in this experiment. (a) Whole substrate. (b) Close up on the silicon die.

4.5 Uncertainties evaluation

The accuracy considerations of measurements with the stress sensor can be found in the literature. In [136], Jaeger et al. discussed calibration errors and rosette alignment errors for a resistive type of stress sensors. In [137], Hussain et al. discussed measurement errors of the rosette type sensor on (111) silicon. More extensive analytical and experimental analyses on the measurement uncertainties are required so that the applicability of the sensor in the PHM domain can be extended.

4.5.1 Experimental validation

This section presents the experimental results of measurements conducted at different packaging levels with the stress sensor; FEM simulation results are given here as well. The goal of these considerations is to evaluate the effect of the sum of stresses and out of plane stress on the measurement results as the complexity of the system grows.

The thesis takes the simplest case of the silicon sensor glued onto LTCC as the starting point (see Figure 4.5.1). This sample consists of a ceramic substrate with a NiPdAu metallization layer. The sensor die is attached to it with an adhesive, and electrical connections are constituted with gold wire bonds. The behavior of this sample is relatively straightforward as it is possible to assume both silicon and LTCC materials are linear elastic. The only viscoelastic material in this system is the adhesive that mounts the chip to the LTCC. However, this material was characterized on site using DMA and TMA techniques. Thus, its properties have been determined and can be further used to predict the thermo-mechanical behavior of the sample.

Then, the sensor in a 3x3 mm Land Grid Array (LGA) package is investigated (see Figure 4.5.2). A double sensor chip (two times 12 measurement cells) is glued onto a PCB substrate. The electrical connections from the chip to the substrate are constituted by wire bonds. The terminals that form the electrical connection to the outside of the package are established by a metallization layer on the bottom side of the PCB substrate. The whole construction is encapsulated by an EMC. The schematic of the package is shown in Figure 4.5.2(b) and the x-ray is in Figure 4.5.2(c).

The next set of samples consists of a sensor in an LGA package soldered onto a PCB (see Figure 4.5.3(a)). Finally, the overmolded test vehicle was examined. The cross-section showing overmolded stress sensor is presented in (b) of Figure 4.5.3. Both these samples are based on the test vehicles introduced in Chapter 3. In this case, an evaluation of stresses on system level was conducted.

To separate the systematical and random errors in the measurements, eight samples of each kind are measured, and an average value is taken for further analysis. Then, the measurement results were compared

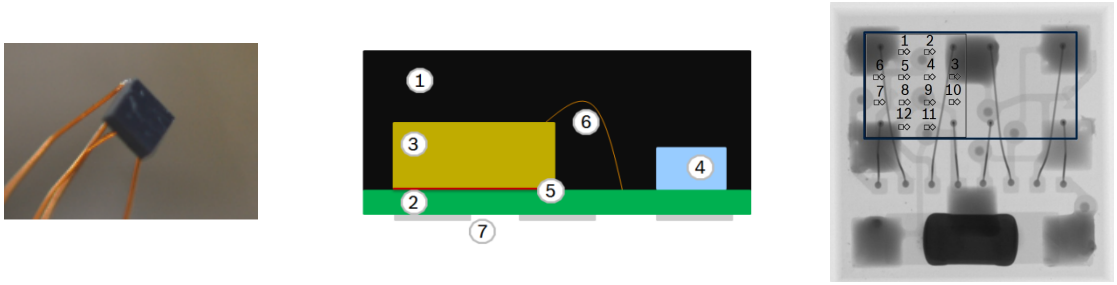

(a) (b) (c)

Figure 4.5.2: LGA package. (a) Image of an LGA package. (b) LGA package construction [(1) mold, (2) PCB, (3) stress sensor, (4) ceramic, (5) die attach, (6) wire bond, (7) soldering pads]. (c) X-ray of the package with the points of measurement marked.

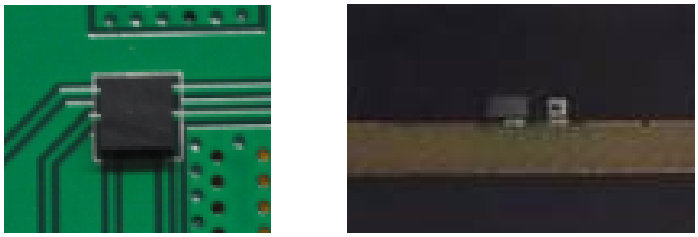

(a) (b)

Figure 4.5.3: The samples used in this experiment. (a) Sensor in LGA package soldered onto a PCB. (b) Cross- section of an overmolded sample.

with the simulation.

Measurements were made at -40°C and 125°C for every sample. The presented values are relative in order to enable a comparison with the simulation; the reference measurement was taken at room temperature. Figures 4.5.4-4.5.7 present the averaged results of the measurements from eight samples on LTCC, on component level, on a PCB, and in an overmolded case, respectively. It is worth noting that the measured stress has a symmetrical distribution only in the cases of LTCC and the overmolded sensor. The LTCC sample is symmetrical on the x-axis, while the LGA package is not (see Figure 4.5.2). Thus, the distribution of stress in the LGA package presented in Figures 4.5.5-4.5.6 cannot be symmetrical. In the case of the overmolded sample, the constraint introduced by outer EMC plays a dominant role on the behavior of the package, and the asymmetry introduced by the LGA package design is negligible. However, in all four cases, the structure is close to symmetrical on the y-axis, as well as results from both sides of the sensor. This allows us to present the measurement results only from one half of the sensor without losing much information.

The values in Figures 4.5.4 to 4.5.7 are presented along with the corresponding results from simulations and from error bars related to sample variability. Figure 4.5.4 shows the results concerning LTCC. Here, the agreement between the simulation and measurement is very good for both difference stress and shear stress, especially when the error bars are taken into account. It is mainly due to the fact that the thermo-mechanical behavior of this sample is straightforward and can be accurately predicted.

In Figure 4.5.5, the same results for the standalone component are presented. The agreement between measurements and the simulation in this case is reasonable, but taking the calculated uncertainties into account does not fully explain the differences. The distribution of stresses within the silicon die is predicted correctly by numerical modeling. The differences between the measured and predicted values do not exceed 5 MPa and may be a result of various factors, such as slight geometrical differences or the humidity present in the molding compound.

Next, the results with PCB samples are shown in Figure 4.5.6. Here, the agreement between the simulation

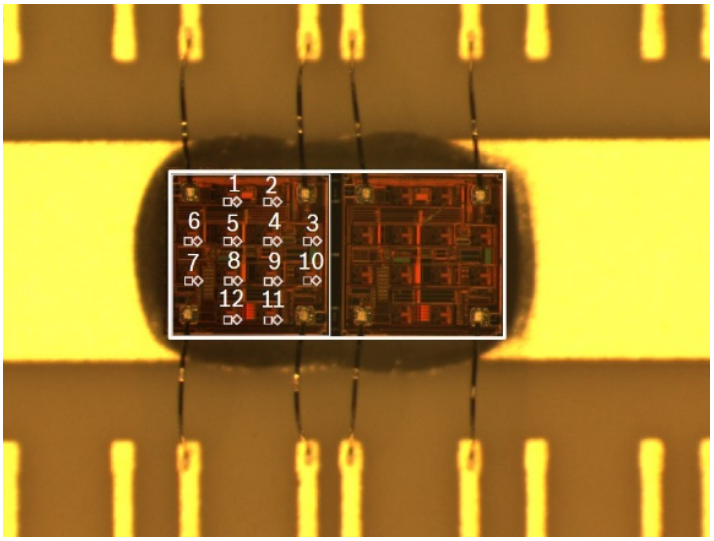

(a)

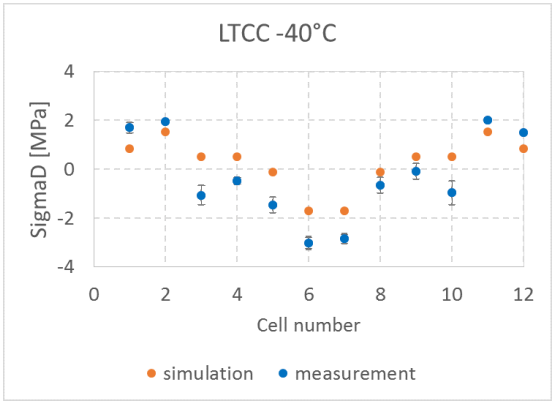

(b)

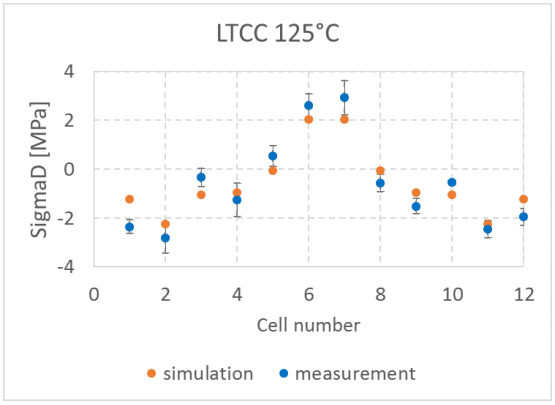

(c)

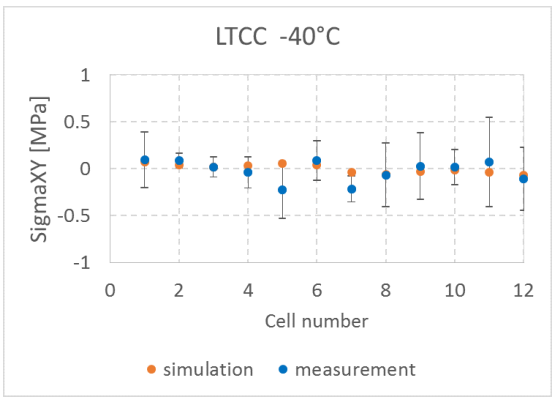

(d)

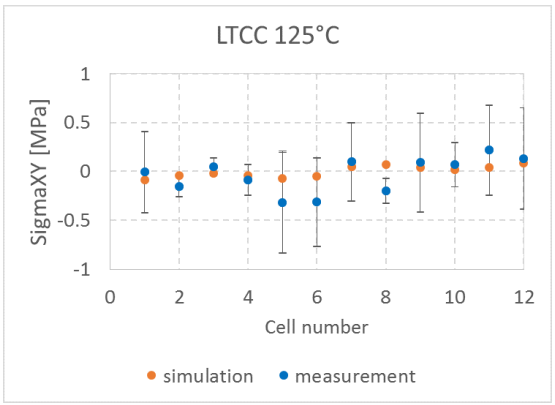

(e)

Figure 4.5.4: Simulation vs measurement results for LTCC samples. (a) Sensor with marked measurement points. (b) Difference stress at -40°C. (c) Difference stress at 125°C. (d) Shear stress at -40°C. (e) Shear stress at 125°C.

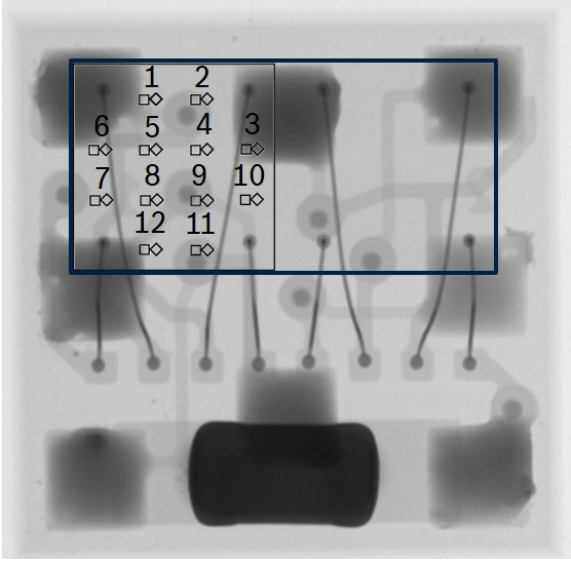

(a)

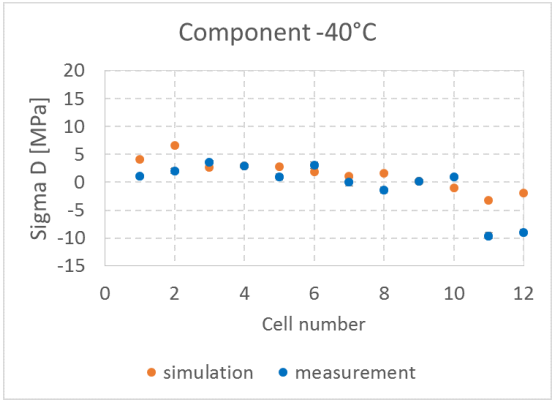

(b)

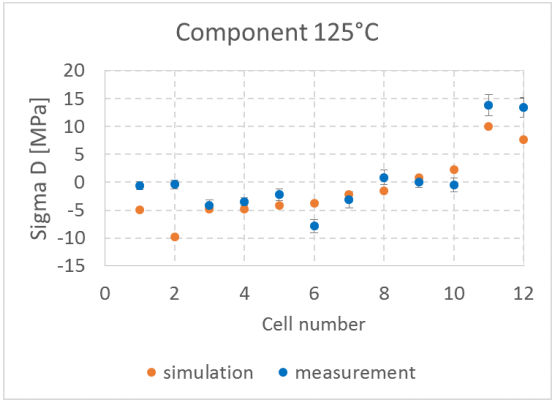

(c)

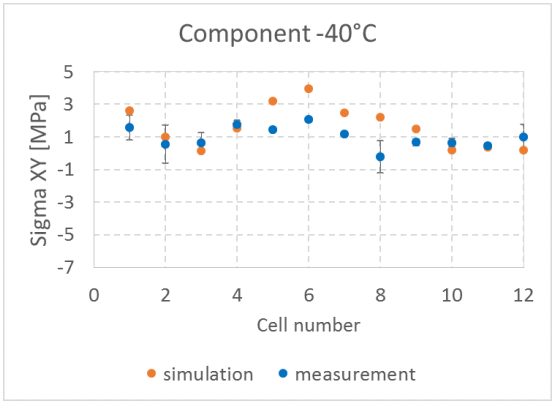

(d)

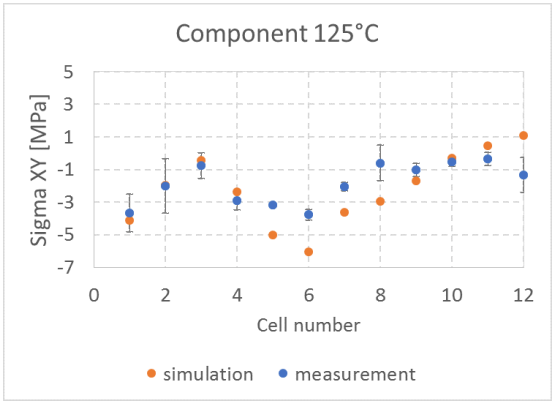

(e)

Figure 4.5.5: Simulation vs measurement results for component level samples. (a) Sensor with marked measurement points. (b) Difference stress at -40°C. (c) Difference stress at 125°C. (d) Shear stress at -40°C. (e) Shear stress at 125°C.

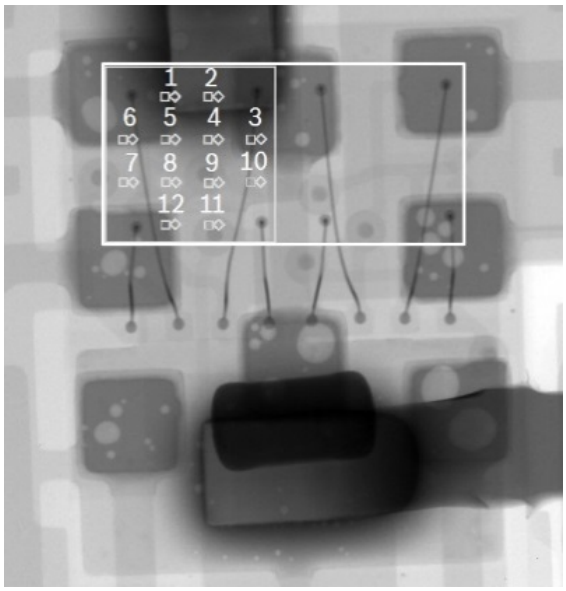

(a)

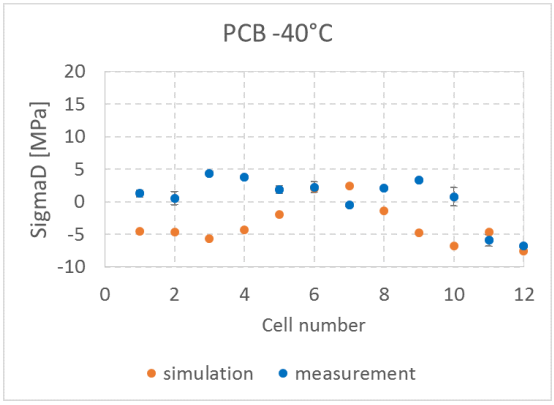

(b)

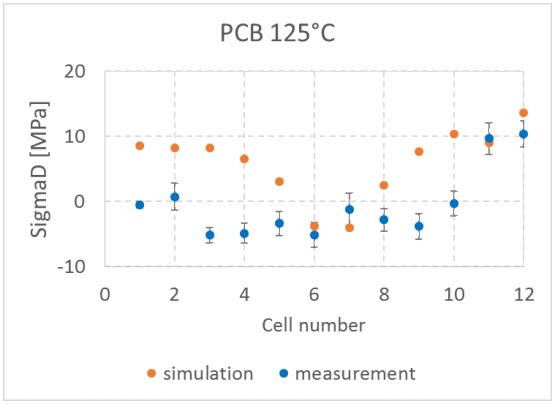

(c)

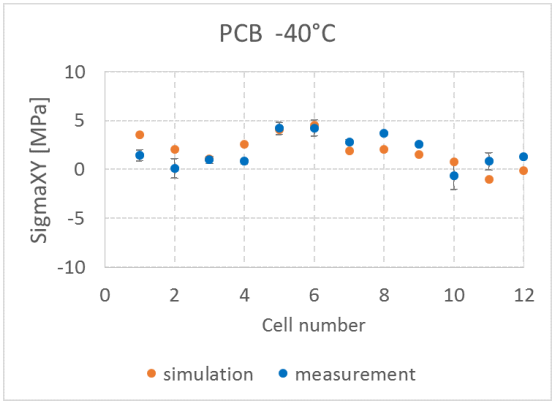

(d)

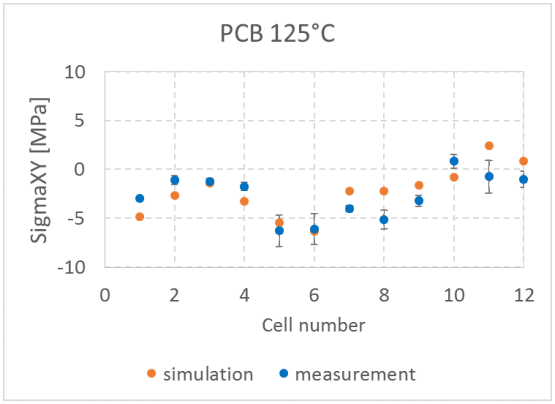

(e)

Figure 4.5.6: Simulation vs measurement results for PCB samples. (a) Sensor with marked measurement points. (b) Difference stress at -40°C. (c) Difference stress at 125°C. (d) Shear stress at -40°C. (e) Shear stress at 125°C.

(a)

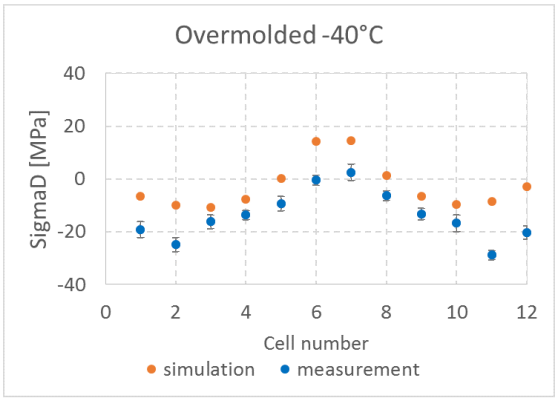

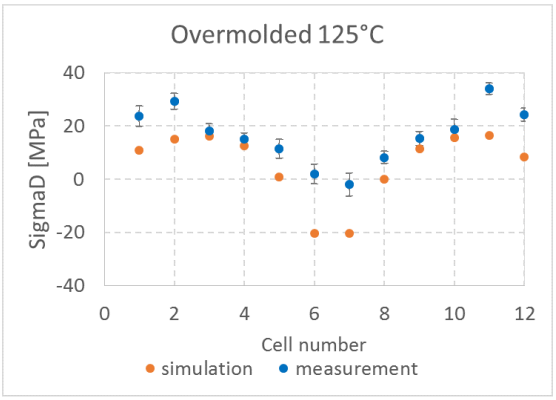

(b)

(c)

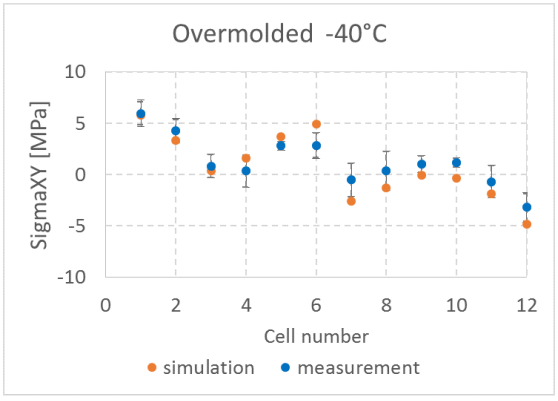

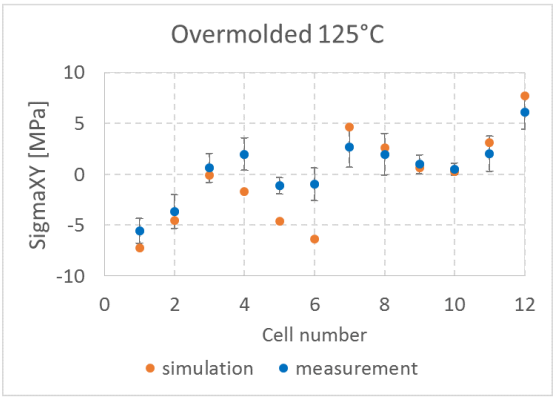

(d)

(e)

Figure 4.5.7: Simulation vs measurement results for overmolded samples. (a) Sensor cross-section. (b) Difference stress at -40°C. (c) Difference stress at 125°C. (d) Shear stress at -40°C. (e) Shear stress at 125°C.

and the experiment is satisfactory only for shear stress measurements. In the case of difference stress, the results are in the same range of values, but the distributions are inconsistent. This is caused by various factors, such as the assumption regarding linear material properties of solder. On a system level, the modelling of solder with non-linear material properties would be computationally too expensive. Another possible reason for this discrepancy is that the initial deformation of a package is not taken into account in a simulation, and the stress free temperature is assumed at 25°C. However, the predicted range of values is acceptable, and the simulation can be used for further analysis.

Finally, Figure 4.5.7 shows the results concerning overmolded samples. In here, the distribution of stress on the silicon die is matching. However, there are some slight discrepancies when it comes to the values of stresses. This may be caused by the non-linear temperature dependent material properties of the outer molding compound. The behavior of this material is very complex and very hard to capture in such a complicated model. However, the differences between the measured and simulated values are reasonably small; in most cases they do not exceed 10 MPa. Thus, the simulation results are considered satisfactory and are used for further analysis.

4.5.2 Sample variation

The values of standard deviation as a measure of sample variation are evaluated for all investigated cases and are summarized in Table 4.4. As expected, the sample variation increases with the packaging level as the number of varying design parameters also grows; these parameters can entail different materials or different layers thickness. The more complex the sample, the more processes it needs to go through and the more variability exists between the samples. The values of sample variations for a corresponding measurement cells are plotted in Figures 4.5.9-4.5.12 at all four packaging levels. The variation is smaller with shear stresses because the corresponding stress values are smaller. However, there are no significant differences between the measurements executed at different temperatures.

Table 4.4: Standard deviation as a measure of sample variation at different packaging levels.

	σ_{12} standard deviation [MPa]	σ_d standard deviation [MPa]
LTCC	0.23	0.6
LGA package	0.5	0.8
PCB	0.8	1.45
Overmolded	1.3	2.7

4.5.3 Random error

Additionally, the repeatability of the measurements was assessed. The goal is to determine what part of statistical error is caused by the measurement process itself. For this purpose, 60 consecutive measurements were conducted at a controlled temperature of 25°C. This uncertainty is independent of the packaging level, and thus the measurements are conducted only for PCB samples. The results in a form of histogram for both difference stress and shear stress measurements are shown in Figure 4.5.8. They confirm that a normal distribution of the investigated variable can be assumed. The average repeatability over all measurement cells calculated at 68% (1σ) confidence level was 0.18 MPa for shear stress and 0.27 MPa for difference stress. It should be emphasized that the main factor affecting the repeatability in here is the accuracy of the current measurement. Although both currents are measured with the same precision, the repeatability is different. It is caused by the different constants in (4.3.1) and (4.3.2) that introduce other uncertainty propagation into the final results. It can be easily seen that the uncertainty propagation of current measurement depends linearly on the piezoresistive constant used for stress calculation. The ratio of the relevant constants is around 2:3, which is similar to the ratio of the calculated repeatability values.

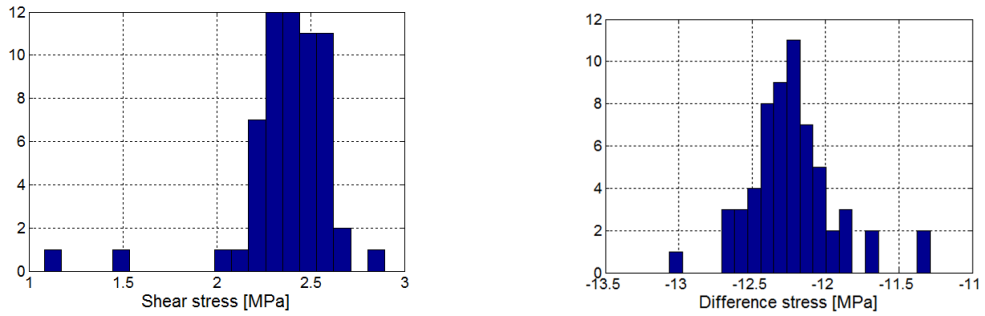

(a) (b)

Figure 4.5.8: The histogram of measurements conducted in the same conditions (a) for shear stress and (b) for difference stress.

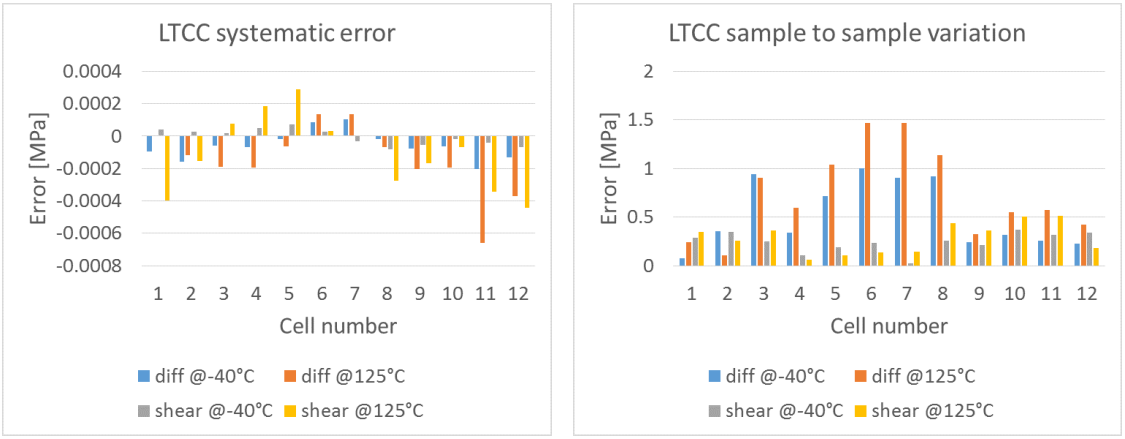

(a) (b)

Figure 4.5.9: Errors evaluation of LTCC samples. (a) Systematic error. (b) Sample variation.

4.5.4 Systematic error

The validated simulations were used to extract the values of the sum of stresses and z-component of stress for evaluation of systematic errors. The results of this study are presented in this section.

The systematic error was calculated in percentage according to (4.4.17), taking into consideration the signs of corresponding stress values. The values in MPa are calculated based on the measurement results. The values of both systematic errors and sample variations for a corresponding measurement cells were plotted in Figures 4.5.9-4.5.12 for all investigated cases. There are no observable trends in the uncertainties distribution, neither for different cells, nor stress values or temperatures.

To compare the systematic error values quantitatively, the maximal values of the sum of stresses and calculated errors in percentage and in MPa are summarized in Table 4.5. It is worth noting that the systematic error, similarly to the statistical uncertainty, increases with the packaging level. For LTCC, the absolute value of this error does not exceed 0.0007 MPa, while for the component it is already around 0.017 MPa. At the PCB level, it reaches 0.03 MPa, and in the case of the overmolded sample, it amounts to 0.1 MPa. This shows that the relevant stress levels increases with the packaging level, but the maximal error even on the system level remains negligible. A much greater influence on the uncertainties of these measurements are introduced by sample variation and random errors. Even for the overmolded samples, this error is around two orders smaller than the random error.

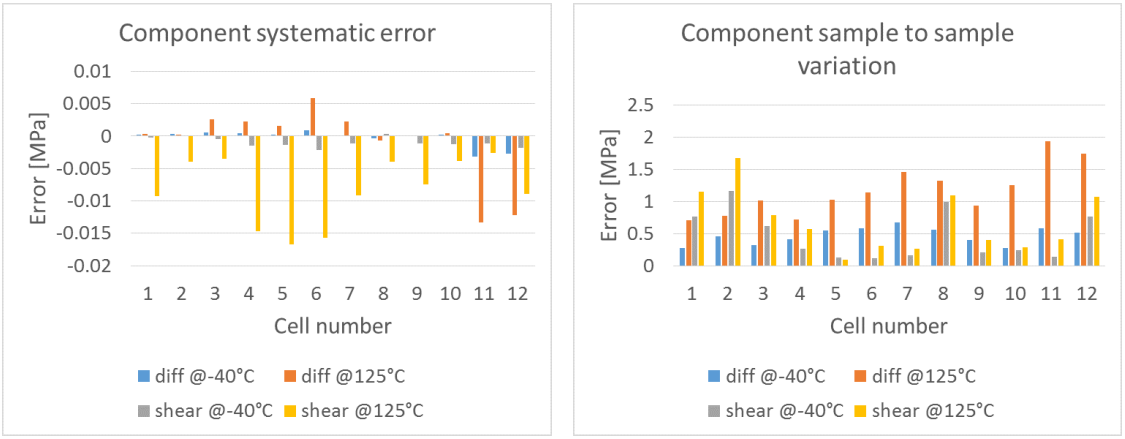

(a) (b)

Figure 4.5.10: Errors evaluation of component level samples. (a) Systematic error. (b) Sample variation.

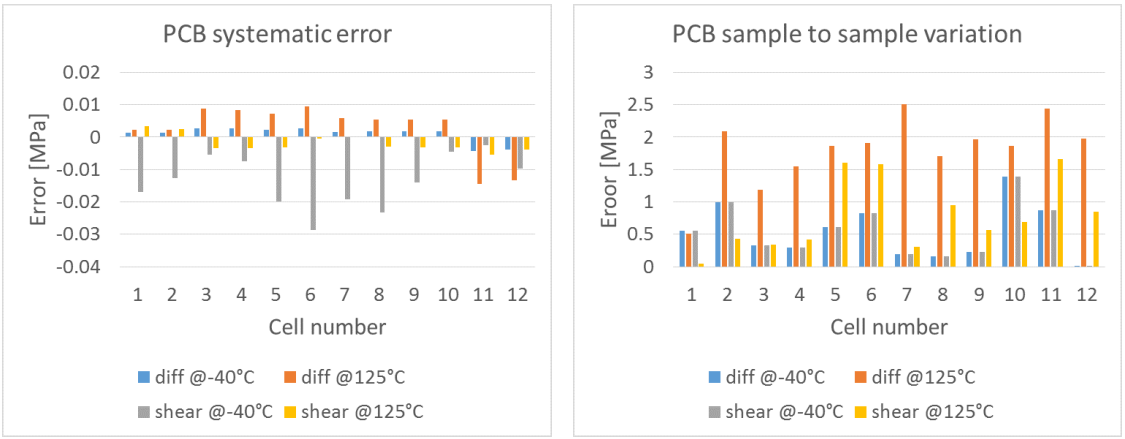

(a) (b)

Figure 4.5.11: Errors evaluation of PCB level samples. (a) Systematic error. (b) Sample variation.

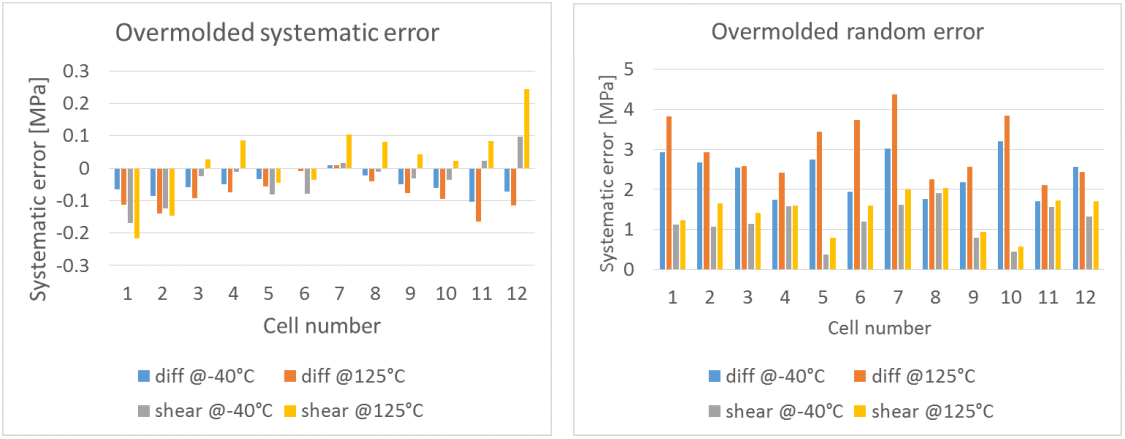

(a) (b)

Figure 4.5.12: Errors evaluation of overmolded samples level. (a) Systematic error. (b) Sample variation.

Table 4.5: The maximal values of calculated systematical errors at different packaging levels.

	LTCC	Component	PCB	Overmolded
z component of stress [MPa]	7.96	5.71	10.27	6.58
Sum of stresses [MPa]	6.6	35.97	53.52	186.88
Max. error σ_{12} [%]	0.54	0.73	1.4	4.37
Max. error σ_{12} [MPa]	0.0004	0.017	0.029	0.023
Max. error σ_d [%]	0.022	0.10	0.15	0.51
Max. error σ_d [MPa]	0.0007	0.013	0.014	0.096

4.6 Summary

This chapter introduced the piezoresistive silicon-based stress sensor, which has a major potential for applications in PHM. The sensor directly measures stresses in the structure, and thus can be directly related to damage. This chapter also discussed the construction, the working principle, and communication protocol of the used sensor. Then, the challenges that come from the measurements with this sensor were identified. These include the dependence of piezoresistive coefficients on temperature and on measurement current, a lack of a dedicated measurement system, and the systematical errors introduced in stress calculation caused by the simplification of the formulas. Then, the developed solution for data gathering from a large number of sensors was presented. Additionally, the statistical and random uncertainties related to the measurements with the CMOS-based piezoresistive stress sensor were evaluated. In the case of statistical error, the error caused by the measurement process itself was separated from the error caused by other factors, such as the variability between samples. It was shown that the systematic errors introduced by the simplifications in the stress calculation are negligibly small, even at a system level. However, the value of this error is strongly application dependent, and in the worst case scenario it can be as large as 10-15%. Users should be aware of this, and they should make sure that in their specific application this error can be in fact ignored.

Chapter 5

Virtual modeling

5.1 Introduction

In this thesis, a detailed FEM modelling of the investigated ECU is performed. The model was prepared in a very meticulous way (see Figure 5.1.1). Geometry was validated with cross-sections and x-ray imaging. For a detailed stress sensor modelling, a PCB substrate homogenization technique was implemented [138]. The viscoelastic material properties were implemented for all epoxy-based thermosets and PCB prepreg. Exact loading conditions of an active operation were modelled by executing a series of coupled simulations, namely electrical, thermal, and thermo-mechanical [139]. To create a physics-of-failure model, a submodeling technique was used. This method enables an evaluation of the exact load on the design elements where the failure is expected. Various validation techniques were used. Thermography and thermocouples measurements were used to validate thermal model prediction. The thermo-mechanical simulation was validated locally by the stress sensor and globally by warpage measurements. Additionally, for a detailed assessment of behavior of all the materials, moiré interferometry was used.

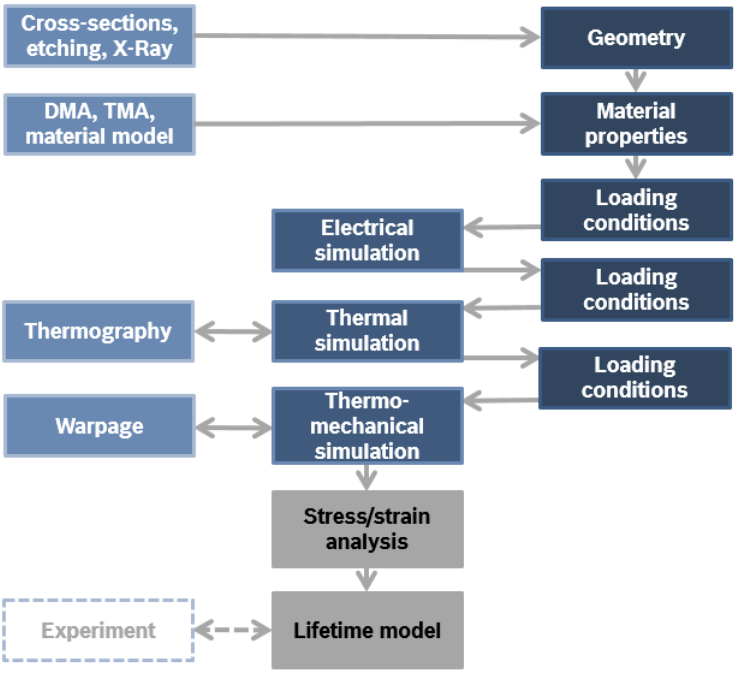

Figure 5.1.1: PoF modeling workflow.

For all numerical simulations presented in this work, a commercial FEM code ANSYS® was used. The

important steps of model preparation are described in this section.

5.2 Geometry

First of all, a detailed geometry of all design elements must be considered. This includes the copper layer layouts on the PCB with thermal vias, as well as the internal geometry of the components.

The identified failure mechanisms are strictly related to the design elements of the package. These components are commercially available, and thus our knowledge on its internal structure was limited. To collect the necessary information on the inner construction of the DPAK component, an x-ray imaging of the IC package was performed. The mold was then etched from the DPAKs, as shown in Figure 5.2.1. Based on this, it was possible to create a detailed geometry of the wire bond. Finally, the DPAK was cross-sectioned to collect the information on the thickness of the copper lead frame, the die attach, and the thickness of the silicon die.

(a) (b) (c)

Figure 5.2.1: DPAK package. (a) Modelled geometry. (b) Etched. (c) Cross-sectioned.

Moreover, the internal geometry of the stress sensor must be very accurate. This includes also the layout of the PCB within the sensor package. Simulating the exact geometry is computationally too expensive, as the PCB layout contains very small features. Thus, the PCB substrate inside the sensor package was modelled using homogenization technique [138]. The procedure of an applied homogenization approach is presented in Figure 5.2.2. First of all, a number of copper and prepreg layers of a considered PCB substrate must be defined. In this case, there are two copper layers containing layout—one layer is at the top and the other is on the bottom of a substrate. The substrate model is divided into respective layers of known thickness. The prepreg layer in the middle is modelled as continuous material with orthotropic properties. For the layers containing layout, a mesh from the FEM model must be known in order to implement the homogenization technique. Then, the local properties can be calculated for each cell of the FEM model separately using linear rules of mixture. The effective Young's modulus is calculated as follows [140]:

$$E_{eff} = V_{Cu}\, E_{Cu} + V_{Ppg}\, E_{Ppg} \tag{5.2.1}$$

Where:
V_{Cu},V_{Ppg} - the volume fraction of copper and prepreg ($V_{Cu} + V_{Ppg} = 1$),
E_{Cu},E_{Ppg} - the Young's modulus of copper and prepreg.

Similarly, other effective properties are computed as an average of properties of the individual phases according to their volume fractions. The orthotropic nature of Young's modulus of prepreg are taken into account by calculating the effective values in every direction separately. An example of a calculated effective Young's modulus distribution is shown in Figure 5.2.3. The effective value of CTE is calculated while taking into account the elasticity modulus, according to the relation here [141]:

$$\alpha_{eff} = \frac{\alpha_{Cu}\, V_{Cu}\, E_{Cu} + \alpha_{Ppg}\, V_{Ppg}\, E_{Ppg}}{V_{Cu}\, E_{Cu} + V_{Ppg}\, E_{Ppg}} \tag{5.2.2}$$

Where:

α_{Cu},α_{Ppg} - the coefficient of thermal expansion of copper and prepreg.

The results from the simulation that takes the layout into account validate the measurements much better as shown in Figure 5.2.4. The range of stress values is predicted properly in both cases. However, the distribution of stresses on the silicon die changes significantly when the detailed geometry is considered. In the case of simplified geometry, there is a peak in stress values at the edge of the chip in cells 6 and 7; this peak is not observed in measurements. The detailed simulation predicts the stress distribution much more accurately.

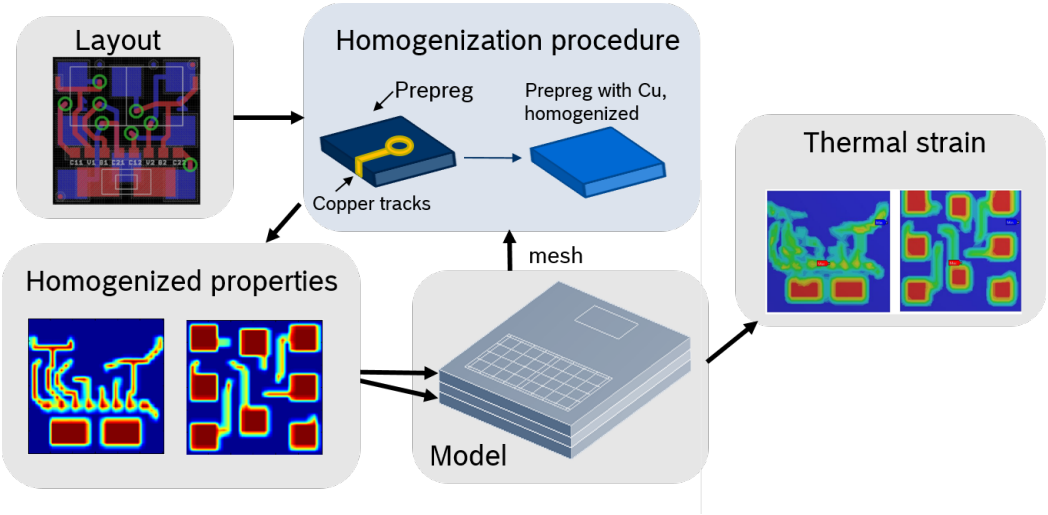

Figure 5.2.2: Homogenization technique workflow.

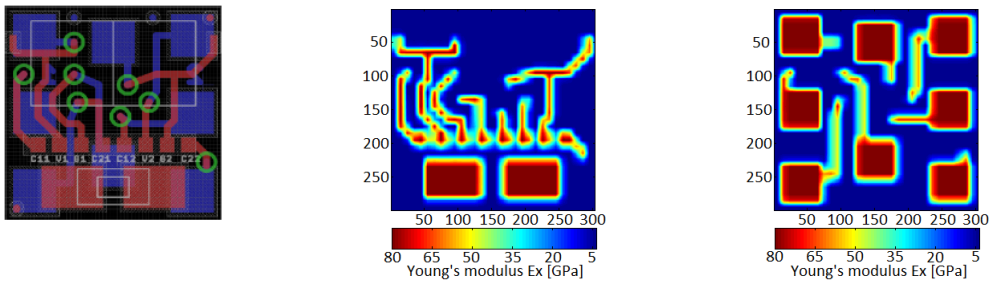

(a) (b) (c)

Figure 5.2.3: Calculated effective Young's modulus distribution. (a) Sensor PCB layout. (b) Calculated homogenized Young's modulus values in the x-direction for the top layer and (c) for the bottom layer.

Another very important aspect of stress sensor modelling is appropriate meshing. Throughout the chip thickness, the mesh should be finer near the chip surface, as shown in Figure 5.2.5(a). This is because the actual device measures the stresses only in the top layer. The area at the top of the chip was divided according to the chip cells arrangement as depicted in Figure 5.2.5(b). The actual position of measurement cells marked on an X-ray picture of the sensor is presented in Figure 5.2.5(c). The applied mesh is hexahedral, with four by four element matrix in every measurement cell. Due to such a geometry preparation, it is possible to extract the values from the exact same locations as in the experiment.

Finally, the geometry of the test vehicle PCB should also be prepared very carefully. In this approach, the PCB layout must be modelled explicitly in order to perform electrical simulation. The layout also affects

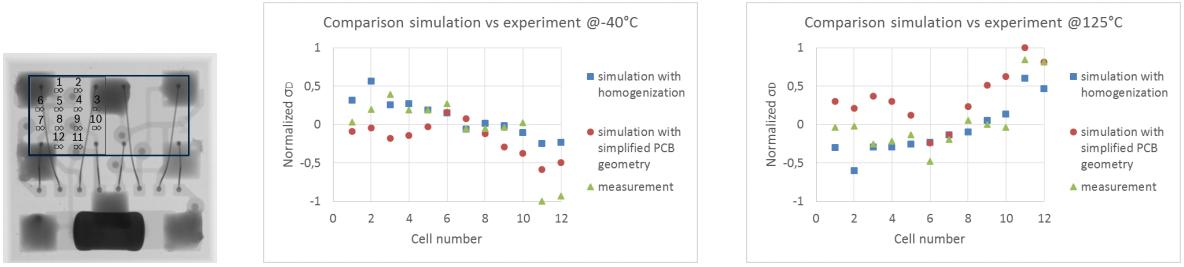

(a) (b) (c)

Figure 5.2.4: Stress measurement vs. simulation with/without layout. (a) Cells position. (b) At -40°C. (c) At 125°C.

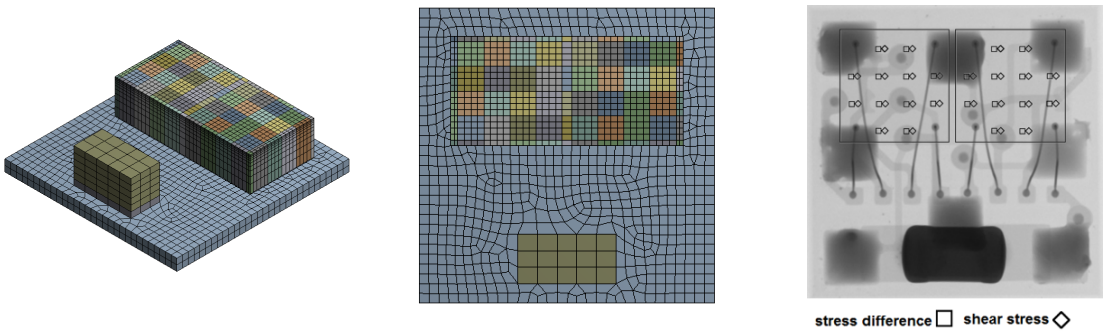

(a) (b) (c)

Figure 5.2.5: The geometry of the stress sensor. (a) Mesh through the thickness of the chip. (b) Mesh view from the top of the chip. (c) Placement of the measurement cells in an actual sensor package.

the results of thermal modelling. The structure of the PCB (number of layers and its thickness) determines the thermal and thermo-mechanical behavior of the test vehicle. These details of the PCB geometry were validated by cross-sectioning the existing test vehicle.

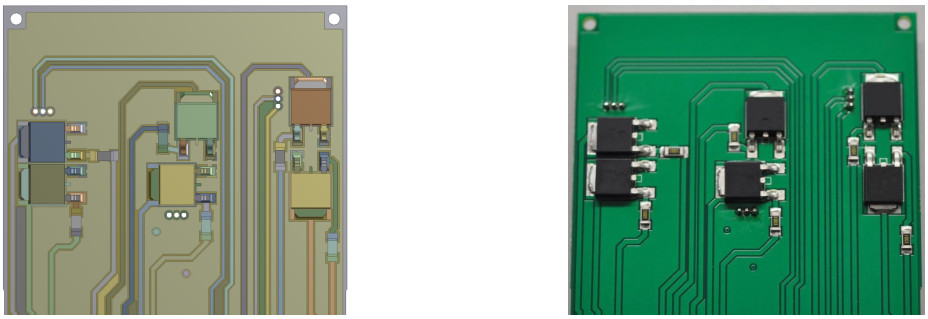

(a) (b)

Figure 5.2.6: Comparison between (a) a modelled geometry (b) a real geometry.

Furthermore, the appropriate meshing is essential to avoid mesh influence on the results, especially when values of stress are evaluated. As mentioned, the stress sensor mesh was prepared very carefully and meticulously. Also, the critical layers in wire bond and solder—where the damage parameters are evaluated—were meshed with high quality hexahedral elements. As a general rule, a dominant hexahedral mesh was applied to all bodies. Moreover, in all bodies with large surface to thickness ratio, at least two elements across the thickness were used in order to avoid having too stiff behavior. On the other hand, in such a large system level model, the element count should be considered. Having too large of a number of elements causes a very long solution time. Thus, in the bodies where no stress values were evaluated, a coarser mesh was applied.

The final model of the overmolded test vehicle consist of roughly 3.5 million nodes.

5.3 Materials

Another important aspect of accurate FEM modelling is material properties characterization. The linear elastic properties of LTCC were measured in one of the previous projects and available for use. The detailed DMA characterization of the adhesives and molding compounds were performed on site; the molding compounds are of an epoxy-based thermoset type. These measurements were performed specifically for the investigated product. Typically, three to four samples are tested in tensile and in three point bending mode. Only one representative measurement made in tensile mode is then taken for the creation of the material model. The other measurements are made to ensure that the values are consistent, and they are compared to each other based on the variability range supplied by the material supplier. This value is specific for every type of material. The results of our measurements are usually also compared to the characterization results provided by the supplier. Additionally, composite materials used for PCBs were characterized by measuring the prepreg and copper foils separately. Afterwards, the linear viscoelastic material models were created using an optimization procedure to calculate prony terms that can be implemented in the FEM software. The thermo-mechanical material properties used in a discussed model are presented in Table 5.1. The electrical and thermal properties that are summarized in Table 5.2 are taken from a public database.

Table 5.1: Thermo-mechanical material properties

Material properties		Modulus of elasticity [MPa]	CTE [ppm/K]	Material law
LTCC	Ceramics	128000	6	Linear-elastic
	Adhesive	3940	40	Viscoelastic
PCB	Copper traces	80000	17	Linear-elastic
	Prepreg	24000	14	Viscoelastic
Stress sensor	Substrate	23000	19	Homogenized
	Adhesive	8000	51	Viscoelastic
	Silicon die	167000	8	Linear-elastic
	EMC	26000	8	Viscoelastic
DPAK	Copper lead frame	125000	17	Linear-elastic
	Solder	49551	20	Viscoplastic
	Silicon die	167000	8	Linear-elastic
	EMC	17000	12	Viscoelastic
	Wire bond	64000	25	Viscoelastic

Table 5.2: Thermal and electrical material properties

Material properties		Resistivity [Ω·m]	Heat conductivity [W/ m ·K]
PCB	Copper traces	2e-8	350
	Prepreg	-	0.7
Stress sensor	Substrate	-	0.7
	Adhesive	-	1
	Silicon die	-	120
	EMC	-	0.75
DPAK	Copper lead frame	2e-8	300
	Solder	2e-7	50
	Silicon die	-	120
	EMC	-	1.5
	Wire bond	3e-14	230

5.4 Loading conditions

For a system level simulation such as entire ECUs, both the boundary and loading conditions play a very important role. The predictability of the numerical simulations strongly depends on residual stresses due to assembly steps as well as coupled loading conditions.

In this study, the electrical, thermal, and thermo-mechanical simulations are conducted sequentially in order to predict the expected lifetime of design elements, such as a solder joint or wire bond. Details of this simulation chain are described in the following sections.

5.4.1 Electrical model

It is especially crucial for a physics-of-failure model assessment to take into account the exact load in the investigated design element. In the testing conditions, in each DPAK package a power of 1.2 W is dissipated, but the current passing through the system causes a significant heat dissipation also in other parts of the circuit. In particular, the heat dissipation in the wire bond is relevant not only because it is a design element considered when creating a physics-of-failure model but also because the current density in this area may be large. Additionally, it was observed during experiments that the current in the paths on the PCB affected the temperature distribution.

To consider these effects, this thesis developed an electrical model. In this simulation, a current flow was set through the wire bonds, copper frame, solder, and copper layers. The current flow through the silicon die is not considered. For the silicon die to be taken into consideration in an electrical model, a silicon die layout would have to be known. Moreover, it can be assumed that the heat dissipation is homogenous because of the high thermal conductivity of silicon. Thus, the known heat dissipation in silicon is considered first in the thermal model.

Figure 5.4.1. presents the calculated Joule heat distribution. The increased heating caused by the current flow can be observed in the copper traces on a PCB and in the wire bond that connects the emitter terminal.

5.4.2 Thermal model

A thermal simulation was conducted to calculate the temperature distribution under an active loading profile. For the first loading condition, the Joule heating distribution result from the electrical simulation was used.

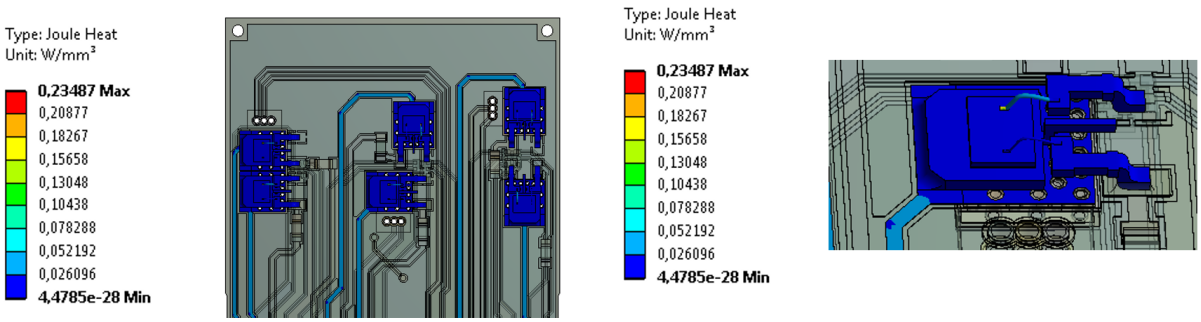

(a) (b)

Figure 5.4.1: Joule heating on the PCB from the electrical simulation. (a) PCB overview. (b) Inside of DPAK package.

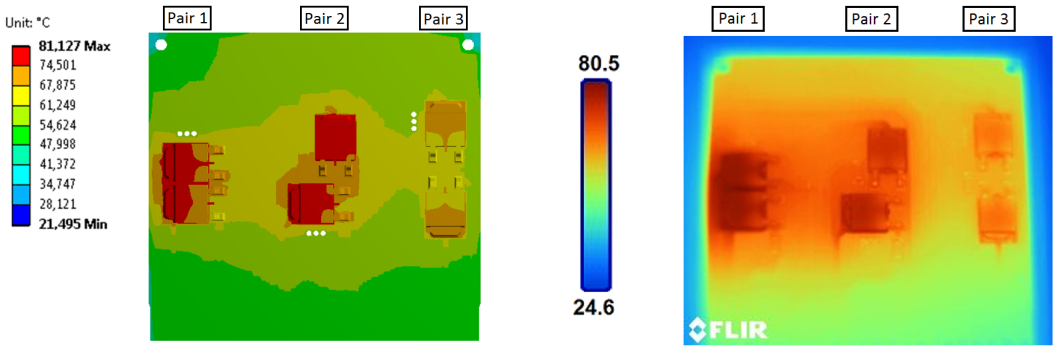

(a) (b)

Figure 5.4.2: Comparison of (a) the result of thermal simulation and (b) thermography of the test vehicle under active loading conditions.

Additionally, a known heat dissipation in the silicon die was introduced. The test vehicle was placed on a thermally insulating surface under natural convection conditions.

The result of the thermal simulation is shown in (a) of Figure 5.4.2. The maximum temperature reached 81°C. Pair 1 has much higher temperatures as the DPAKs are located close to each other. As expected, the lowest temperature was observed in Pair 3 as the effective distance between the DPAKs was larger and thus cross-heating was smaller.

This result was validated with thermography measurements. The test vehicle was painted with a matte black paint for an ideal and uniform reflectance of the sample. Measurements were made continuously until the steady state was reached, which occurs at around the 30 minute mark of power dissipation. The result is shown in (b) of Figure 5.4.2. The temperature distribution agrees well with the numerical prediction. More specifically, the predicted maximum temperature is nearly identical to the measured value, and the predicted temperature distribution at the top of the DPAK shows a very similar distribution compared with the measurement data (e.g., the lower temperature in the area of the two copper lead fingers for all six DPAKs). The effect of the PCBs self-heating is visible in both simulation and experimental results. A slightly higher temperature in the copper paths is evident, which is attributed to detailed geometry representation (i.e., fine details of the PCB traces are found in the model) and realistic loading conditions (i.e., the model uses the results of the electrical simulation for the thermal analysis). The validated thermal simulation results are carried to the next step as an input for the thermo-mechanical simulation.

5.4.3 Global thermo-mechanical model

The simulation was conducted in two steps in order to predict the expected lifetime of relative small design elements, such as solder joint and wire bond. First, an approximated global response of the system was obtained from a linear analysis to make the analysis numerically feasible. The free expansion boundary conditions were defined which correspond to the field use case and all the preformed experiments. Next, the submodeling technique was employed in order to investigate the local loads that can cause solder joint failure or wire bond lift-off. For the submodeling, critical layers were created specifically in the solder joint and the wire bond.

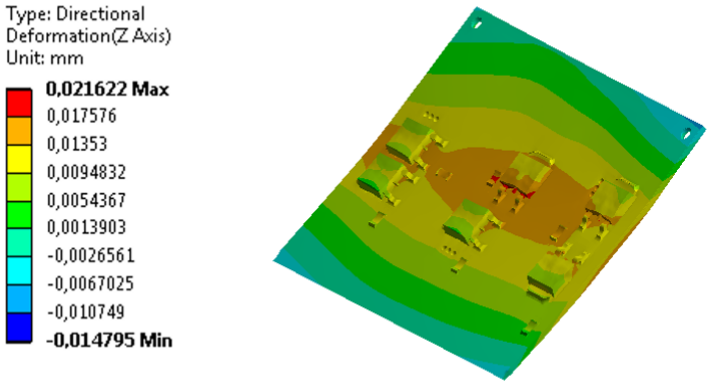

Figure 5.4.3: Global PCB deformation.

The accumulated creep or plastic strain energy dissipated in the critical layers was used as a damage index. Two separate simulations were conducted—a passive temperature cycle in the range of temperatures from -40°C to 125°C and an active temperature cycle. The active thermal condition uses the temperature distribution obtained from the thermal simulation. The out-of-plane deformation obtained from structural simulation with active thermal load is presented in Figure 5.4.3. The test vehicle bends visibly along the longer edge, which is found to have the largest deformation in the middle of the PCB, just where the DPAK packages are placed.

Both passive and active simulations were globally validated using warpage measurement. The deformation of the test vehicle was measured using digital image correlation (DIC). Figure 5.4.4 depicts the results of the DIC, which represent the absolute deformation of the test vehicle. The relative out-of-plane displacements evaluated along a diagonal line (white line) are compared with the numerical prediction in (a) and (b) of Figure 5.4.5. Both results correlate very well with the experimental data.

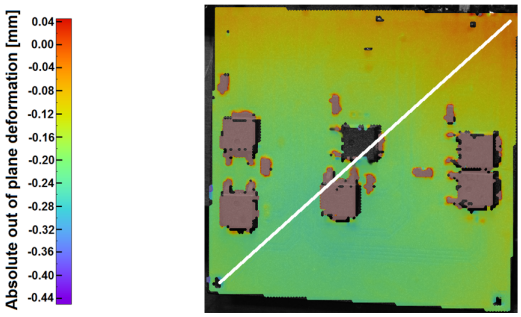

Figure 5.4.4: Measured absolute out of plane deformation. The path along which the results are evaluated is marked in white.

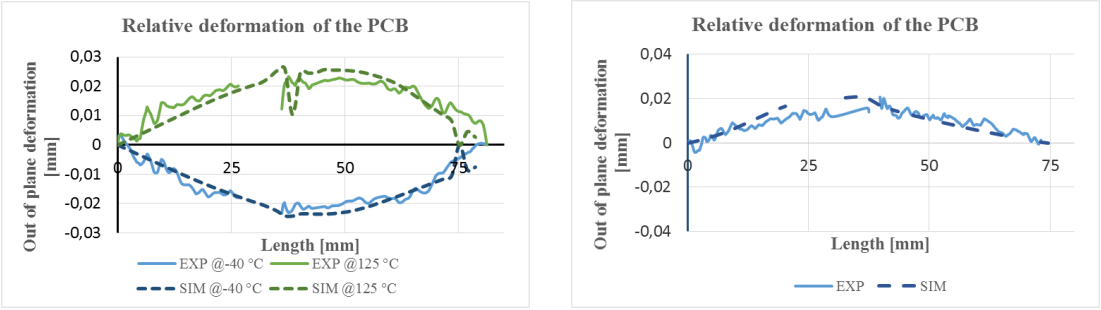

(a) (b)

Figure 5.4.5: Warpage measurement and simulation comparison. (a) Passive cycling at -40°C and 125°C. (b) Active cycling at room temperature.

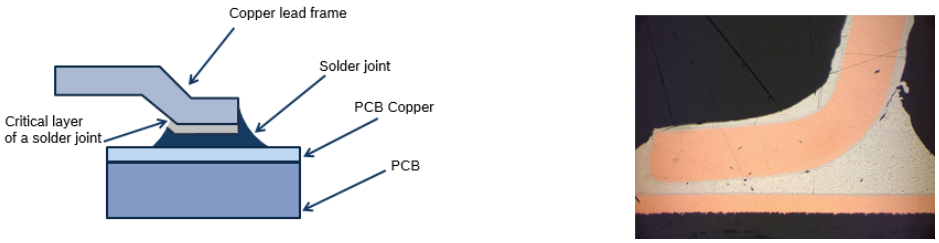

(a) (b)

Figure 5.4.6: Critical layer location in solder joint (a) with its schematic and (b) damaged component.

5.4.4 Thermo-mechanical submodel

The results obtained from the submodeling were used for risk assessment. Both of the damage indexes were calculated in a critical layer that was created specifically at the interface between the copper lead frame pin and the solder joint. The critical layers were created in order to achieve the required mesh quality at the location where the damage parameters are evaluated. Mesh quality is one of the most critical parameters in achieving the desired accuracy. Hexahedral elements that were 10 µm thick with an aspect ratio less than 1:5 were used in this study in both critical layers. The thickness of this layer was 10 µm and it was located in the area where failure was expected.

Creep strain energy density (CSED) or creep strain (CS) is the most common damage index to evaluate the lifetime of a solder joint [142]. The CSED damage indicator was used in this work, and it was calculated until the values converged to the steady state value. Typically, the steady state dissipation of CSED is reached in three to five and five to ten cycles for passive and active temperature cycles respectively. Figure 5.4.6 shows the location of the critical layer for solder joint; the effect of intermetallics was ignored.

For the wire bond, plastic strain energy density (PSED) was used as damage index. The values were calculated in a critical layer at the interface between the wire bond and the copper lead frame, at a point where the failure was expected (Figure 5.4.7).

Figure 5.4.8(a) depicts a representative creep strain energy density distribution in the critical layer of the solder joint. The maximum CSED is accumulated on the top of the solder joint at the interface with a copper lead finger, at the point where the lead finger bends. It is also the point where the crack initiation was observed during temperature cycle experiments. To reduce the mesh sensitivity, the volume averaged method (VAM) was used (1). With this method, the damage indexes of each element are normalized by the volume of the element as:

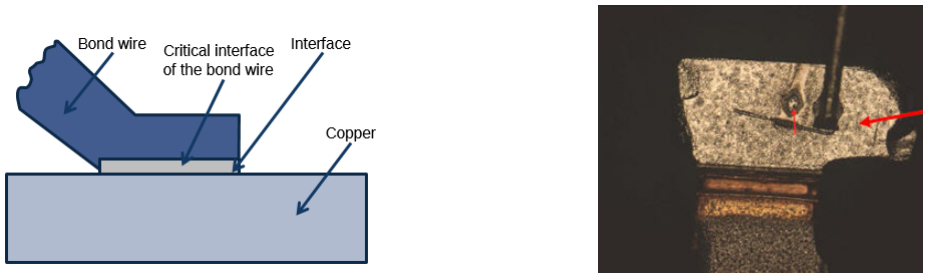

(a) (b)

Figure 5.4.7: Critical layer for the wire bond (a) with its schematic (b) and damaged component.

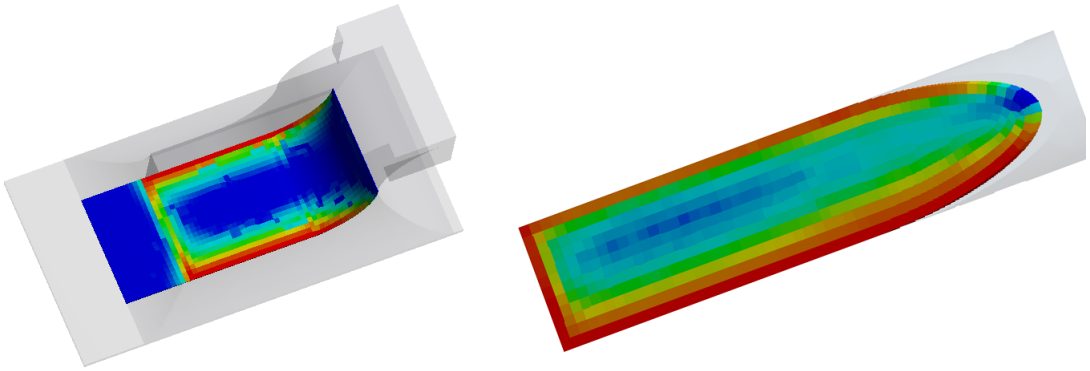

(a) (b)

Figure 5.4.8: The results evaluated within the critical layer. (a) CSED distribution in the critical layer of the solder joint. (b) PSED distribution in the critical layer of the wire bond.

$$\Delta W_{AVG} = \frac{\sum \Delta W_{SED} * V_{el}}{\sum V_{el}} \tag{5.4.1}$$

Where:
W_{AVG} - the average creep (plastic) strain energy density accumulated per cycle in a critical layer,
W_{SED} - the creep (plastic) strain energy density accumulated per cycle in each element,
V_{el} - the volume of each element.

The same methodology was implemented to calculate the damage indexes of the wire bond. Figure 5.4.8(b) depicts the PSED accumulated during the last passive temperature cycle. The critical load occurred at the edge of the bond. The obtained results are further used in order to create a physics-of-failure model, as presented in Chapter 6.

5.5 Verification

5.5.1 Moiré interferometry method description

To carefully verify predictions of the thermo-mechanical modeling, a moiré interferometry experiment was conducted. The main goal of this study is to verify the non-linear behavior of the materials present in the system, mainly the molding compounds and PCB prepreg.

Moiré interferometry is an optical measurement technique that enables a recording of in-plane deformations parallel to the surface of the sample. Based on that, it is possible to calculate strains induced in a solid body.

A major advantage of this technique is the fact that it enables displacement measurement with very good sensitivity on the whole surface of the sample. Moreover, it is very accurate due to large signal-to-noise ratio. Furthermore, as it responds only to the geometrical changes, it is equally effective to measure all kinds of deformations (e.g., elastic, viscoelastic, or plastic) and materials (e.g., isotropic, orthotropic, or anisotropic) that have been subjected to various loadings (e.g., mechanical, thermal, or dynamic) [143]. This technique has been extensively used in the microelectronics industry to investigate stresses induced by thermal cycling [[144]–[146] and hydroscopic swelling [147]–[149] in electronic packages.

An example of a moiré pattern that gives us the information on the specimen deformation is shown in Figure 5.5.1. The mechanism of formation of this pattern is simple spatial interference of two regular patterns; the idea is presented in Figure 5.5.2. In the moiré measurement system, one of the patterns is created by a grating replicated on an investigated sample surface. The grating is replicated on a specimen before the deformation takes place, and the deformation state of the sample in the time of the grating replication is taken as a reference. The typical specimen grating frequency is 1200 lines/mm in both x- and y- directions. The reference pattern is created by a virtual grating, by either diffraction or interference of two coherent beams as shown in Figure 5.5.3. Usually, virtual reference gratings have spatial frequency of 2400 lines/mm. When a sample is not deformed, these two beams create a uniform fringe pattern. After applying the load, the grating on a sample is then deformed, and the directions of diffracted rays are changed. This creates the irregular interference pattern that can be analyzed further to obtain information on deformation distribution. During the experiment, two orthogonal fields U and V are recorded, which represent the x- and y- components of displacement at every point.

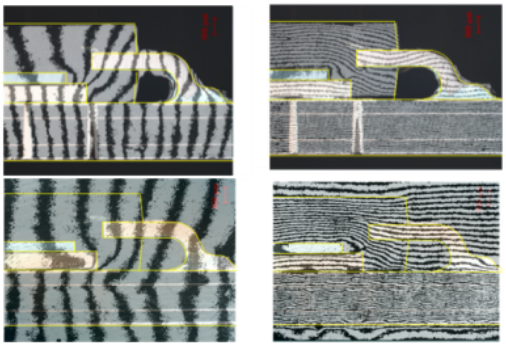

Figure 5.5.1: U and V field displacement for an electronic package [7].

The schematic diagram that illustrates the functioning principle of the moiré interferometer is shown in Figure 5.5.4. In general, the measurement setup consists of several components, namely 1) a grating replicated on a specimen, 2) optical elements that are used to create the virtual reference gratings, and 3) a camera to register the fringe pattern. The grating replicated on a specimen has the pattern in both x and y-directions. The beams B_1 and B_2 are marked in green, and they create a virtual reference grating for an N_x fringe pattern that corresponds to the x-component of displacement. Similarly, the beams B_3 and B_4, marked in blue, are needed for the evaluation of the y-component of displacement. They must be coherent and collimated. Typically, a digital CCD camera is used to register the fringe patterns, and it must focus on the surface of the specimen. The spatial resolution of this method depends on the frequency of gratings, and for given values (the grating on a specimen 1200 lines/mm, the reference grating 2400 lines/mm) the displacement of 0.417 µm corresponds to one fringe order.

The fringes counting starts with the choice of a zero order fringe that establishes a reference. Along this fringe, the displacement is assumed to be zero. The fringes are then counted, and a relative displacement in the rest of the sample is calculated based on the following relations:

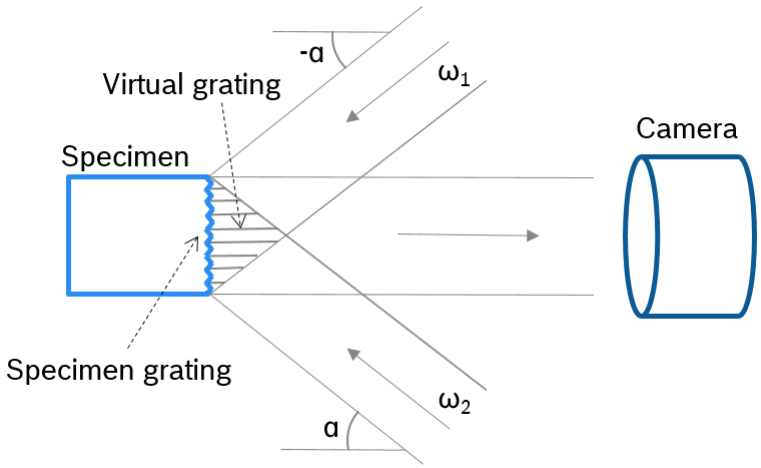

Figure 5.5.2: The specimen and reference grating interact with each other to form moiré pattern [143].

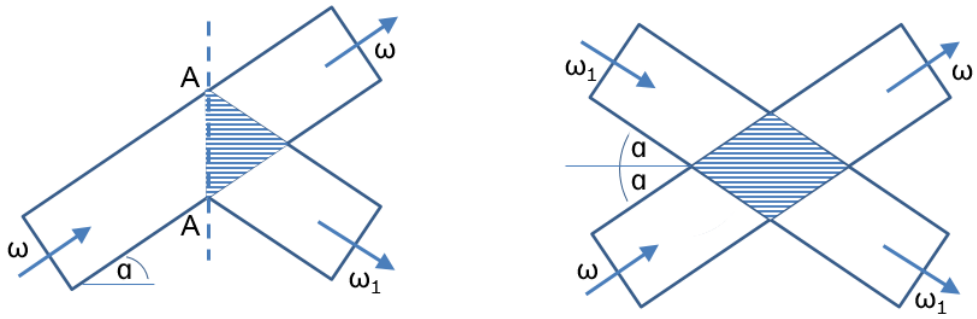

(a) (b)

Figure 5.5.3: Formation of virtual grating through (a) diffraction and (b) interference of two coherent beams [143].

$$U = \frac{1}{f_s} N_x \tag{5.5.1}$$

$$V = \frac{1}{f_s} N_y \tag{5.5.2}$$

Where:
U, V - displacements in x- and y-directions,
N_x, N_y - the fringe orders in x- and y-directions,
f_s - the spatial frequency of the virtual reference grating (2400 lines/mm).

After this, it is possible to calculate the in-plane strains based on the finite differences approximations of the respective derivatives:

$$\epsilon_x = \frac{\Delta U}{\Delta x} = \frac{1}{f}\left(\frac{\Delta N_x}{\Delta x}\right) \tag{5.5.3}$$

$$\epsilon_y = \frac{\Delta V}{\Delta y} = \frac{1}{f}\left(\frac{\Delta N_y}{\Delta y}\right) \tag{5.5.4}$$

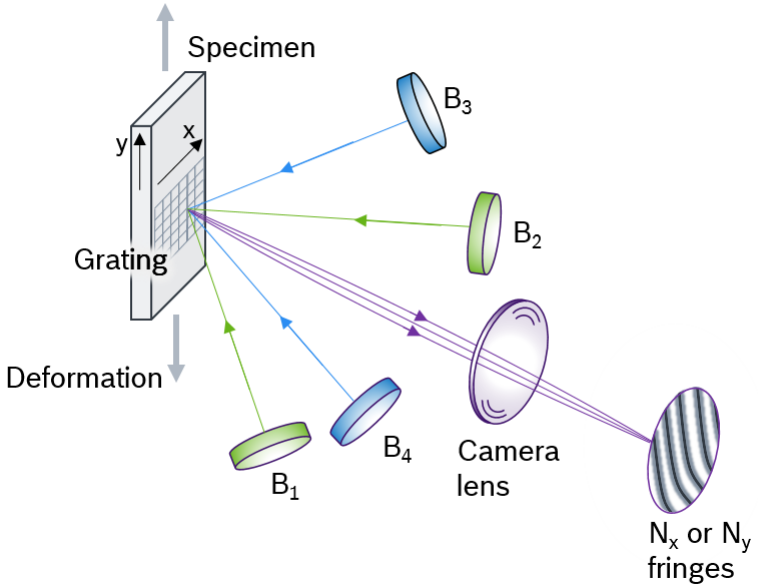

Figure 5.5.4: A general schematic of moiré interferometry. [150].

$$\gamma_{xy} = \frac{\Delta U}{\Delta y} + \frac{\Delta V}{\Delta x} = \frac{1}{f}\left(\frac{\Delta N_x}{\Delta y} + \frac{\Delta N_y}{\Delta x}\right) \tag{5.5.5}$$

Where:
ϵ_x, ϵ_y - normal strains,
γ_{xy} - shear strain.

These equations also allow for an intuitive interpretation of the fringe pattern—the strains are bigger in the regions where the fringes are denser. Additionally, if the calculation of stresses is necessary, it can be made based on the known stress-strain relations for the investigated material.

5.5.2 Measurement setup

In this investigation, the thermal deformation of an ECU subjected to the passive and active thermal cycling was analyzed using moiré interferometry. For the measurements, a portable engineering moiré interferometer (PEMI) and a convection oven were used. Figure 5.5.5 presents a schematic of the setup for real-time observation of thermal deformation; this setup minimizes the effect of vibration caused by air circulating inside the oven on the measurement [144]. This is achieved by mechanically coupling the optical part of the setup with the sample holder using a glass rod. Hence, all parts of the PEMI and the sample vibrate in unison, and all vibration effects on the measurement are cancelled. Additionally, a specimen is mechanically isolated from the oven, and no vibration from the oven is transferred to the experimental setup. Therefore, measurements can be made while the oven is being operated, thus maintaining a high measurement resolution. Thanks to the low thermal conductivity of glass, the heat transfer between thermal chamber and optical system is minimized.

The complete experimental setup is illustrated in Figure 5.5.6. The stress state in the ECU specimens was monitored by the stress sensor during the experiments. For the passive thermal condition, specimens were placed inside the convection oven, and the deformations were documented as a function of temperature. The minimum and maximum temperature was -40°C and 150°C respectively. For the active thermal condition, the specimens were tested under the natural convection condition at 25°C with 1.2 W of electrical power

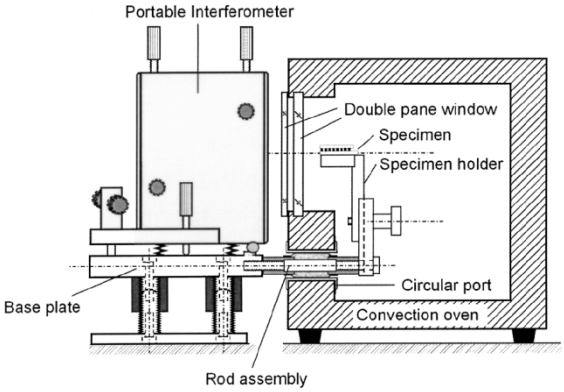

Figure 5.5.5: Schematic of the moiré setup for real-time observation of thermal deformation.

dissipated in each of the DPAK packages. Additionally, thermocouples were attached to different locations on the specimen surface to collect temperatures through DAQ during experiments.

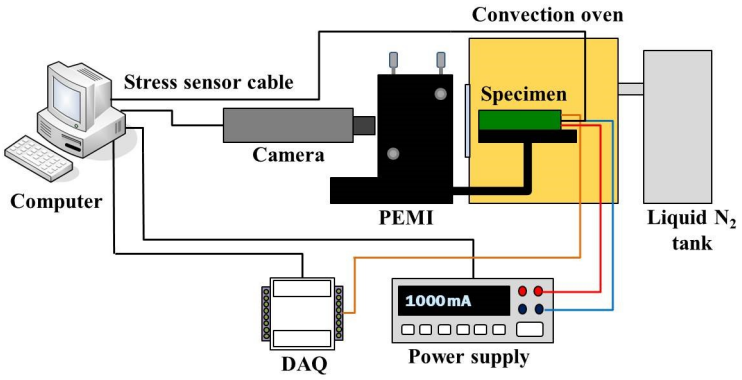

Figure 5.5.6: Schematic of complex experimental system.

Two additional sets of ECU specimens were designed and fabricated for thermal deformation analyses—one for passive and one for active thermal condition investigation. They were produced using the same materials and the same processes at the same manufacturers as the main test vehicles for this study. Thus, the transferability of the results between the two sets of test vehicles is ensured since the objective of this study is to validate the material behavior. The only modification to the main test vehicles is the positioning of the DPAK packages and stress sensors. In this case, the DPAK packages and stress sensors are placed on one side of the PCB to minimize the necessary field of view for the moiré interferometry. Additionally, these need to be aligned in a way that enables a cross-section through all the components at once. The specimens subjected to active cycling were designed in a way that can preserve functional electronic components (i.e., power packages for thermal cycling and stress sensors) even after making a cross-section needed to perform moiré interferometry experiments as presented in (a) and (b) of Figure 5.5.7). To prepare the samples for the moiré experiment, the test vehicles were ground flat to expose the Al bond, Cu leads, Cu pad, and DPAK mold, as shown in (c) and (d) of Figure 5.5.7. The specimen gratings (f_s = 1200 lines per mm) were replicated on the unusually large cross-sections (50 mm × 12 mm) using epoxy based adhesive cured at room temperature.

Each set contains two different configurations: unmolded ECU and molded ECU (see Figure 5.5.8), where two DPAK packages and one silicon based stress sensor were mounted onto the PCB.

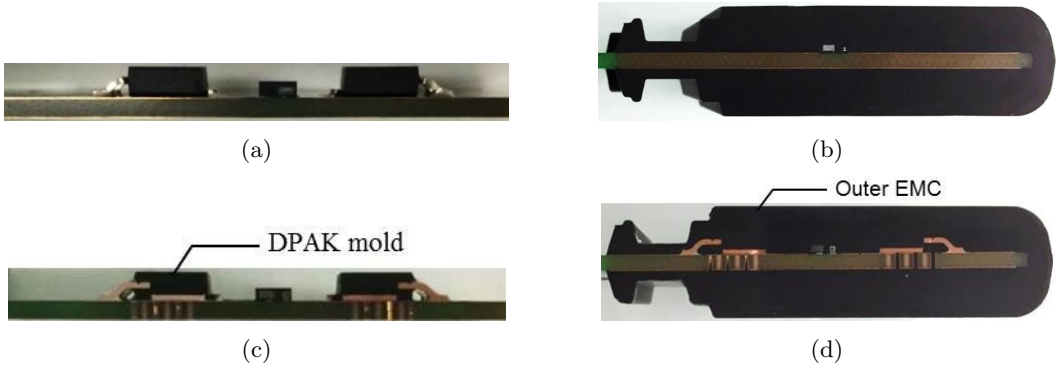

(a) (b) (c) (d)

Figure 5.5.7: Cross sections of specimens. The specimens for passive thermal condition are seen in (a) and (b). The specimens for active thermal condition are seen in (c) and (d).

(a) (b)

Figure 5.5.8: ECU configurations. (a) Unmolded configuration. (b) Molded configuration.

5.5.3 Results

Representative fringe patterns obtained at -40°C and 150°C are shown in Figures 5.5.9 and 5.5.10. The corresponding contour interval in the moiré fringe patterns amounts to 417 nm/fringe order. For a convenient analysis, the outlines of DPAK packages, stress sensor, and PCB were drawn onto the fringe patterns. The thermal deformations in the ECU specimens are very complicated. It is caused by the fact that the thermal and mechanical properties of the used materials are temperature dependent. The deformation patterns are quite different between the molded and unmolded ECUs because the outer EMC constrains the system significantly. The results revealed the effect of the outer EMC on the thermal deformations of ECU.

To quantitatively evaluate the deformation state in the investigated ECUs and the effect of the outer mold on the thermo-mechanical behavior of the system, the deformation was evaluated along the lines presented in (a) of Figure 5.5.11. As depicted in (b) of Figure 5.5.11, U displacements of the PCB along line 1 are almost the same in the unmolded and molded ECUs at -40°C. However, at 150°C the U displacement of the PCB becomes smaller in the molded ECU, which indicates that the material properties are dependent on temperature. It is worth noting that the outer EMC has a small effect on the U displacement of the DPAK package along Line 2, while it increases the V displacement of DPAK along Line 3, as presented in (b) and (c) of Figure 5.5.11. The thermal deformations on the cross sections of stress sensors on those two specimens are completely different, as shown in Figure 5.5.9 and Figure 5.5.10.

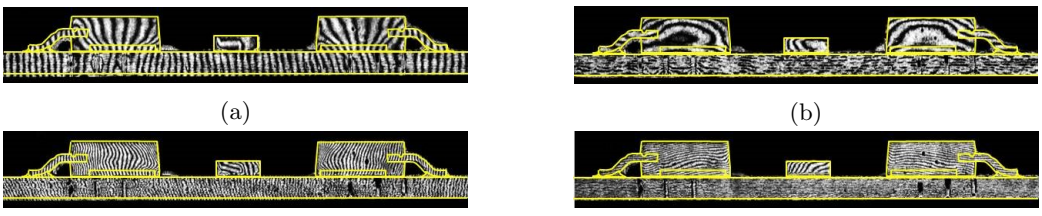

(a) (b) (c) (d)

Figure 5.5.9: Representative fringe patterns of unmolded ECU subjected to passive thermal condition. (a) U field at -40°C. (b) V field at -40°C. (c) U field at 125°C. (d) V field at 125°C.

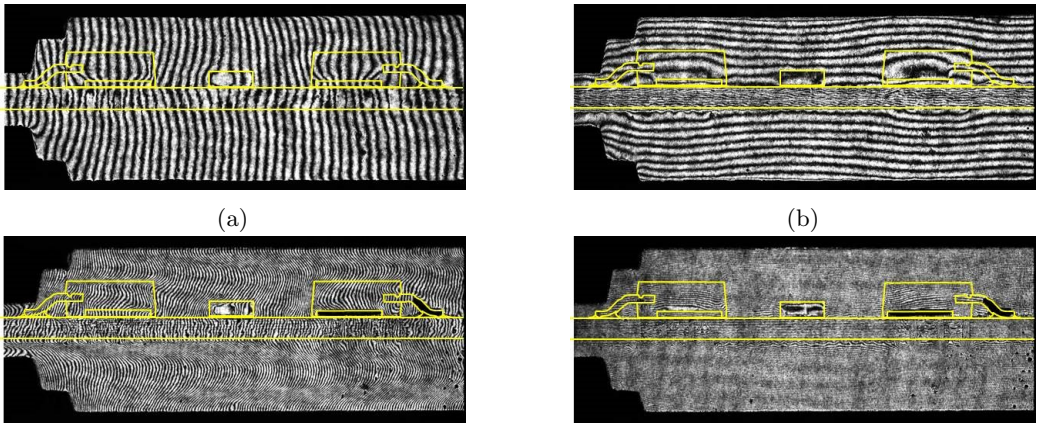

(a) (b) (c) (d)

Figure 5.5.10: Representative fringe patterns of molded ECU subjected to passive thermal condition. (a) U field at -40°C. (b) V field at -40°C. (c) U field at 125°C. (d) V field at 125°C.

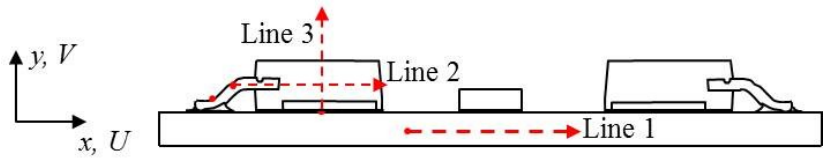

(a)

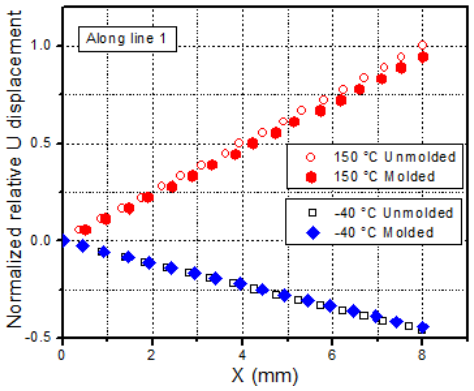

(b)

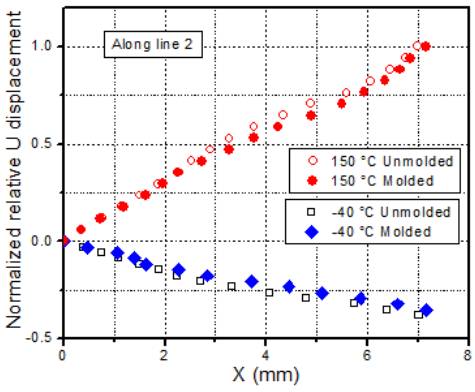

(c)

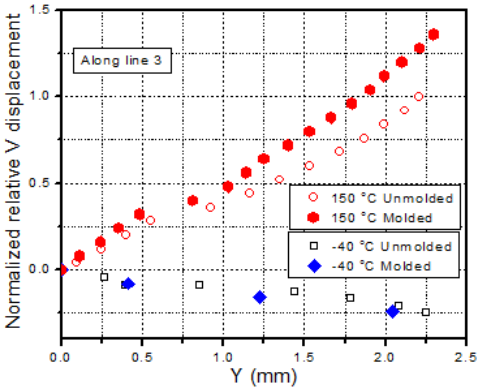

(d)

Figure 5.5.11: Experimental displacements on both the DPAK and the PCB. (a) Evaluation lines. (b) Results along Line 1. (c) Results along Line 2. (d) Results along Line 3.

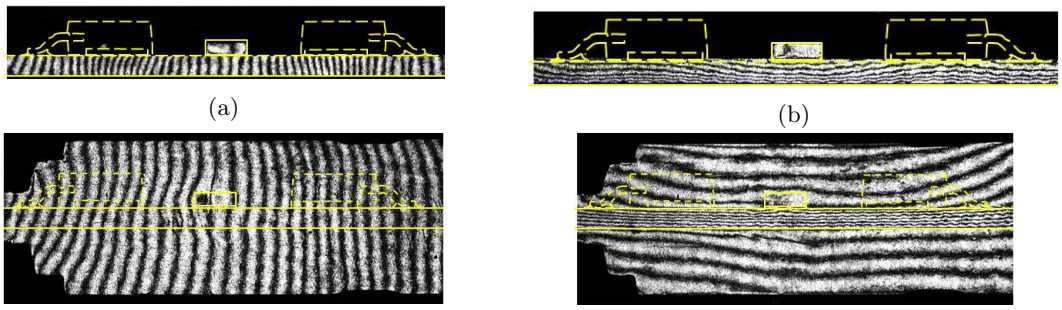

(a) (b) (c) (d)

Figure 5.5.12: Representative fringe patterns of the ECU subjected to active thermal condition. (a) U field of the unmolded sample. (b) V field of the unmolded sample. (c) U field of the molded sample. (d) V field of the molded sample.

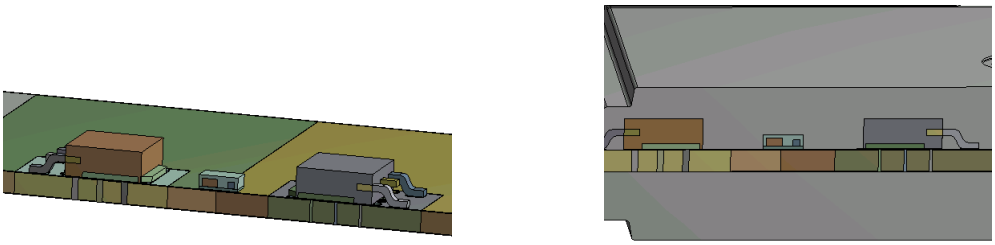

(a) (b)

Figure 5.5.13: 3D model of moiré specimens for the passive thermal condition. (a) Unmolded and (b) molded with outer EMC.

Figure 5.5.12 shows the fringe patterns under the active thermal condition. A denser U field fringe patterns in the PCB in the area of DPAKs indicate local heat generation. The warpage on PCB is evident in the V displacement field of an unmolded specimen. The outer EMC alleviates the warpage of PCB, as shown in Figure 5.5.12(b).

5.5.4 Simulation validation

Since the dedicated test vehicles were designed for purpose of this study and the specimens were cross-sectioned, a separate model with new geometry must be created. However, this study focuses on the validation of material behavior. The model geometry for both molded and unmolded cases is presented in Figure 5.5.13. The critical cross section of interest was placed in the same way as in the experiment; exactly as in the experiment, it exposes the components, namely the Al bonds, DPAK mold, and Cu pad. The properties of some materials like copper or aluminum are well known. The outer EMC, DPAK mold, and prepreg of the PCB have temperature dependent properties and occupy the majority of the volume inside ECUs. For this reason, the behavior of these materials are in the main focus of this investigation. The verification was performed by correlating the results from the FEM model and from the experiment under passive and active thermal conditions. Displacement results from the experiments and numerical simulation confirmed the accuracy of FEM modeling.

The displacement shapes are similar to experimental fringe patterns, as seen in Figure 5.5.14. Quantitative comparisons were done using the displacement values plotted along different lines. The results along Line 1, Line 2 and Line 3 for unmolded ECU are plotted in (a), (b) and (c) of Figure 5.5.15 respectively. For the molded ECU, the displacement results along Line 4 are illustrated in Figure 5.5.16.

The thermal simulation was carried out to obtain the temperature distributions at steady state for the active thermal condition case, as shown in Figure 5.5.17. The temperature differences within 4°C between

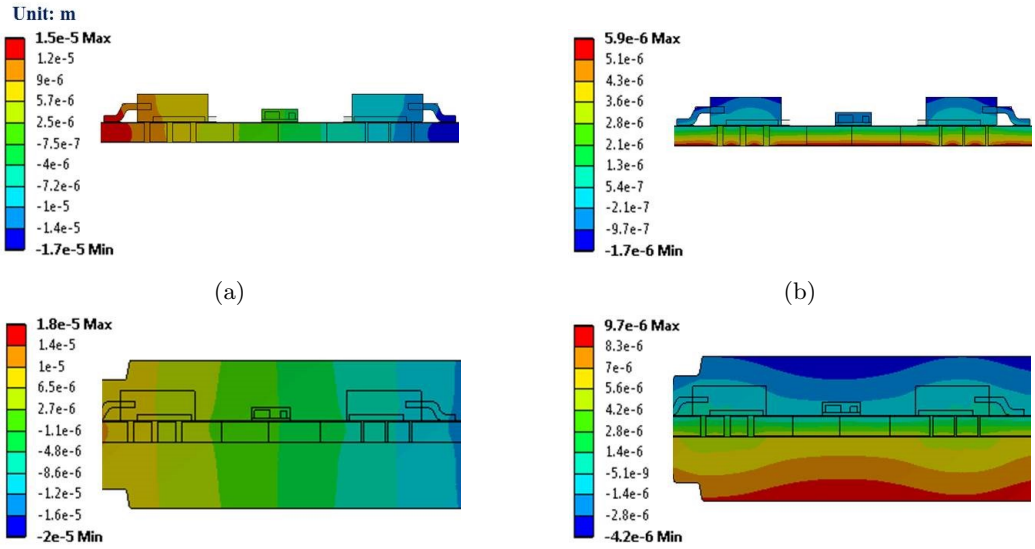

Figure 5.5.14: U and V displacements for a) unmolded and b) molded ECU at -40°C.

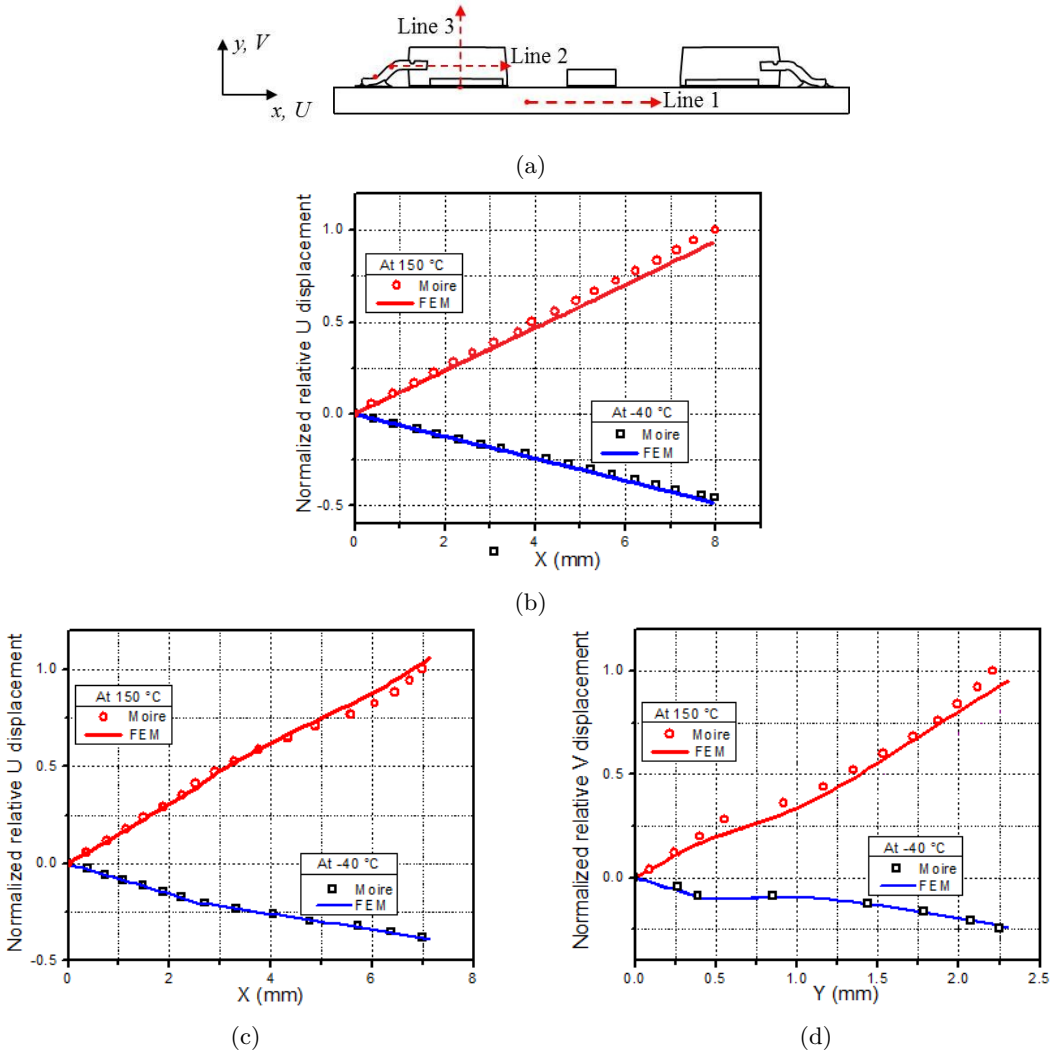

Figure 5.5.15: Experimental displacements on DPAK and PCB along lines shown in the insert.

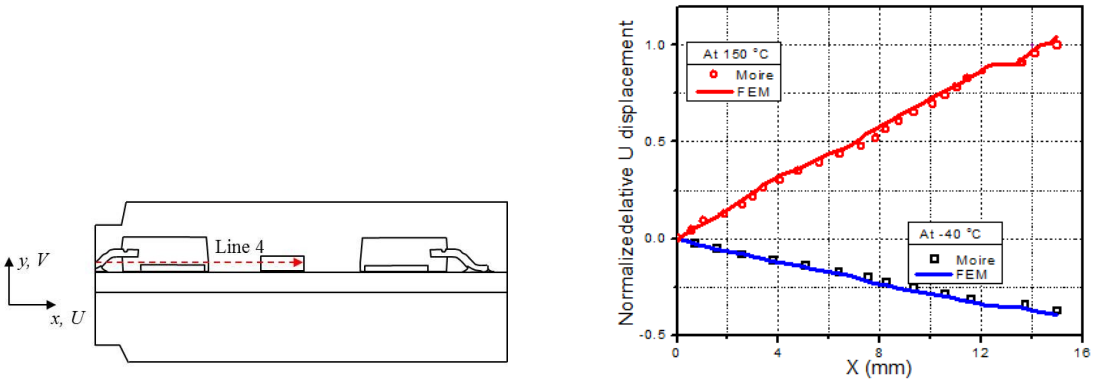

(a) (b)

Figure 5.5.16: Comparisons of U displacements on molded ECU along line 4 shown in the insert.

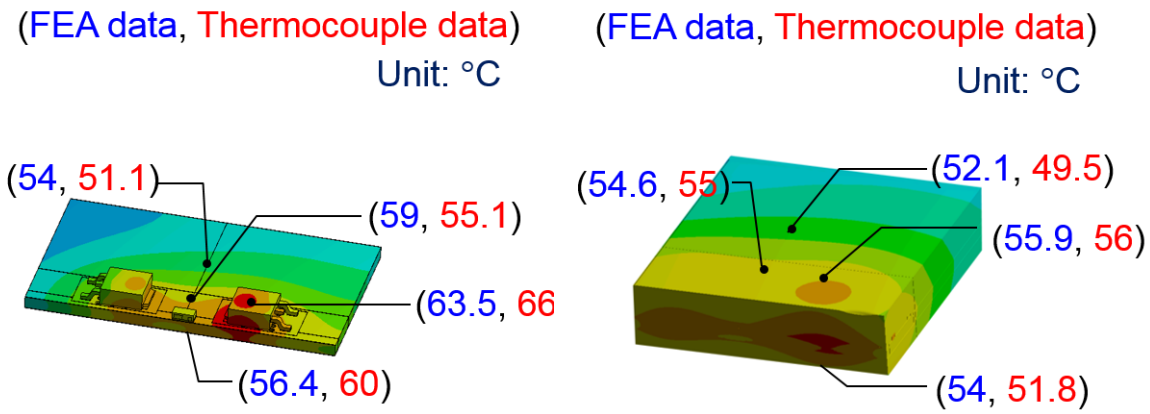

(a) (b)

Figure 5.5.17: Temperature distributions for (a) unmolded and (b) molded specimens at steady state.

numerical and experimental results were achieved. The maximum temperature inside the molded package was around 60.3°C, which is below the glass transition temperature of the DPAK mold, outer EMC, and prepreg.

The temperature distributions were then taken as an input load to the thermo-mechanical FEM model in order to study the thermal deformations of ECU during active operation. As shown in Figure 5.5.18, reasonably good correlations were obtained, and these confirmed the accuracy of FEM modeling. One of the factors that affect accuracy in this case is the fact that the temperature distribution prediction taken as the input load was calculated with a limited accuracy in the previous step.

The verified FEM model was further utilized in this thesis to study stress distributions in both a whole unmolded and a molded ECU package and to investigate the effect of outer EMC on a product's reliability.

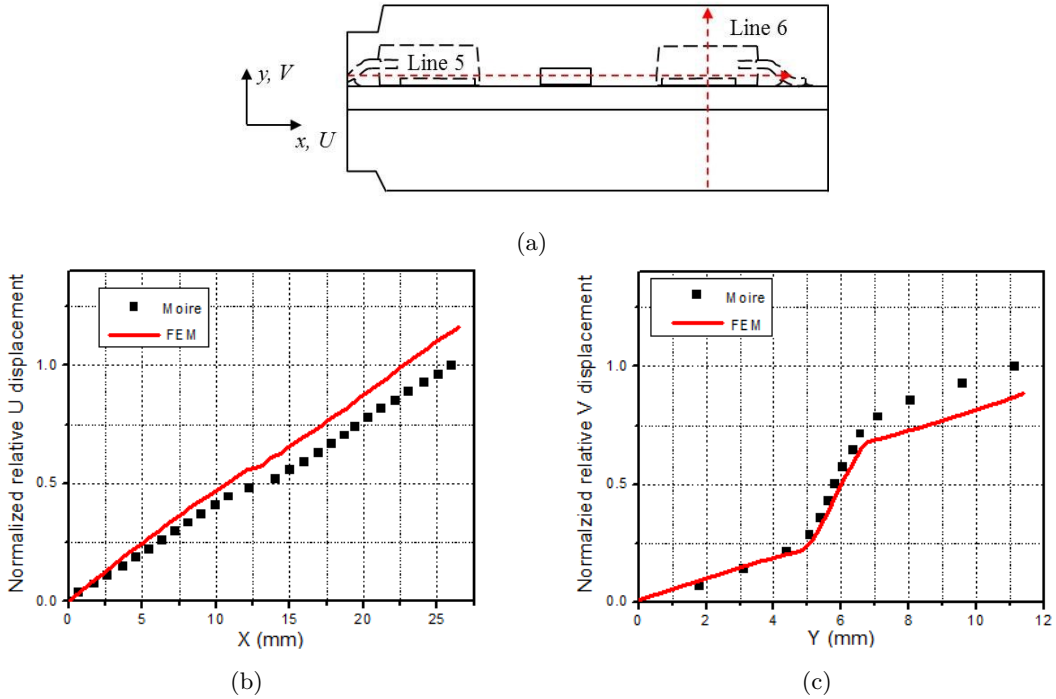

Figure 5.5.18: Comparisons of experimental and numerical results at active thermal condition along lines shown in the insert.

5.6 Summary

This chapter presents the details of the performed FEM modeling. First, the important steps of model preparation were described, including detailed geometry, material characterization, and modeling. To obtain a precise prediction of loading in the design elements—which are of interest from a reliability point of view—a series of consecutive simulations was performed, namely electrical, thermal, and thermo-mechanical simulations. A submodeling technique was then utilized in order to have the non-linear properties of solder and wire bonds to be taken into account in a computationally feasible way. This submodeling also enabled the creation of a very high quality mesh, especially in the area were the damage indexes should be evaluated. Additionally, a comprehensive verification of thermo-mechanical behavior of viscoelastic materials was conducted by means of moiré interferometry. The experiment was conducted under both active and passive thermal conditions, and it confirmed the accuracy of FEM model.

Chapter 6

Model-based approach

6.1 Introduction

This chapter develops a physics-of-failure prognostics approach for an ECU, in which loading conditions are monitored using the piezoresistive silicon stress sensor. The workflow of the proposed methodology is presented in Figure 6.1.1. First, a FMMEA is performed in order to establish possible damage mechanisms in an investigated system. Then, the available physics-of-failure models for the identified failure modes are reviewed and appropriate approach is chosen. Next, FEM simulation is executed in order to evaluate the damage parameters. Additionally, analysis of the results enables better understanding of the investigated system behavior under given load conditions. The reliability tests are defined and performed to verify the approach. During the temperature cycling the system is monitored using piezoresistive silicon stress sensor to gather the data about temperature and mechanical stress. The value of damage parameter and the monitored value of stress and temperature are related to each other by means of validated FEM model. This finally enables RUL calculation.

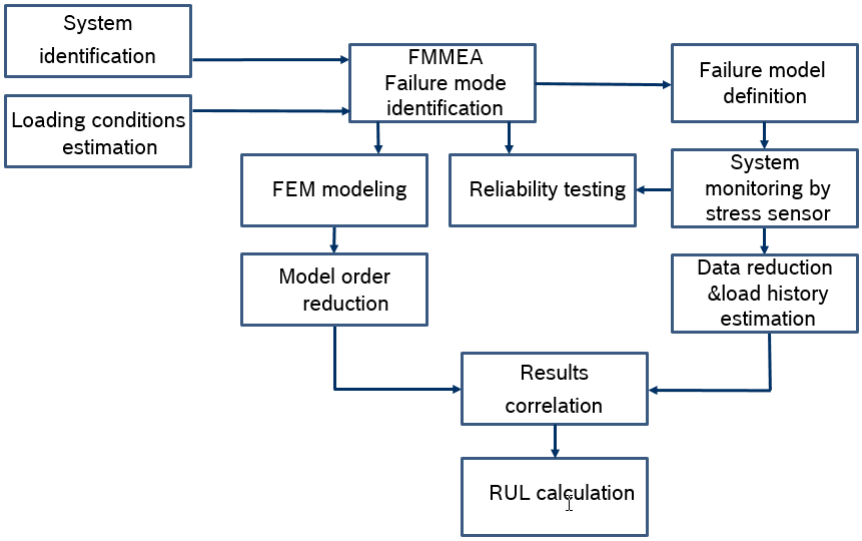

Figure 6.1.1: Proposed methodology of model based approach.

6.2 Failure mode identification

FMMEA was conducted as a first step in this study. Three major failure modes were identified:

- delamination between the molding compound and the copper lead frame (see Figure 6.2.1(a)),
- wire bond lift-off (see Figure 6.2.1(b)),
- solder joint crack due to fatigue (see Figure 6.2.1(c)).

Solder crack due to fatigue is a very common failure mode that has been investigated extensively in the literature [151]–[154]. The corresponding failure mechanism is the occurrence of cyclic thermo-mechanical stresses provoked by CTE mismatch between the materials that constitute electronic system. Similar to a solder joint failure, the failure mechanism in the case of a wire bond lift-off is the occurrence of the cyclic thermo-mechanical stresses on the wire bond foot. The wire bond that is expected to fail first is the thinner of the two bonds (with a diameter of 125 µm) that forms the electrical connection for the gate terminal. Delamination is caused by the weak adhesion between the molding compound and copper; specifically, it is a crack on the interface of the materials. The corresponding failure mechanism is the occurrence of the shear stress on the material interface that exceeds the adhesion strength. Delamination does not cause an electrical failure, but it does significantly accelerate other failure modes since it causes a larger cyclic mechanical load to act on a design element. In the analyzed case, a wire-bond lift-off is accelerated substantially by delamination between the molding compound and copper pins in the direct vicinity of the bond foot of the wire bond. Similarly, solder crack due to fatigue is accelerated by the delamination that occurs between the solder and outer molding.

All of above-mentioned failures are investigated in this work. To predict reliability accurately, the choice of an adequate physics-based model is necessary. In the following sections, the available models for the considered failures are discussed.

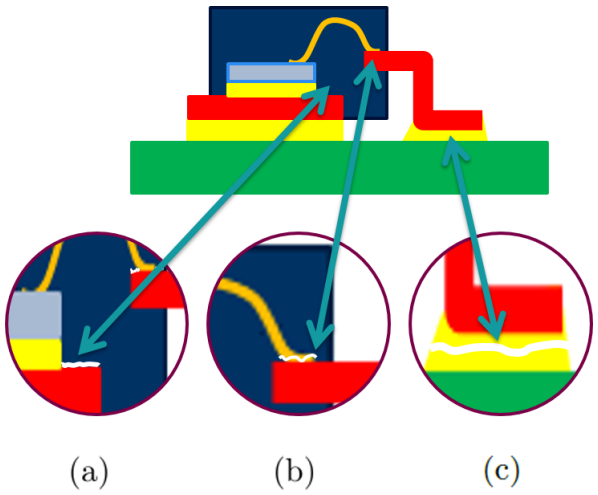

Figure 6.2.1: Expected failure modes. (a) Delamination between molding compound and copper lead frame. (b) Wire bond failure. (c) Solder joint failure [126].

6.2.1 Wire bond failure model

Wire bonds form electrical connections inside the component package. In power packages, they are subjected to large temperature swings. They are heated up not only passively by the heat dissipated in silicon die but also actively, since they may carry significant currents. The mechanical failures are caused by thermo-mechanical stresses that are provoked by different coefficients of the thermal expansion of silicon and aluminum. The forces acting in the system during thermal loading provoke repeated bending of the wire or stress between the bond pad and wire. Consequently, horizontal or vertical heel cracks may appear. The

most common relation that describes how the number of cycles to failure depend on certain chosen damage parameters is a simple power law equation [155]:

$$N_f = C_1(\Psi)^{(C_2)} \tag{6.2.1}$$

Where:
N_f - number of cycles to failure
Ψ - a damage parameter e.g. temperature range, mean temperature, current density, plastic strain
C_1, C_2 - constants, usually determined experimentally

One of the most popular fatigue models based on the power law is the plastic strain-based model described by the Coffin–Manson equation [156]. This model describes low-cycle fatigue behavior; a damage parameter in this model is the plastic strain PS induced per cycle (ϵ_{pl}). The main disadvantage of this approach is that plastic strain is not easy to evaluate. It can only be estimated by a finite-element analysis or other numerical methods. Therefore, the model cannot be easily validated. It can be only done using end of life tests of samples with various properties, such as their different geometries or materials. Although validation may be unfeasible at this point, the approach can still provide a comparative analysis of different designs, and it can be done based on numerical simulations.

Another very well-known model is Basquin's equation [157]. The damage parameter in this model is a stress range $\Delta\sigma$. It is a high cycle regime model—this means that it can be applied to the estimation of thermal fatigue life of wire bonds only when the stresses do not exceed yield stress. Here, the same considerations concerning the estimation of damage parameter as for the Coffin–Manson model also holds.

Aside from this, there is yet another highly popular lifetime model for wire bonds which uses the temperature range of the load cycle as a damage parameter. This model is based on an assumption that the damage is caused by the thermo-mechanical stresses introduced by differences in the coefficients of thermal expansion between silicon and aluminum. The thermal strain in this situation is linearly dependent on the temperature difference. A relation between fatigue lifetime and the temperature range can then take the form of a power law. The main advantage of this model is that it is very straightforward to implement because the temperature can easily be measured. However, its accuracy is limited; it is also used only in cases where the temperature range does not exceed 120°C [158].

Various other models do exist, and each one may use different parameters—such as the mean temperature or current density. There are also models that use a specific method, such as models based on Paris Law, fracture mechanics, or Arrhenius equation. A substantial disadvantage of all of these models is their assumption that wire bonds are subjected to regular load cycles, which in reality is rarely the case. In other words, irregular cycling should be taken into account, and the Palmgren–Miner rule can be applied for this purpose.

In this work, a model based on PSED as a damage parameter is implemented. Such an approach has an advantage over the above-discussed approaches in that it captures the accumulated damage more accurately. This approach takes the nonlinearity of a stress-strain curve for aluminum into account by using the hysteresis curve to calculate the damage parameter. In this way, it considers both stresses and strains acting in the design element. Additionally, the result depends not only on the temperature but also on the ramp rate and history of loading. However, similar to the strain or stress based models, the damage parameter cannot be easily measured. Thus, the approach in using a detailed FEM simulation was chosen to evaluate PSED in a wire bond.

6.2.2 Solder joint failure model

Solder joint reliability becomes an important issue as a result of constant decrease of interconnect size. It forms not only the electrical connection but also the mechanical bond between the component and the

substrate. Considering mechanical wearout mechanism, most failures are the effect of differences in the coefficient of thermal expansion (CTE) and resulting thermo-mechanical stresses. The PCB substrates have CTE much different than solder and other materials used in production of microelectronic packages, therefore substantial strains are induced that provoke the solder joint fatigue.

However, it is not easy to evaluate the reliability of solder joints. The analytical models present the simplistic view on the case and are not able to take into consideration all the factors, for instance complex geometries or material properties that change during temperature cycling. Yet, they are generally quick and easy to use. Numerical models can deal with complex geometries and material properties but they are time consuming and require validation through experiments.

The models for lifetime prediction of solder joints under thermo-mechanical loading utilize mainly plastic strain, creep strain and energy criterion as a physical damage parameters. The models based on plastic strains include mentioned before Coffin–Manson equation or Solomon and Engelmeier models. However, solder is expected to deform mainly due to creep behavior since in the typical application temperature lays relatively close to its melting point (for lead-free solder, the melting temperature is typically 217°C). The models based on creep strain as a damage parameter include Knecht and Fox or Syed models [159]. Two mechanisms of creep behavior are identified—matrix creep and grain boundary creep. Knecht and Fox introduced a model based on creep shear strain range in the matrix, taking into account the microstructure of solder [160]. Syed proposed a model that takes both matrix and grain boundary creep into account [161]. These models provide more comprehensive lifetime modeling but they are not able to capture the complex deformation fatigue as they neglect the plastic and elastic strain components. In some situations, like when temperature change has high ramp rate, plastic strain cannot be neglected.

Another group of fatigue models for solder uses hysteresis energy terms as a damage parameter. This group contains models that employ different energy components (elastic, plastic, creep) and different lifetime relations [159]. In this work, a model based on power law that uses CSED as a damage parameter is implemented. It was introduced by Darveaux in [162]. This model takes into account the hysteresis of strain-stress curve for solder. It has the advantage that it takes into account the nonlinear behavior of solder which is affected by the loading conditions. It is worth to notice that this model predicts only the number of cycles needed to initiate the crack and is not applicable for crack propagation. Usually, FEM simulation is performed to estimate CSED values. This approach was also applied in this work; a detailed model, which enables evaluation of mechanical loads in the solder joints was created.

6.2.3 Delamination

Delamination is one of the considerable problems in packaging industry, as it influences the reliability of a whole package. Delamination does not cause immediate failure but it often leads to acceleration of other failure modes. It damages the thermal interface, what can lead to overheating. Moreover, it increases the mechanical stress acting on the other design elements, what leads to acceleration of various fatigue related failure modes. In large molded ECUs there are couple of interfaces where the delamination can occur—these include interfaces between the molding compound and cooper lead frame, between molding compound and silicon chip, between outer molding compound and PCB etc.

Various mechanisms may provoke delamination. When the stresses are high enough to surpass adhesion strength, the delamination at the interfaces begins. The stress may be induced by e.g., differences in CTE, in-plane shear stiffness mismatch or even mismatch in Poisson ratios. It can be also initiated during manufacturing process as a consequence of differences in the thermo-mechanical properties. Other factor that could initiate delamination is the appearance of micro cracks somewhere near the interface. Usually, the delamination is initiated in a few places at the same time. It propagates during application of a component, thus compromising the reliability.

To model this type of failure, typically the fracture mechanics is applied [163]. There is no general rule that states when the delamination should be detected or how widespread it has to be in order to classify it as failure. It is much too complex, as it depends on the interface where the delamination occurs, the geometry of the package, and the cyclic stress conditions. These considerations are beyond the scope of this thesis. Here, the influence of a delamination on the wire-bond lift-off and solder fatigue is investigated.

6.3 Physics-of-failure model creation

After choosing the appropriate failure models, it is necessary to establish all needed parameters. The workflow of a failure model creation is presented in Figure 6.3.1. To calculate the values of damage parameters accurately, it is crucial to perform a detailed FEM modeling. The simulation approach is described in Chapter 5. Here, the results of modelling are presented and analyzed. Additionally, the model should be validated by means of experiment. Various test vehicles should be prepared to obtain different stress levels in the critical design elements. The details of the approach are presented in the following sections.

6.3.1 Modeling results

In this section, the results of modelling are demonstrated. Separate models were created for all the test vehicles and loading conditions used in the reliability testing. In total, four different cases were calculated, namely using a molded vehicle and an unmolded vehicle being subjected to both passive loading and active loading.

As mentioned, the damage parameters were evaluated in a critical layer where the failure is expected. Values of both of damage indicators—namely CSED for solder joints and PSED for wire bonds—vary during the first couple of cycles because of the time dependent properties of materials within the system. To obtain a converged value of damage parameters, the simulation contained three load cycles. Figure 6.3.2 presents the evolution of the accumulated CSED and PSED during the thermal cycling. The presented values are normalized to the maximal calculated value of CSED and PSED in order to observe the relative changes of the values between cycles. Within the three cycles, the accumulated CSED and PSED has changed by 1.3% and 0.8% respectively. This change would lead to a 1.2% error in calculation of solder joint lifetime and a 0.5% error in the calculation of wire bond lifetime. Still, all the values of PSED and CSED parameters were extracted from the last calculated cycle to ensure correctness of the approach in all simulated cases. The values that are taken into account as a damage parameter are marked in Figure 6.3.2.

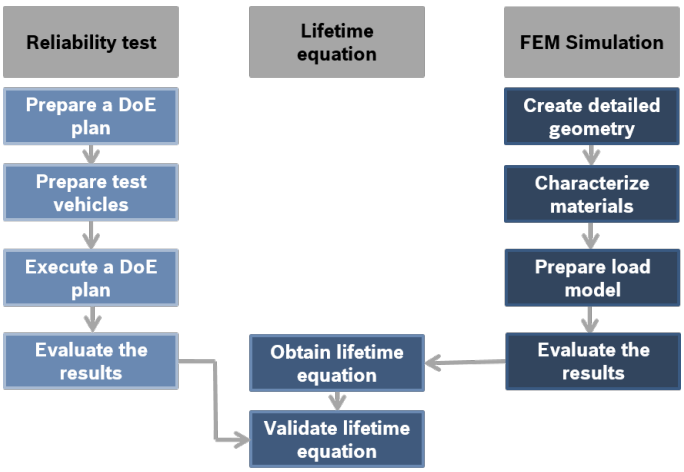

Figure 6.3.1: Physics-of-failure model creation workflow.

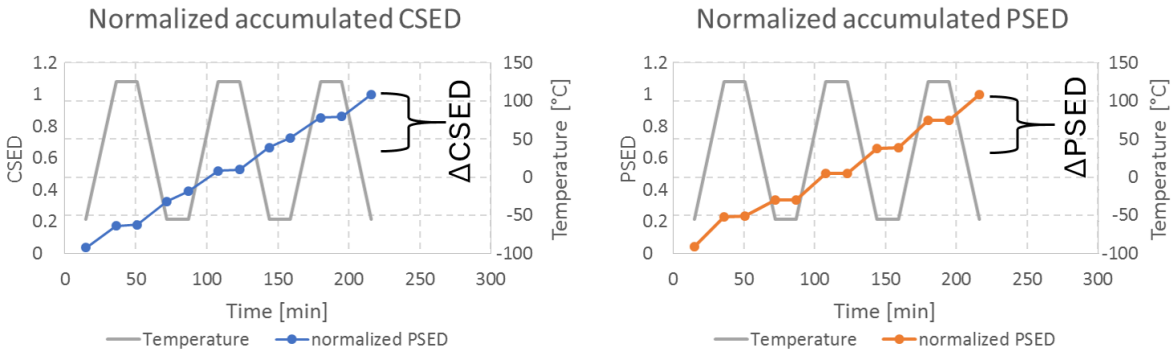

(a) (b)

Figure 6.3.2: The evolution of damage parameters during first three cycles of simulation a) CSED b) PSED.

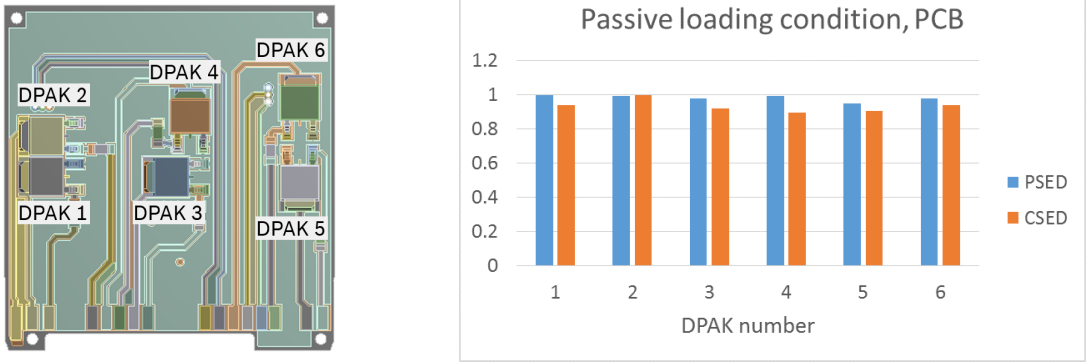

(a) (b)

Figure 6.3.3: (a) Numbering of DPAKs in the test vehicle. (b) Normalized values of PSED and CSED for every DPAK package during passive cycling loading of bare PCB.

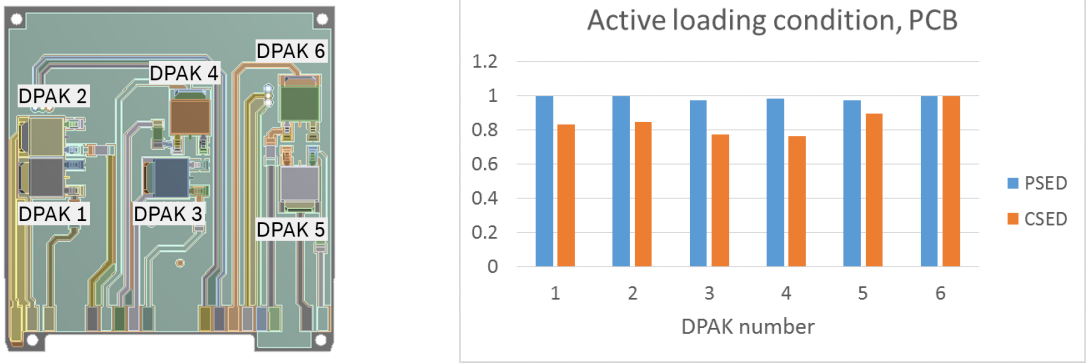

(a) (b)

Figure 6.3.4: (a) Numbering of DPAKs in the test vehicle. (b) Normalized values of PSED and CSED for every DPAK package during active cycling loading of bare PCB.

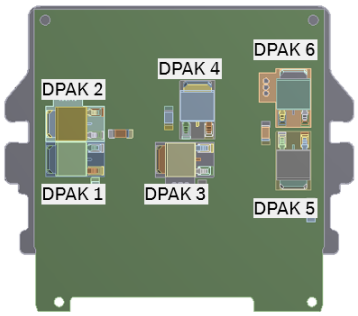

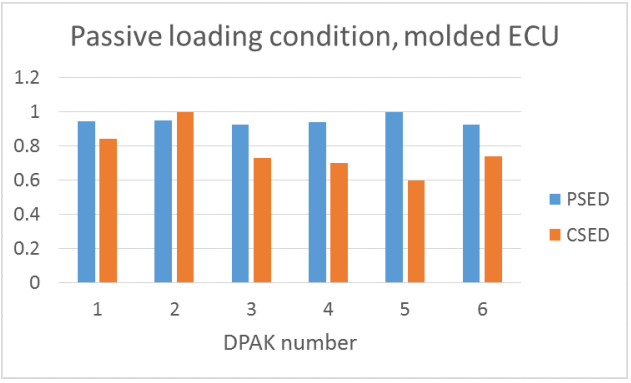

(a) (b)

Figure 6.3.5: (a) Numbering of DPAKs in the test vehicle. (b) Normalized values of PSED and CSED for every DPAK package during passive cycling loading of overmolded PCB.

Figures 6.3.3 to 6.3.5 show the normalized results for respective DPAK packages; in particular, Figure 6.3.3 presents the results for a bare PCB test vehicle subjected to passive thermal condition. Here, the values of the PSED parameter were similar for all packages, and they did not vary more than 5%. This is caused by the dominant role of the local deformation state inside the package on the load acting on the wire bond. The CSED values varied more significantly, the difference between smallest and largest value amounts to 12%. The smallest value of CSED is observed in DPAKs 3 and 4; these are located in the middle of the PCB where the induced stresses are the lowest.

Figure 6.3.4 depicts the results for the PCB test vehicle which was subjected to active thermal condition. In this case, again the PSED value is comparable for all the DPAKs, and it does not vary more than by 3%. CSED is largest in DPAKs number 5 and 6, which are at the edge of the PCB. There, the temperature rise caused by power dissipation in components is the lowest, which causes a larger local deformation at negative temperatures than in other parts of PCB.

Finally, in Figure 6.3.5 the results concerning passive thermal condition for overmolded case are shown. Again, the values of PSED do not vary significantly; the difference between the smallest and largest value reaches 7%. The variation in CSED values is much more significant with a 40% difference between the largest value in DPAK 2 and the smallest value in DPAK 5. Overall, the smaller values of CSED can be observed for DPAKs 4 to 6 that are oriented parallel to the longer PCB edge. This causes a different stress state, as these packages are less stiff in the bending direction.

Figure 6.3.6 presents the comparison of PSED and CSED values for different test vehicle types. The CSED is largest in the case of active cycling of a bare PCB followed by passive cycling of PCB. The PSED value is largest for the overmolded test vehicle subjected to active and passive cycling. This means that the solder joints will fail faster in PCB test vehicles that in molded ones. Then, the wire bond will fail faster in the case of overmolded modules. This is caused by the constraint introduced by the outer mold that prevents the deformation of a PCB and introduces more stress inside the components.

6.3.2 Reliability testing

To complete the physics-of-failure model, it was necessary to perform reliability tests. The workflow of prepared trials is shown in Figure 6.3.7. Two versions of test vehicles were designed and fabricated—bare PCBs and overmolded modules. Each group was divided in two parts; one of them was subjected to a passive condition, and the other was subjective to a combined active and passive thermal condition. The detailed test conditions are presented in Figure 6.3.8 and the testing setup is shown in Figure 6.3.9. The

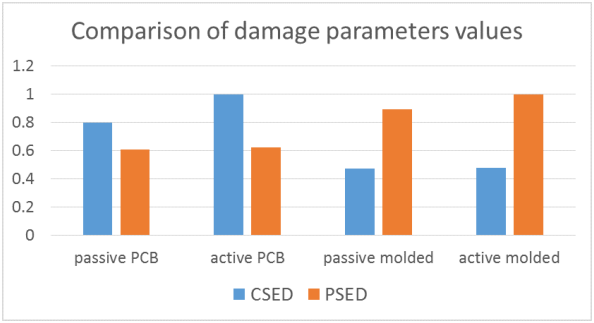

Figure 6.3.6: Comparison of the damage parameters between different samples groups.

samples were cycled passively in a convection oven between -55°C and 125°C with 15 minutes dwell time. Additionally, for active loading condition, 1W power was dissipated in every DPAK at -55°C hold time. The temperature and local stress conditions were monitored using the piezoresistive silicon stress sensor in real time for the whole duration of the testing. Additionally, a periodical examination using scanning acoustic microscopy (SAM) and electrical testing was performed.

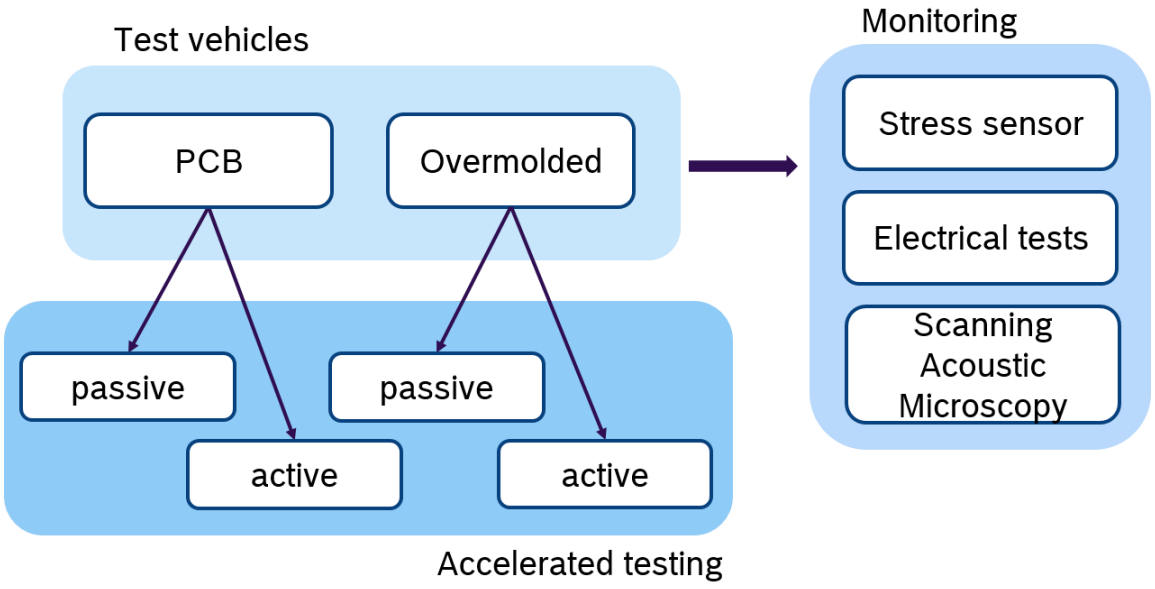

Figure 6.3.7: Reliability testing workflow.

An example of measured stress evolution over one thermal cycle is presented in Figure 6.3.10. Both measured stress values decreased as the temperature increased as shown in Figure 6.3.10(c) and (d). This could be caused by the fact that the stress free temperature for the investigated test vehicle was 175°C; it is a temperature at which transfer molding is performed. Naturally, the largest stresses were observed at -55°C, as it is the most distant point from stress free temperature. The lowest value of stress difference at -55°C was recorded at Cells 6 and 7, which are located at the edge of silicon die as shown in Figure 6.3.10(b). These are the only two cells where the difference stress has a positive value. This means that part of the chip is dominated by an x-component of stress. Further away towards the neutral axis of the package, the value of the stress difference decreases; in the middle in Cells 3 and 10, it is dominated by the y-component of stress. The largest negative value of stress is observed in Cells 11 and 12, where are on the bottom edge of the sensor. It has to be taken into account that the LGA package construction is not symmetrical in the y-direction. Additionally, the shape of silicon die is rectangular with a longer horizontal edge. This causes a clear dominance of y-direction stresses throughout the chip, which is most visible on the horizontal edges of the chip. The measured values of shear stress are much smaller than the values of difference stress. In fact,

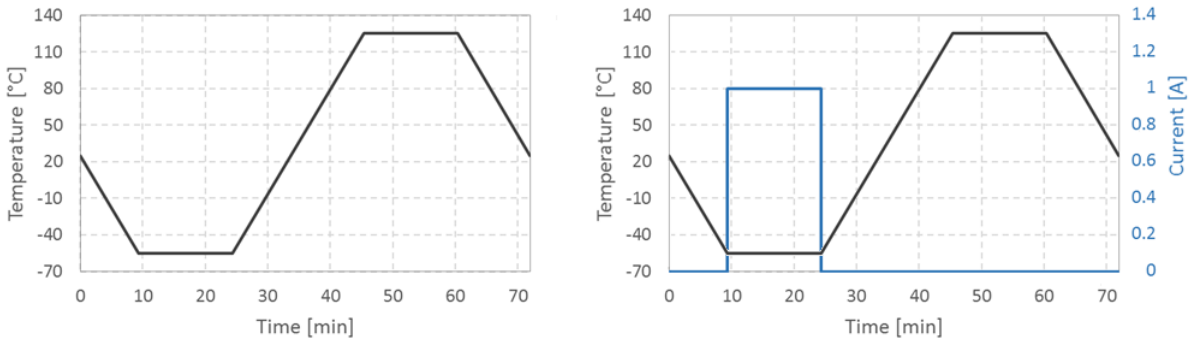

(a) (b)

Figure 6.3.8: The loading conditions used in reliability testing. (a) Passive loading condition. (b) Active loading condition.

Figure 6.3.9: Reliability testing setup.

the forces that cause xy-shear stress were minimal in the considered construction.

In Figure 6.3.11, the stress evolution over the initial 50 hours of thermal cycling is presented; the measured temperature, the difference stress measured in cell 1, and the shear stress measured in cell 1 are shown in (a), (b), and (c) of the figure respectively. The temperature cycles are regular and no variation in time was observed. In the case of stress difference, a slight variation can be noticed in the few initial cycles, and eventually the stress stabilized. In the case of shear stress, the variation in the initial cycles is also clearly visible, but additionally the stress drifted over the first 20-30 cycles, until it eventually stabilized afterwards. These variations are caused by initial relaxation and humidity uptake.

In order to track the variation of stresses in all measurement cells over large number of cycles the stress values at a maximal and minimal temperatures was extracted from cycling data as presented in Figure 6.3.12. The difference stress evolution at 125°C, the difference stress evolution at -55°C, the shear stress evolution at 125°C and the shear stress evolution at -55°C are depicted in (a), (b), (c) and (d) of Figure 6.3.12 respectively. The observed variations in the stress values at the beginning of thermal cycling are much more evident in the measurements at an elevated temperature. However, the initial change at low and high temperatures were of the same magnitude. The absolute values of measured stresses were much larger at -55°C. It is interesting to note that the change in the initial few cycles had a different direction in Cells 6 and 7, which are on the edge of silicon die (see Figure 6.3.12(a)). This is caused by the dominance of the x-direction stress in the region of the silicon die where Cells 6 and 7 are located. As mentioned, the y-component of stress is dominant in the remainder of the chip.

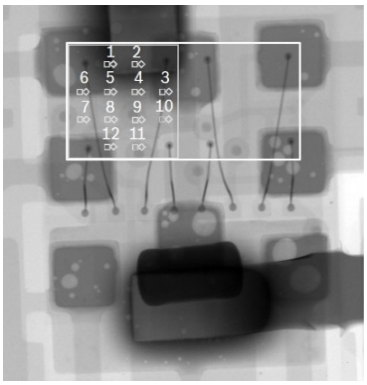

(a)

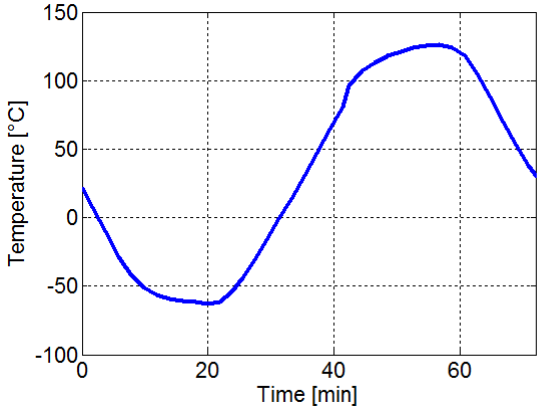

(b)

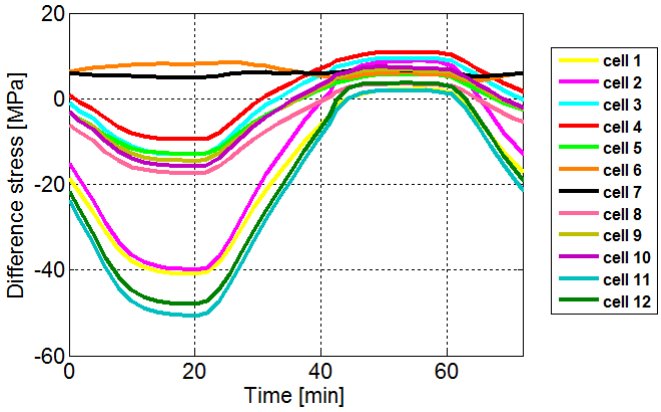

(c)

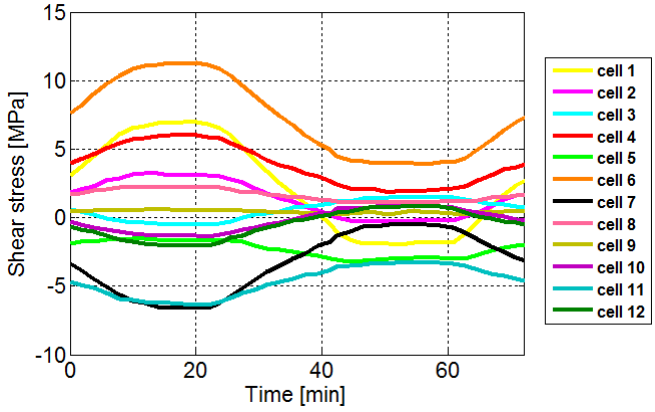

(d)

Figure 6.3.10: Results of system monitoring over one cycle. (a) Measurement cells. (b) Measured temperature. (c) Difference stress. (d) Shear stress.

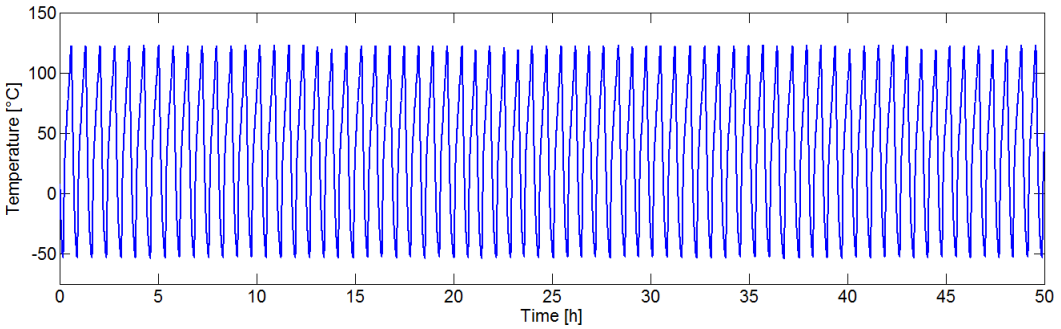

(a)

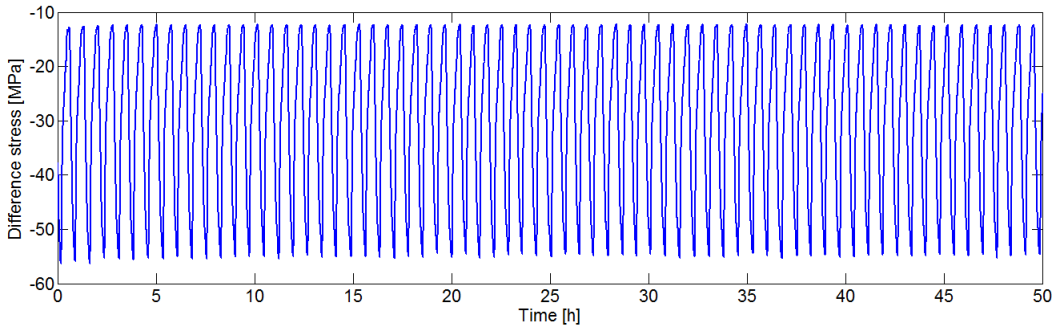

(b)

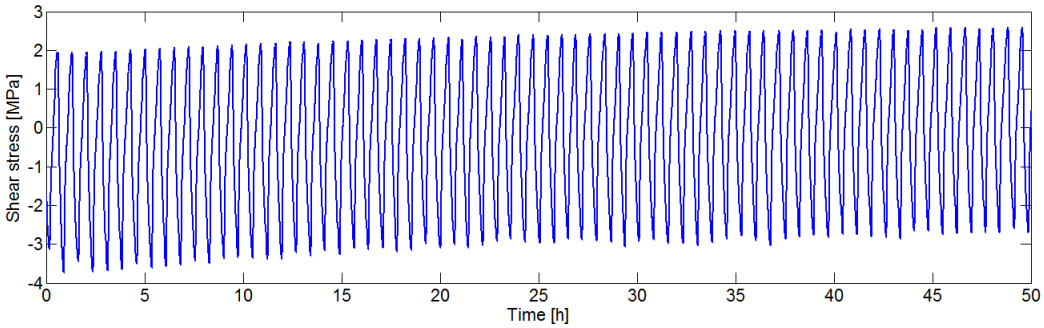

(c)

Figure 6.3.11: Results of system monitoring over multiple cycles. (a) Measured temperature. (b) Difference stress. (c) Shear stress.

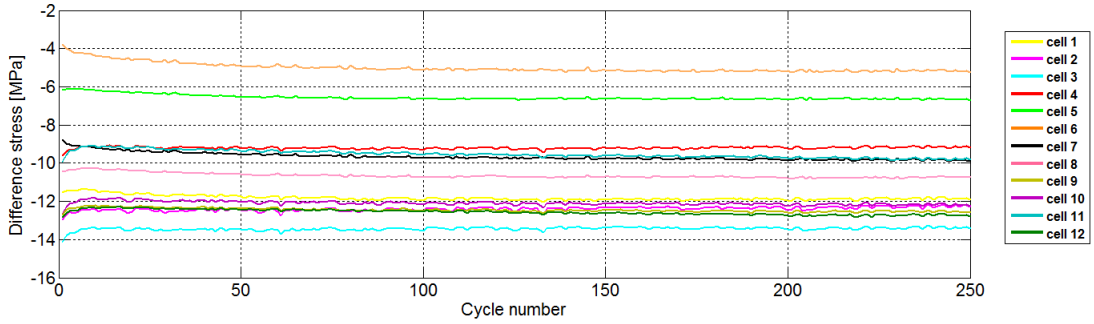

(a)

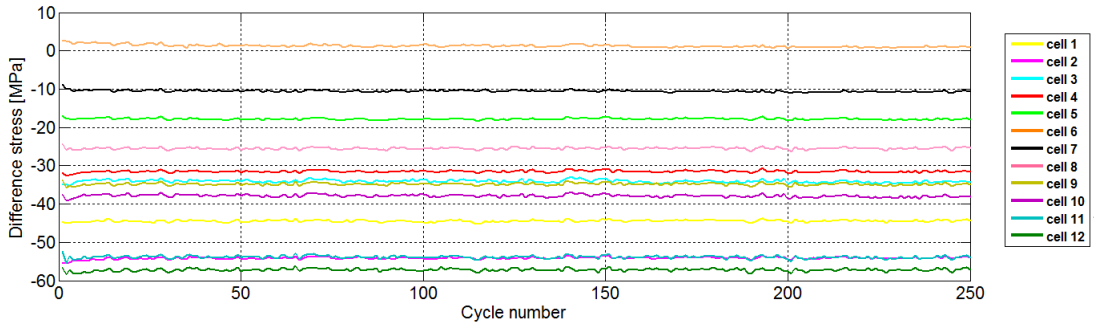

(b)

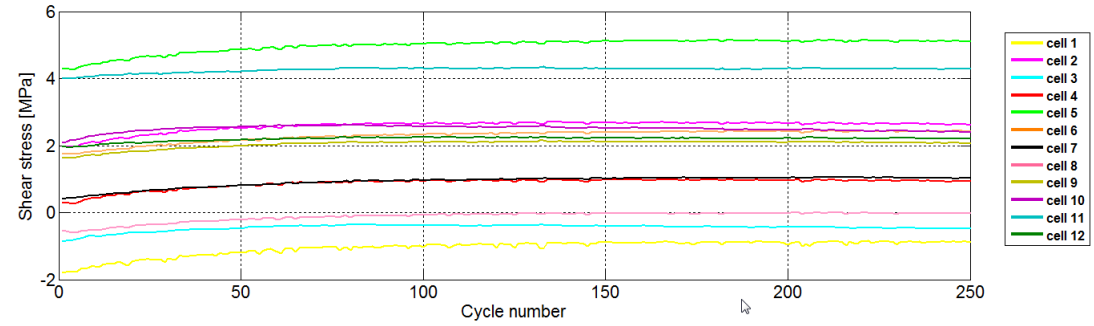

(c)

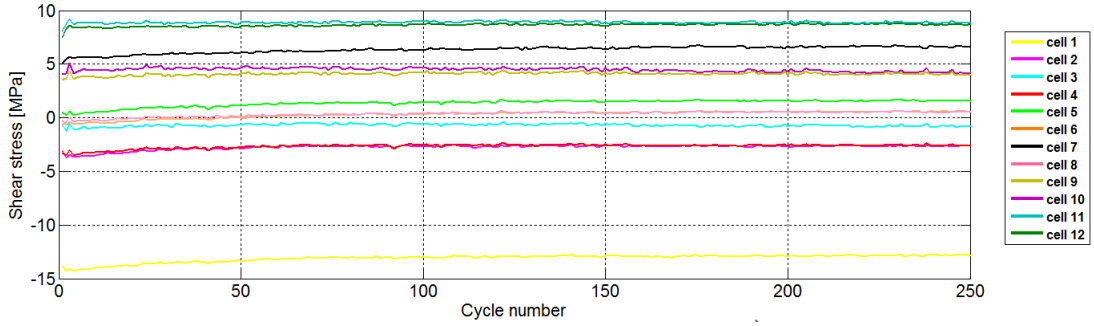

(d)

Figure 6.3.12: The stress evolution during thermal cycling. (a) Difference stress at 125°C. b) Difference stress at -55°C c) Shear stress at 125°C. d) Shear stress at -55°C.

6.4 RUL calculation

This section presents the RUL calculation done based on the developed failure models and monitoring data gathered during reliability testing. It should be noted that during reliability testing, failure was not observed, and thus the failure model could not be validated. Hence, the results presented in this section are purely illustrative, and they have been included only to demonstrate the developed approach.

The total predicted lifetimes for all calculated cases are summarized in Table 6.1. In all cases, the test vehicles subjected to active cycling will fail faster than the respective sample subjected to passive cycling. In the case of bare PCB samples, the failure mode that will likely occur first is a wire-bond lift-off. However, in the case of molded samples, solder joint will likely break first. The outer mold decreases the total lifetime of wire bonds and increases the total lifetime of solder joints. This is caused by the fact that the outer mold induces compressive stresses in solder joints. At the same time, the construction becomes stiffer; this prevents the package from deforming freely and causes larger stress amplitudes inside DPAK package, thus accelerating wire-bond lift-off.

Table 6.1: Predicted life for investigated test vehicles (in cycles)

Element	Bare PCB		Molded PCB	
	Passive	Active	Passive	Active
Solder	2955	2776	7469	7448
Wire bond	5486	5147	3222	2719

The total number of completed thermal cycles is 600, and until then no failure was observed. This is in accordance with the presented calculated lifetimes, as the fastest failing component should brake at around 3000 cycles. The tests were not continued because of time limitations for this research.

In Figure 6.5.1, the in-situ RUL calculation for the investigated test vehicles is presented. At every cycle, a new value of RUL is calculated based on the signal from stress sensor and damage parameters calculated by means of FEM modeling. The use of a stress sensor measurement for system monitoring provides advantages such as the possibility to detect the setting of material parameters or changes due to humidity intake. In the case presented in Figure 6.5.1, a regular series of load cycles is provided. In the case of an irregular load profile, the Miner's rule can be applied for RUL calculation. Additionally, a model order reduction method should be applied in the future in order to enable an in situ evaluation of damage parameters.

6.5 Summary

This chapter presented a model-based approach for PHM that uses a piezoresistive stress sensor for system monitoring. First, an FMMEA was performed to identify the most critical design elements in the investigated system, which turned out to be wire bonds and solder joints. Then, appropriate failure models were chosen. The failure model for wire bonds and for solder is based on PSED and on creep strain energy density respectively. The damage parameters were calculated based on a detailed FEM analysis. After establishing the model of failure for both design elements, their total lifetimes were estimated. Results showed that for overmolded samples, the failure that would occur first was wire-bond lift-off. In the case of a bare PCB, the solder joint would fail first. Reliability tests were then designed and performed to verify the approach. It was observed that there are changes in the stress values as measured by the piezoresistive sensor caused by material setting and humidity uptake. One point to note is that the 3000 cycles—which theoretically should lead to a failure—have not been performed. Finally, a methodology to calculate the RUL in situ was presented. In the future, a model order reduction should be implemented to allow for the evaluation of the damage parameters in situ. Additionally, a Miner's rule should be used to consider the cycles of different amplitudes.

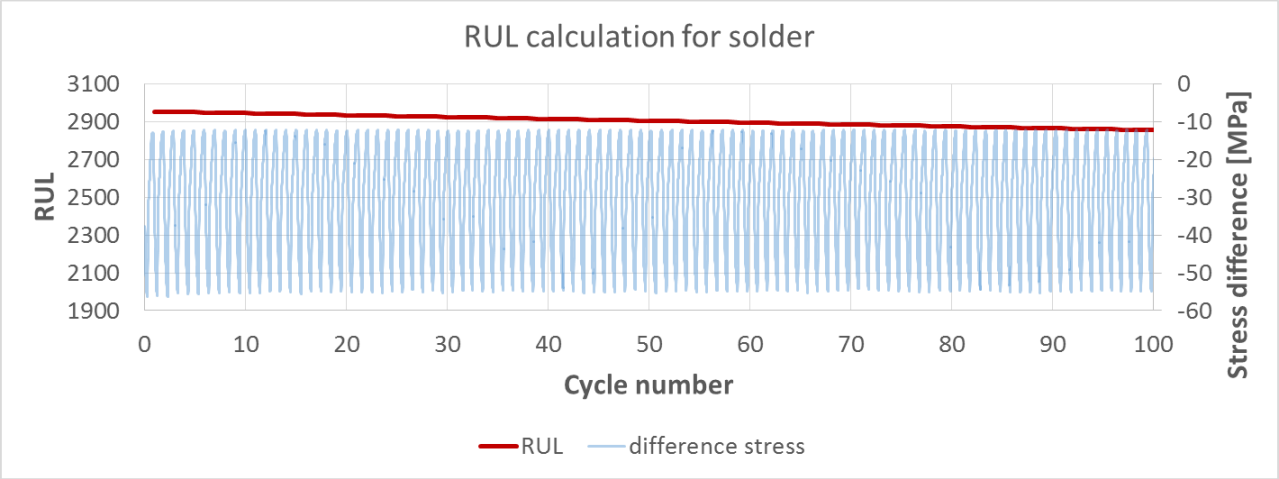

(a)

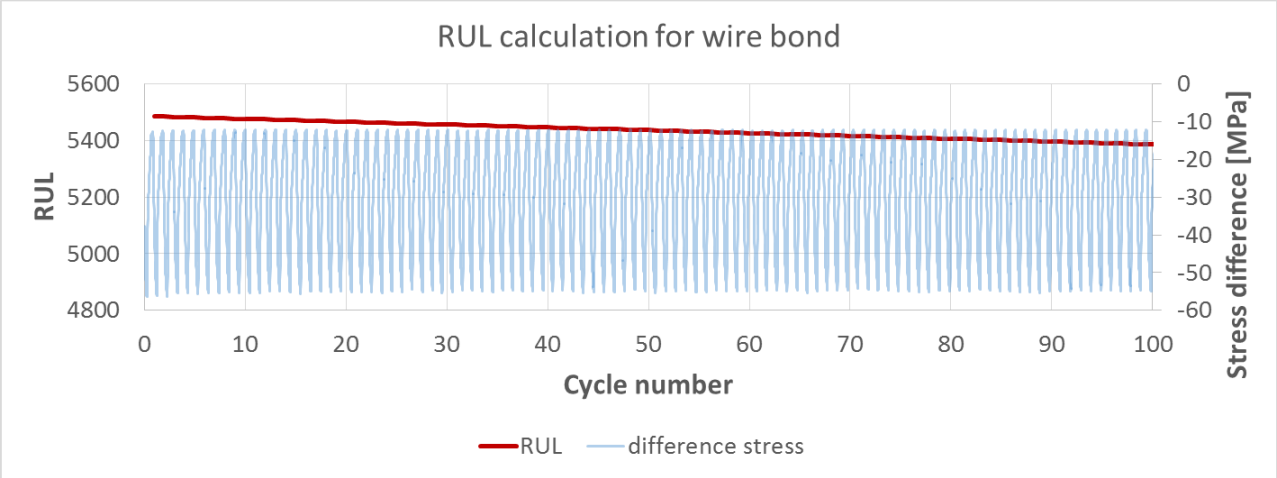

(b)

Figure 6.5.1: The RUL calculation for (a) solder joints and (b) wire bonds.

Chapter 7

Data-driven approach

7.1 Introduction

In this chapter, the piezoresistive silicon-based stress sensor is studied for the application in a data-driven approach to PHM. It has been shown already that delamination can be detected by sensing the signal change of the sensor [164]. However, a systematic study regarding how different failures can affect the sensor output has not yet been conducted.

First, an FEM analysis was conducted to fill this gap. Various failure modes were introduced into the validated model (presented in Chapter 5), and the virtual response of the sensor was investigated. Specifically, three failure modes have been investigated; they were chosen based on the performed FMMEA described in Chapter 6. The first of these was delamination in the area of the sensor as shown in (a) of Figure 7.1.2. This failure should give the largest response of a sensor. The second one was delamination in the DPAK area (see Figure 7.1.2(b)) which investigates whether a failure not directly placed under the sensor can be detected. The delamination in the area of soldering in any of the components accelerates solder joint fatigue; in the area of DPAK, delamination specifically accelerates the wire-bond lift-off. The third investigated failure mode was a solder crack that could happen due to fatigue, and this fault was located under the sensor (see Figure 7.1.2(c)). This failure was inserted in such a way that does not affect the electrical connections of the sensor. Table 7.1 summarizes the investigated failures and the reference names used later on in the chapter.

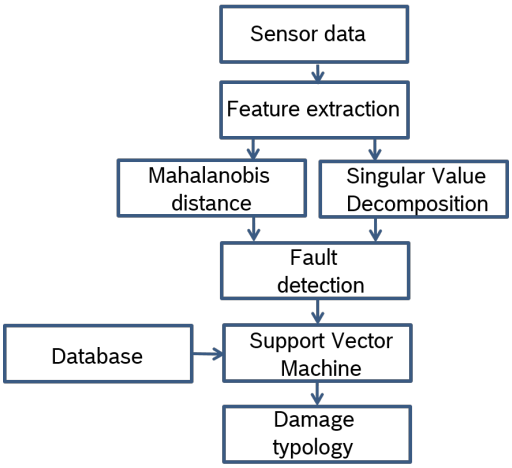

Figure 7.1.1: Proposed workflow for use of studied algorithms.

Collected data was then analyzed using statistical pattern recognition algorithms. Three different algorithms

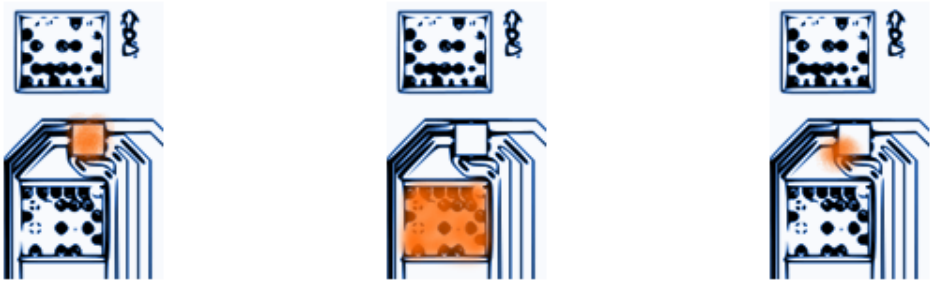

(a) (b) (c)

Figure 7.1.2: Locations of the inserted failure modes. (a) Delamination in the sensor area. (b) Delamination in the DPAK area. (c) Solder crack in sensor area.

were studied—MD [165] and SVD [69]-[70] for damage detection; and SVMs for damage typology [166]. The damage detection algorithms do not require a prior knowledge regarding failures; they only search for any deviations from the norm in the data. The SVM algorithm can classify the data containing different failure modes. However, it needs information on the typical signals concerning different failures. When an unknown failure occurs, it can be falsely classified as a healthy state. Hence, the proposed workflow of studied algorithms includes firstly one of the detection algorithms and then a classification algorithm as presented in Figure 7.1.1. Because this investigation focuses on detecting different damage types, the considerations regarding damage size are beyond the scope of this study.

Next, the developed approaches for failure detection were tested with measurement data in which the progression of delamination was observed. Both algorithms were adapted for the real time measurements with the actual variability present in the results. Additionally, an adaptive update of the healthy baseline was implemented. This allows for the classifying of the phenomena, such as the aging of the materials or the humidity intake, that introduces changes into the signal but do not represent failure, as a healthy behavior.

Table 7.1: Investigated failure modes

FM1	Delamination in the sensor area
FM2	Delamination in the DPAK area
FM3	Solder crack in sensor area

To apply the statistical pattern recognition techniques, the information on the variability of sensor responses is needed. For this purpose, the uncertainties from the experiment evaluated in Chapter 3 were used here. After an evaluation of the simulation results, it was found that the sample variability was too high to detect failure in a reliable way. Thus, only the variability related to the measurement process is taken into account in the process of creating the statistical distribution. This means that a database of healthy results was created as normal distribution with a standard deviation of 0.3 MPa for stress difference and 0.2 MPa for shear stress values.

7.2 Mahalanobis distance

MD is defined as a distance in a multidimensional space that considers correlations among parameters [167]. It is similar to Euclidean distance; the only difference is that it takes correlation coefficients of performance parameters into account. This is also a reason for the algorithm's sensitivity.

This approach needs both a healthy baseline and a threshold to classify a product to be healthy or unhealthy. Figure 7.2.1 presents an MD algorithm workflow. The methodology begins with gathering the sensor data, namely the values of stress difference and shear stress at location of the 24 sensor cells, as shown in Figure

7.2.2. These values are referred to as performance parameters. The typical performance parameters pattern for a molded sample in a healthy state is presented in Figure 7.2.3. For the sake of simplicity, they are presented as the half pattern (i.e., 12 points from a half of the chip); the other half is symmetrical. This is actually just another representation of the data depicted in Figure 4.5.7. Thus, it is an average pattern measured from 8 samples. It is worth noting that the general pattern is kept between the measurements at low and high temperatures. However, the pattern is expected to change due to structural change in the system.

The performance parameters are stored in a matrix X_{ij} with elements denoted as x_{ij} (see Figure 7.2.2), where $i = 1, 2, \ldots, p$ and p is the total number of performance parameters (here $p = 24$) and $j = 1, 2, \ldots, m$ where m is the total number of observations. The normalized values are calculated as follows [167]:

$$z_{ij} = \frac{x_{ij} - \bar{x_i}}{s_i} \tag{7.2.1}$$

Where:

$$\bar{x_i} = \frac{1}{m} \sum_{j=1}^{m} x_{ij} \tag{7.2.2}$$

$$s_i = \sqrt{\frac{\sum_{j=1}^{m} (x_{ij} - \bar{x_i})^2}{m - 1}} \tag{7.2.3}$$

The correlation matrix is calculated as:

$$C = \frac{1}{m-1} \sum_{j=1}^{m} Z_j Z_j^T \tag{7.2.4}$$

Finally, the MD for a healthy dataset is calculated as:

$$MD_j = \frac{1}{p} Z_j^T C^{-1} Z_j \tag{7.2.5}$$

After calculating the MD values for each observation from healthy baseline, it is necessary to establish a threshold which is used for making a decision between a healthy and a damaged state. For threshold determination, a probabilistic approach is used. Since the MD is not normally distributed, a Box-Cox transformation [167] is used. This transformation converts the variable, which contains only positive values and does not follow normal distribution into a normally distributed variable. It is defined as follows [168]:

$$x(\lambda) = \begin{cases} \frac{x^\lambda - 1}{\lambda} & \text{for } \lambda \neq 0 \\ ln(x) & \text{for } \lambda = 0 \end{cases} \tag{7.2.6}$$

Where:
$x(\lambda)$ - the transformed data
$x = x_1, x_2, ..., x_m$ - the input vector of data observation.

The parameter λ is calculated by maximizing the following function:

$$f(x, \lambda) = -\frac{m}{2} ln \left[\sum_{i=1}^{m} \frac{(x_i(\lambda) - \bar{x}(\lambda))^2}{m} \right] + (\lambda - 1) \sum_{i=1}^{m} ln(x_i) \tag{7.2.7}$$

Where:

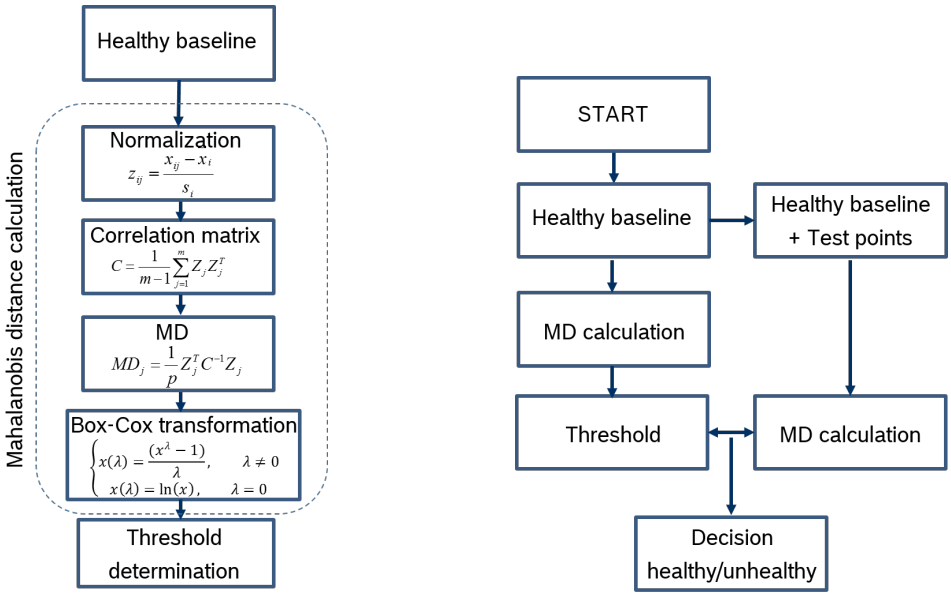

Figure 7.2.1: MD algorithm workflow. (a) Threshold determination workflow with detailed algorithm. (b) Complete algorithm workflow.

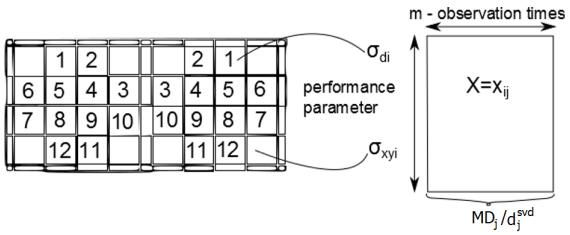

Figure 7.2.2: Input matrix construction.

$$\bar{x}(\lambda) = \frac{1}{n}\sum_{i=1}^{m} x_i(\lambda) \tag{7.2.8}$$

After applying this transformation, the determination of a threshold can be done based on mean (μ_x) and standard deviation (σ_x) of the resulting variable. Since higher MD values are the ones that indicate failure, only the upper part of the control chart is significant for this approach. A warning limit threshold is defined as ($\mu_x + 2\sigma_x$) and a fault alarm threshold as ($\mu_x + 3\sigma_x$). Then, for every point where the calculated MD value will be smaller than the fault alarm threshold, the point lies within 99.8 % of the points provided to the healthy database, and thus it is qualified as healthy. The points for which MD value crosses the fault alarm threshold is classified as an outlier (i.e., point containing failure). The MD value of 0 would mean that the tested measurement point corresponds exactly to the average point of the healthy database. The numerical values of MD are directly related to the standard deviation of the healthy database MDs.

The main advantage of this method is that it does not require knowledge of failure modes for training. That means the only thing needed to start the algorithm is a healthy baseline that can be created based on the initial measurements in the system. Additionally, the MD values are calculated using the normalized values of performance parameters, which eliminates the problem of scaling. Other advantages include a good accuracy and easy implementation.

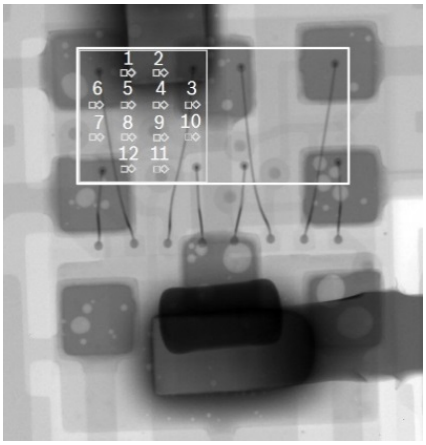

(a)

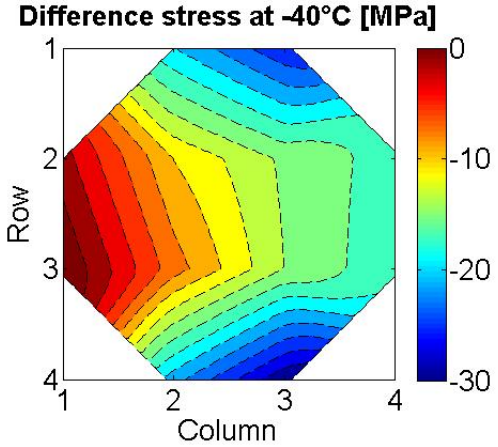

(b)

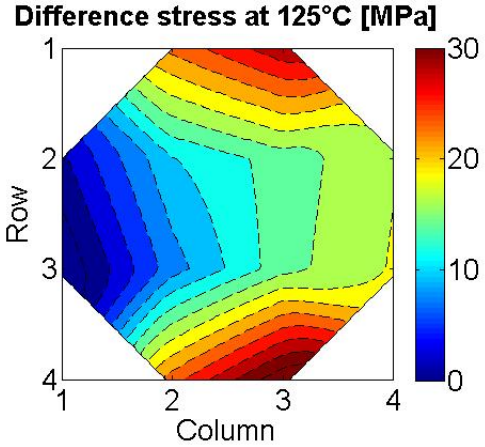

(c)

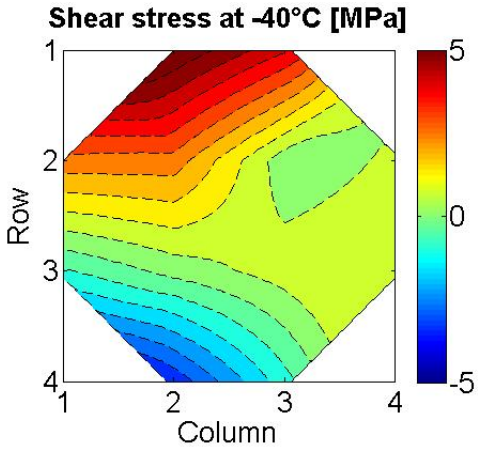

(d)

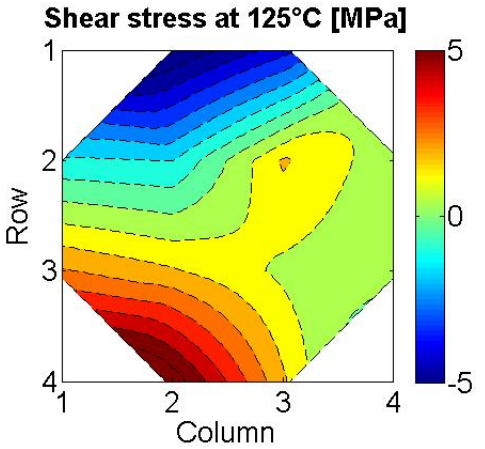

(e)

Figure 7.2.3: The performance parameters pattern. (a) Difference stress at -40°C. (b) Difference stress at 125°C. (c) Shear stress at -40°C. (d) Shear stress at 125°C.

7.2.1 Results based on simulation

A result of fault classification conducted with an MD approach is presented in Figure 7.2.4. The first hundred points are from the healthy baseline, and the last data point contains damage. This point is clearly detected, and it is seen to cross the fault alarm threshold. However, some of the points from healthy baseline do cross the warning level. It is caused by the threshold definition—around 98% of the points should lay within the $(\mu_x + 2\sigma_x)$ bound. To deal with this feature in real time measurements, a couple of consecutive points should be classified as potentially containing failure so that the actual warning can be given.

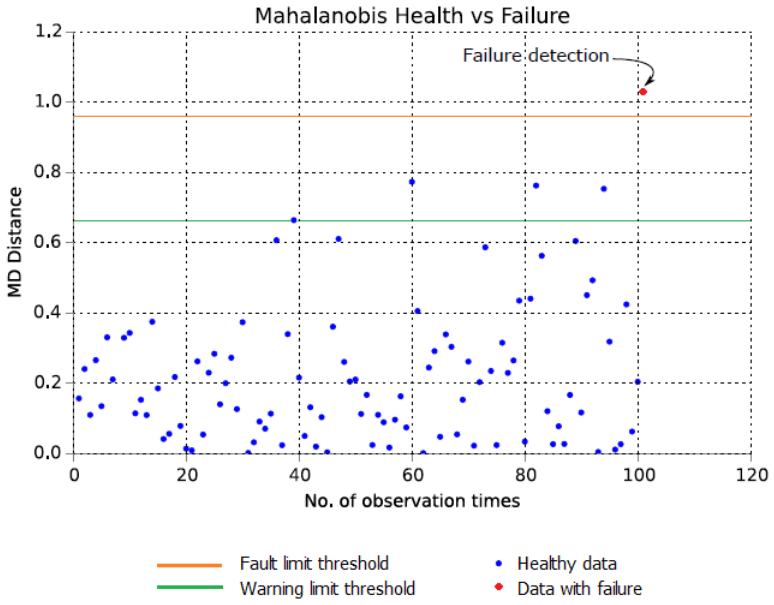

Figure 7.2.4: Results of MD algorithm.

The detection results for all failure modes using both stress difference and shear stress data are presented in Table 7.2. It shows that this method works very well in detecting failure for different damage types. The only case here where the results are not always conclusive is that of damage recognition based on shear stress values.

Table 7.2: Damage detection by MD algorithm for different failure modes and stress components

Condition	-40 °C		125 °C		active	
Failure mode	σ_d	σ_{xy}	σ_d	σ_{xy}	σ_d	σ_{xy}
FM1	✓	✓	✓	✓	✓	✓
FM2	✓	×	✓	×	✓	×
FM3	✓	✓	✓	✓	✓	✓

In conclusion, it can be stated that this method can easily be used for damage detection, although for a robust algorithm it must be further improved.

7.2.2 Results based on measurements

Next, the developed approach was applied to the data gathered from experiment. In order to obtain the signal containing failure, a set of pre-delaminated samples was produced. The samples were subjected to temperature cycling between -40°C and 125°C and examined using a SAM for every 150 cycles. Figure 7.2.5

presents a propagation of delamination that was observed. In this particular case, the delamination occurred just under the sensor on the other side of PCB, on the interface between outer molding compound and the PCB. Figure 7.2.6 shows an example of a stress measured during the propagation of delamination. For the sake of simplicity, a signal from only one of the measurement cells is presented. The data points are extracted separately at temperatures of 125°C and -40°C in order to evaluate the stress evolution independent of the thermo-mechanical behavior of the system. The delamination progression was observed in the measurement data for about 10 temperature cycles, starting at cycle number 30. The stresses in different measurement cells change with different trends, and this situation causes the pattern of stress distribution over silicon chip to change.

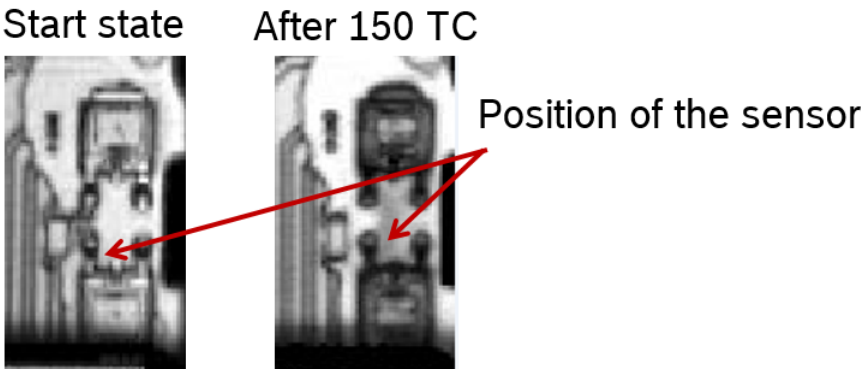

Figure 7.2.5: The images of a sample region where delamination progression was observed from a SAM.

Figure 7.2.7 shows similar data except this one is from a healthy system with no observed failure. In these data, changes in the signal were also observed. They are caused by various effects, such as material aging, material setting, or moisture intake/uptake. However, the observed changes had a much smaller magnitude and did not cause a rapid changes in the signal. The major challenge of applying the pattern recognition techniques to the measurement data is to be able to distinguish between the healthy changes and the changes caused by a failure.

To take the healthy changes of a signal into account, the algorithm was modified—specifically, an adaptive update of a healthy baseline was introduced. The modified workflow is presented in Figure 7.2.8. In this approach, every point is tested using an existing healthy baseline. When a data point is classified as healthy, the baseline is then updated; its oldest point is replaced with the new one. This also necessitates a recalculation of the threshold, which is then adapted to the existing healthy baseline.

The results of the MD approach applied to healthy data are presented in Figure 7.2.9. As observed in Figure 7.2.9(a), the algorithm with a constant healthy baseline provided false warning results after around

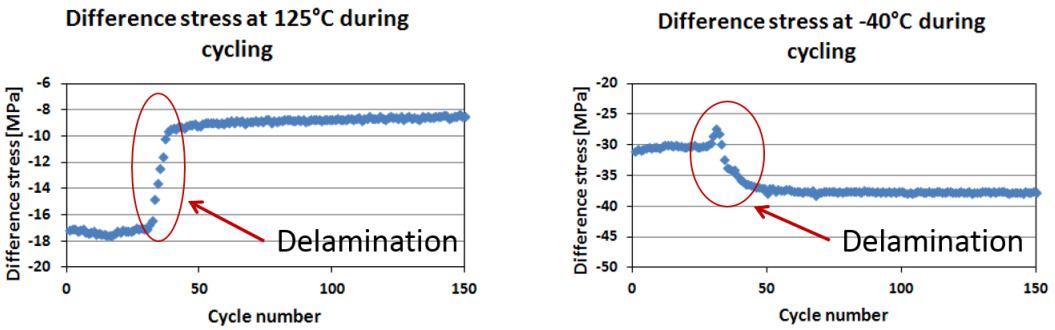

(a) (b)

Figure 7.2.6: Measured difference stress during temperature cycling when the delamination progression was observed. Values extracted (a) at 125°C and (b) at -40°C.

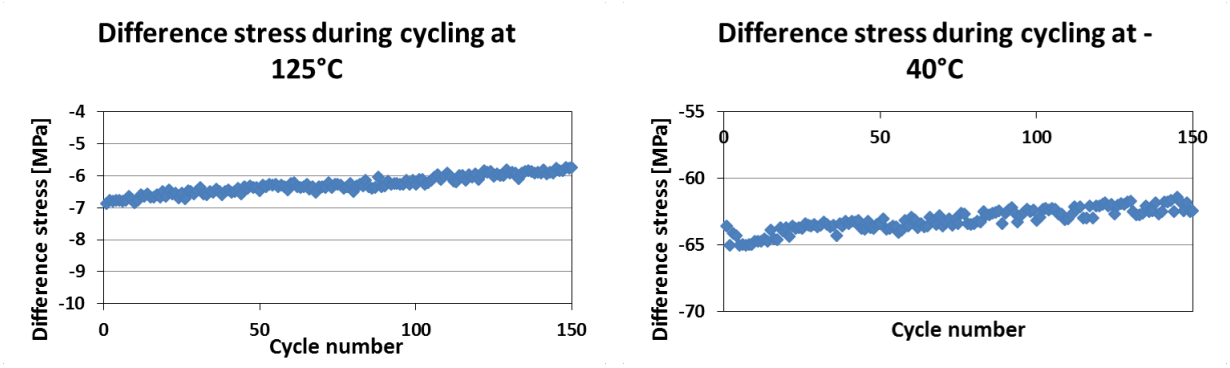

(a) (b)

Figure 7.2.7: Measured difference stress during temperature cycling when no failure was observed. Values extracted (a) at 125°C and (b) at -40°C.

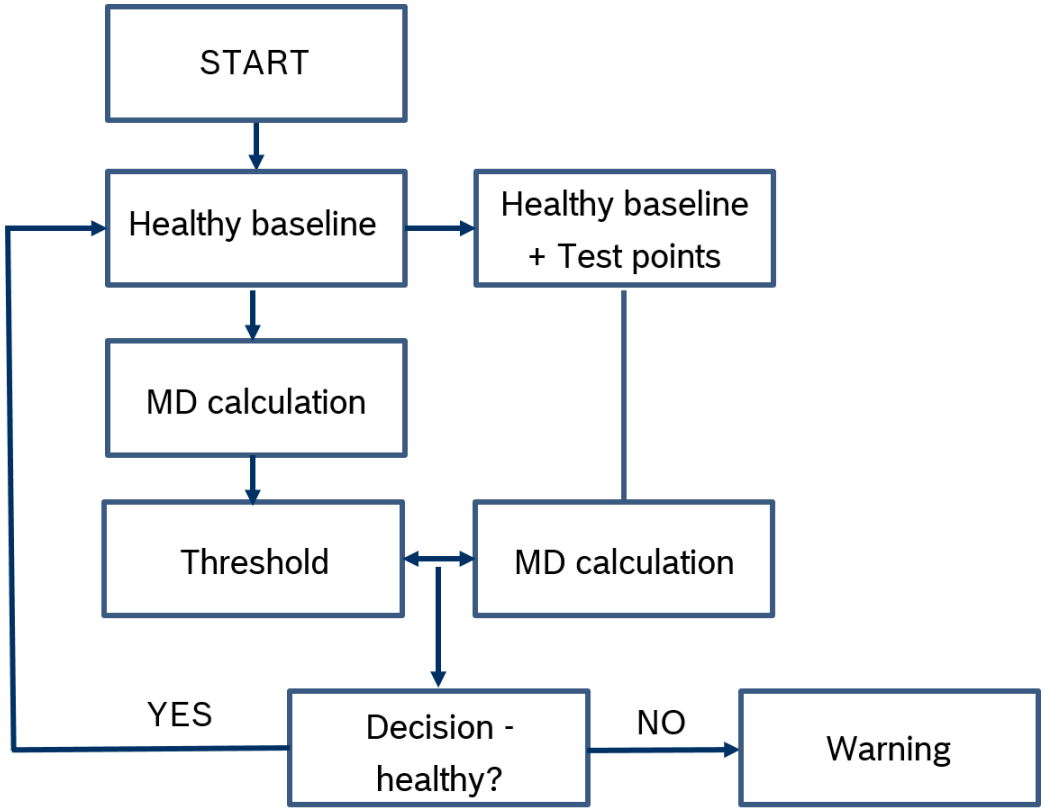

Figure 7.2.8: Workflow of implementation of MD with adaptive update of the healthy database.

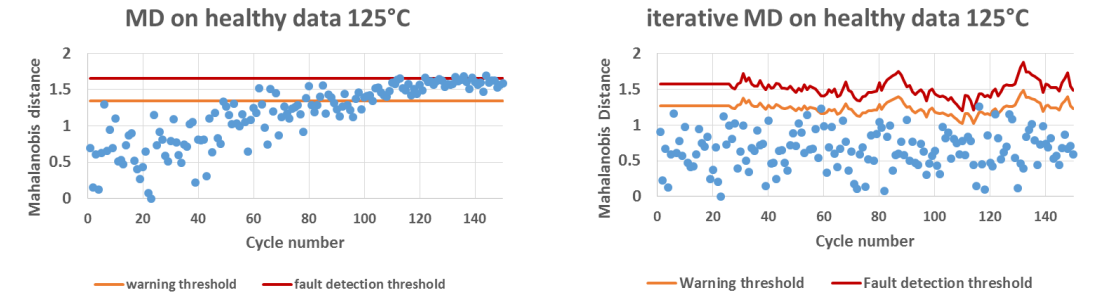

(a) (b)

Figure 7.2.9: The results of MD algorithm applied on healthy data from measurement. (a) Algorithm with constant healthy baseline. b) Algorithm with adaptive healthy baseline update.

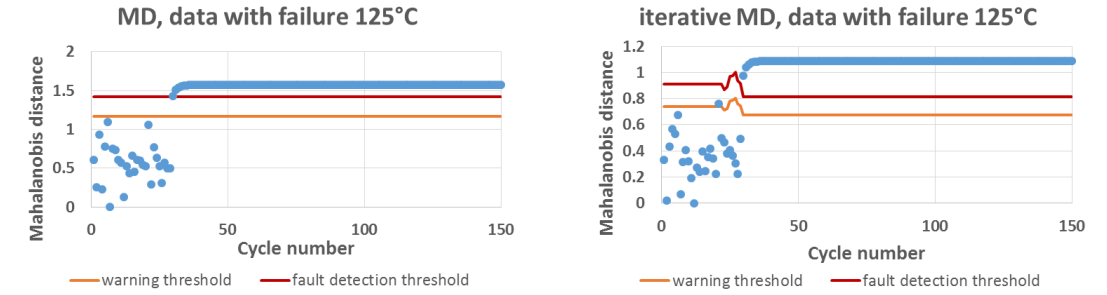

(a) (b)

Figure 7.2.10: The results of MD algorithm applied on measurement data with failure. (a) Algorithm with constant healthy baseline. (b) Algorithm with adaptive healthy baseline update.

60 measurement points and a false fault alarm after around 120 points. A clear growing trend can be observed in the data. This behavior was eliminated by updating the healthy baseline in every step as shown in Figure 7.2.9(b). In this case, the MD values do not show any clear trend and are distributed randomly. This eliminates the concern about false failure detection due to normal changes of sensor response. The warning threshold was exceeded only by a few points, which occurred for the statistical reasons that were discussed in previous sections. It is worth noting that the threshold changes also with every update of the healthy baseline. However, there are no observable trends in the thresholds behavior.

In Figure 7.2.10, the analogical results are shown for the data containing failure. In both cases, the failure is clearly detected starting with the 30^{th} point in the data set. The algorithm was tested with all available data containing failure, and failure was detected in all of the cases.

7.3 Singular Value Decomposition

SVD is a discrete version of the algorithm known as POD, and it is a multi-variate statistical method for data analysis. In this work it is used for feature extraction from the data by revealing its structure. The main idea here is to decompose the matrix into a product:

$$X_{ij} = U_{orth} S V_{orth}^{T} \tag{7.3.1}$$

Where:
U_{orth} and V_{orth} - two orthonormal matrices,
S - matrix containing the singular values σ_S of the matrix X_{ij}.

When the matrix X_{ij} contains data with damage, the decomposition deviates from the one calculated only with data from intact structures. Figure 7.3.1 shows an example illustrating the effect of data containing a failure of the singular values.

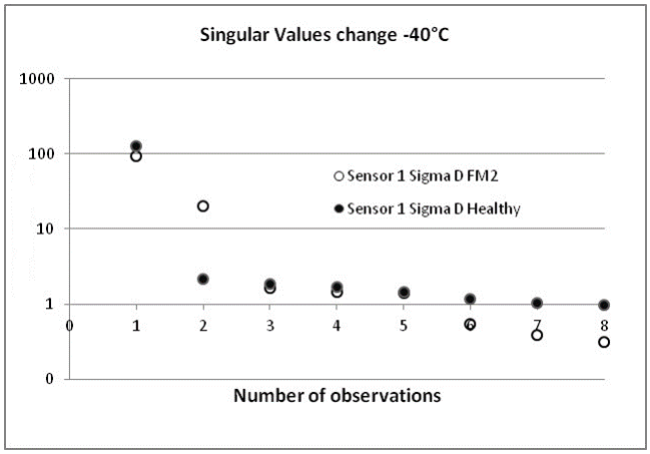

Figure 7.3.1: The effect of data containing a failure of the singular values of a matrix.

The classical LS-SVD algorithm workflow used in this work is presented in Figure 7.3.2 [68]. The first step is to create a performance parameter space. Matrix X_{ij} is built in the same way as for MD approach—that is, the values of stress difference and shear stress at the 24 sensor cells locations are the performance parameters, stored in a matrix X_{ij} with elements denoted as x_{ij}, where $i = 1, 2, \ldots, p$ and p is the total number of performance parameters (here $p = 24$) and $j = 1, 2, \ldots, m$ where m is the total number of observations [68]. A condition that has to be fulfilled in order to detect a failure using this method is that the number of observations containing damage must be greater or equal to the number of healthy observations. In this case, a matrix with eight columns is created, with the four first columns containing healthy data and the rest of the data with damage. Next, the matrix is decomposed according to (7.3.1). All the singular values below the arbitrary chosen noise level are then set to a value of 0, and the matrix X_1 is resynthesized. Afterwards, the residual matrix E_1, the standard deviation of residuals, and the standard deviation of every observation are computed. Finally, the relative distance d_j is obtained which follows χ^2 distribution with a mean of $m = 1$. The threshold for fault qualification is determined based on standard deviation σ of this distribution with a confidence level 95%. Using this procedure, an automatic classification between damaged and healthy observations can be made.

The problem with the classical LS-SVD technique is that it is very sensitive to outliers [68]. To reduce any effects from outliers, an iterative SVD can be used. In this approach, the classical LS-SVD algorithm is firstly applied. Then, the observations with outlying distance $\mathrm{d_j}$ are eliminated, and the SVD of the remaining observations is calculated again. The workflow of iterative SVD is presented in Figure 7.3.3.

Another approach that can be used to improve the performance of SVD algorithm is robust SVD introduced in [68]. Figure 7.3.4 presents the workflow of a robust SVD algorithm. The algorithm starts with drawing a random subset of half of the observations from the input matrix X_{ij} and computing SVD of the obtained matrix X_l. This is done for every possible combination of columns, which means $l = {}^{m!}/_{((m/2)!)^2}$ times. Next, the right singular matrix $V_{l'}$ is extended to all the columns in the original input matrix, and the new matrix $X_{l'}$ is resynthesized. Residuals E_l as well as relative distances d_j are then calculated. Following this, a cost function is calculated as the RMS of half of the smallest distances, according to the formula:

$$\kappa = \sum_{k=1}^{m/2} |d_k|^2 \tag{7.3.2}$$

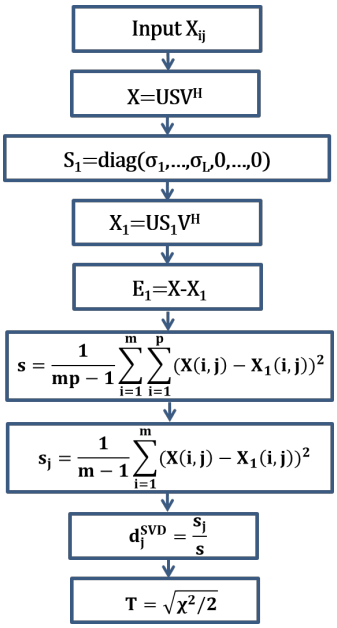

Figure 7.3.2: Classical SVD algorithm workflow [68].

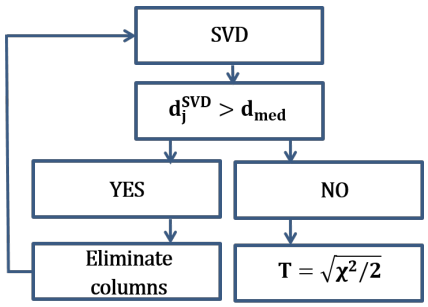

Figure 7.3.3: Iterative SVD algorithm workflow [68].

As the final solution of robust SVD, the result of the combination with the smallest cost function is chosen. This method is computationally more expensive, but it provides much more reliable results.

The main advantage of an SVD approach is its short calculation time. As shown in Table 7.3 both classic and iterative SVD have very short calculation time. Robust SVD is computationally more expensive but it also produces more reliable results. Its calculation time strongly depends on the number of observations taken into account, as all the combinations of columns must be considered. Similar to the MD method, it does not require prior knowledge on the failure modes, and it works on normalized data. The main disadvantage here is that it requires multiple observations containing failure to be firstly made before damage detection can occur.

7.3.1 Results based on simulation

Figure 7.3.5 shows an example of the output of a classical LS-SVD; iterative SVD and robust SVD are presented in Figures 7.3.6 and 7.3.7 respectively. All of the SVD calculations were made with matrix containing eight observations; among them four were healthy and four contained failure.

In the case of classical LS-SVD, there is no significant difference between the results for shear stress and stress difference. In both of these cases, the threshold is at a level of around 1.0. The distances calculated for healthy points have values close to 0, and for data containing failure the values were between 1.0 and 3.0.

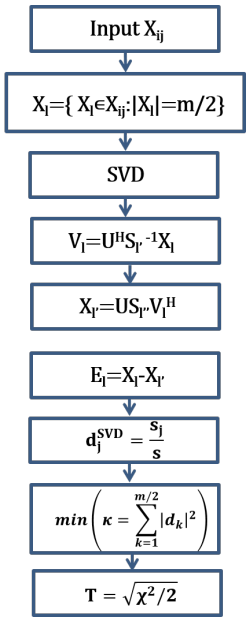

Figure 7.3.4: Robust SVD algorithm workflow [68].

In the case of iterative SVD, the distances calculated for unhealthy points are much larger for shear stress data than difference stress. The threshold is in both cases at approximately the same value of around 2.0. It is yet different for a robust SVD results, where the distances for difference stress are much larger than those for shear stress. This shows that there is no obvious choice of a measured parameter that should be chosen for the analysis. To make the detection more reliable, it may be even needed to analyze both signals. It is also worth noting that the robust and iterative SVD provide a much sharper separation of the healthy and damaged observations.

These methods were tested on data concerning all three failure modes, and in all cases the damage was detected.

7.3.2 Results based on measurement

The SVD algorithms were tested on the same experimental data sets containing failure as MD. Similar to the case of MD algorithm, an adaptive healthy baseline update was implemented for SVD. Figure 7.3.8 presents the results of robust SVD with a constant healthy baseline, and Figure 7.3.9 presents robust SVD results with an adaptive healthy baseline. It can be observed that in both cases the failure is first detected at the 33^{rd} observation point. The delay is caused by the fact that the SVD method detects failure only when the input matrix contains at least the same number of observation points with failure as the number of healthy ones. The use of an adaptive healthy baseline update does not affect the point of failure detection. However, it improves the behavior of the algorithm in the case of a healthy data analysis. In the case of the constant healthy baseline, a steady growth in a calculated relative distance is observed throughout the healthy data as shown in Figure 7.3.8(a). The false positive result of failure detection happens at around the 30^{th} data point. This behavior is eliminated by the adaptive healthy baseline update. As presented in Figure 7.3.9(a), the calculated relative distances do not show any trend in time, and all data points are correctly classified as healthy.

All three versions of SVD algorithm were tested using measurement data. The results of classical LS-SVD are presented in Figure 7.3.10, while iterative SVD and robust SVD are seen in Figures 7.3.11 and 7.3.9 respectively. Among those three approaches, only robust SVD was able to detect failure in a reliable way. A

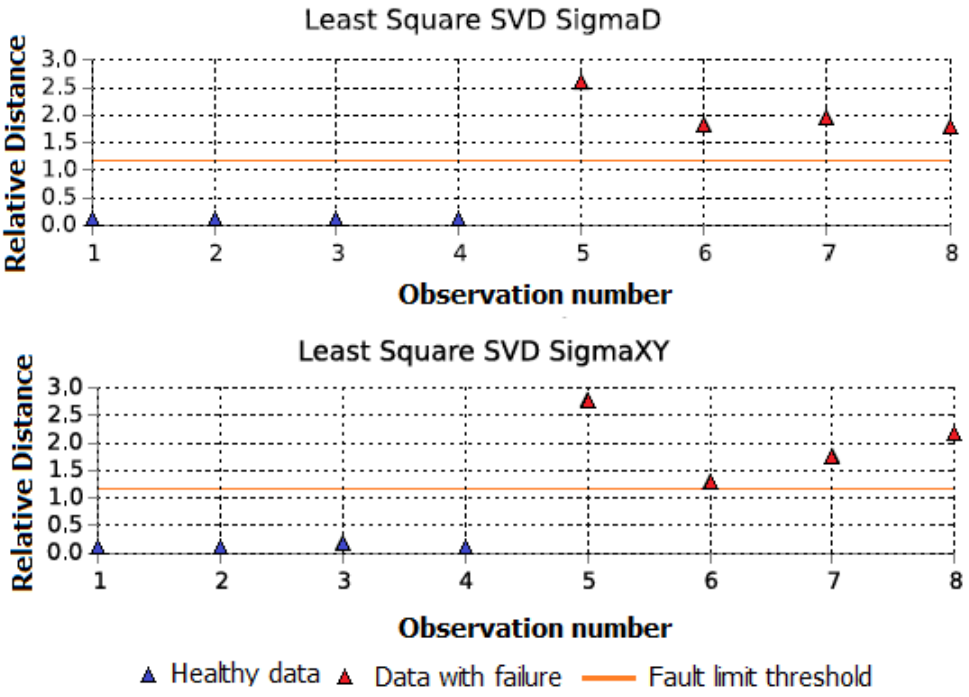

Figure 7.3.5: Example of the LS-SVD results.

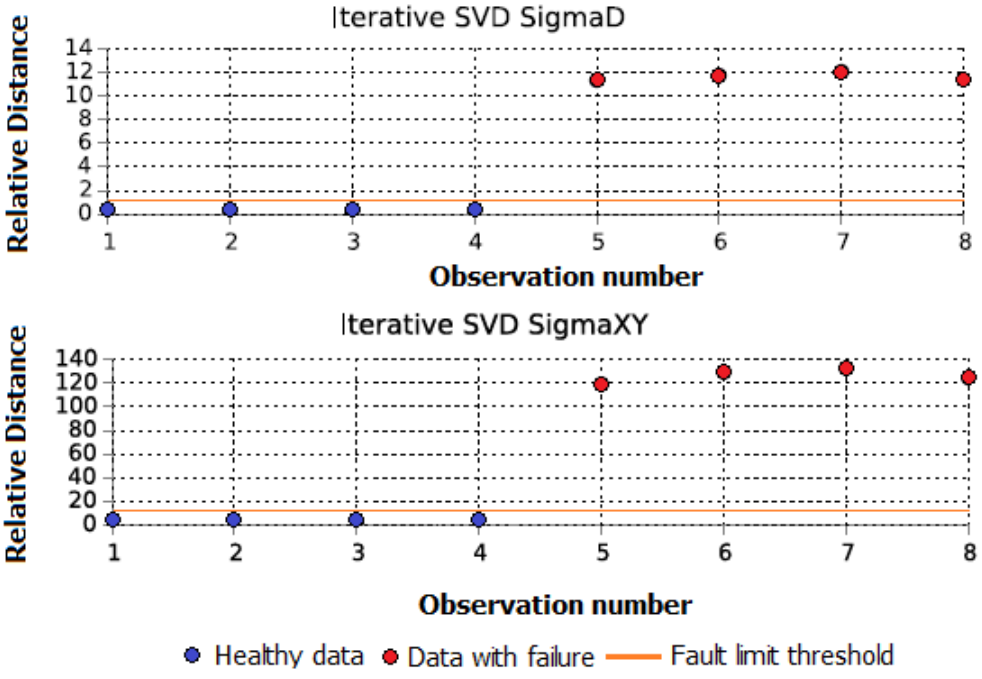

Figure 7.3.6: Example of the iterative SVD results.

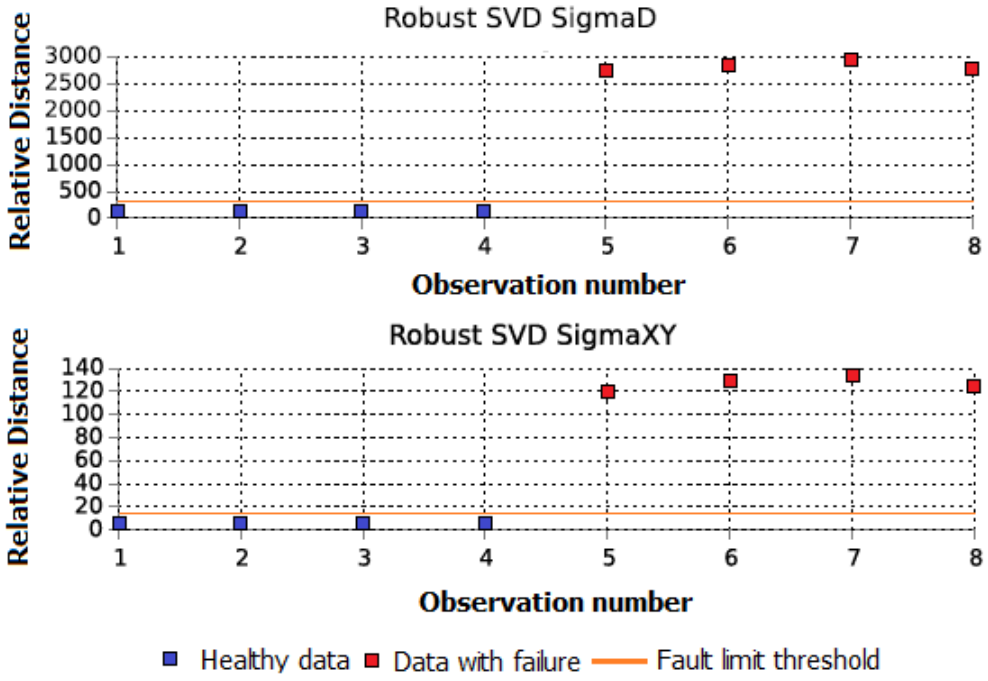

Figure 7.3.7: Example of the robust SVD results.

slight change of the calculated relative distance can be seen in the LS-SVD results where the failure occurs as depicted in Figure 7.3.10(b). However, the sensitivity of the method is not sufficient to detect the failure.

Also, in the case of the iterative algorithm, the apparent change of values of relative distance is caused by an analysis of data containing failure. Nevertheless, the results become highly unstable, and this is caused by the fact that in this algorithm the outliers are removed in a course of calculation. Hence, the algorithm which tries to detect this type of failure in some of the cases removes the observations containing failure from the input matrix.

The most satisfying results are obtained using a robust SVD algorithm. The failure is detected at the first possible point in time. However, this is the most computationally expensive version of SVD to use, and the calculation time is comparable to MD.

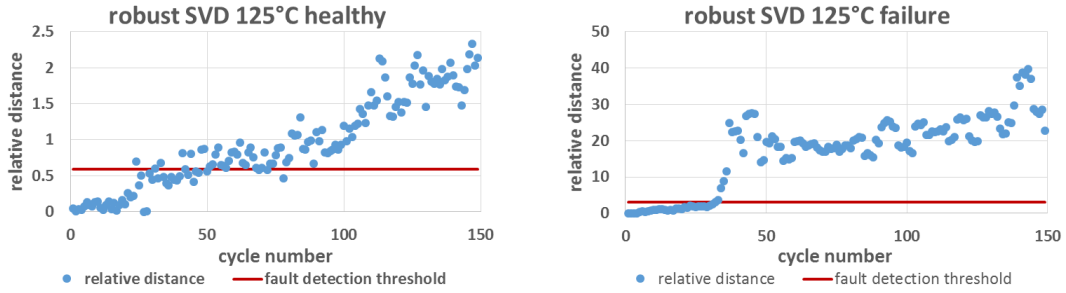

(a) (b)

Figure 7.3.8: The results of robust algorithm with constant healthy baseline applied (a) on healthy data from measurement and (b) on data with failure.

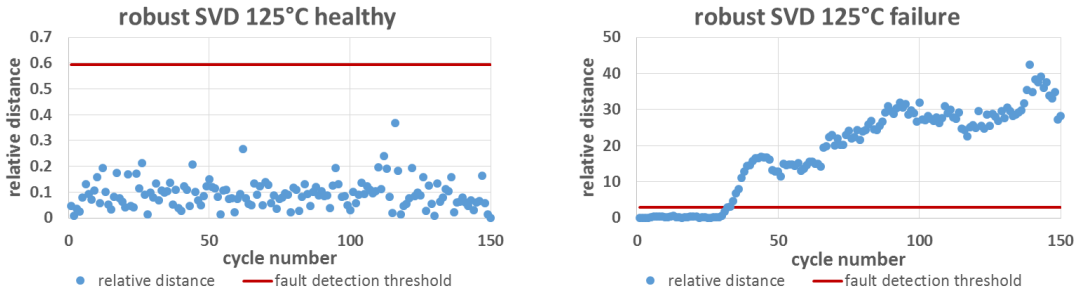

(a) (b)

Figure 7.3.9: The results of robust SVD algorithm with adaptive healthy baseline update applied (a) on healthy data from measurement and (b) on data with failure.

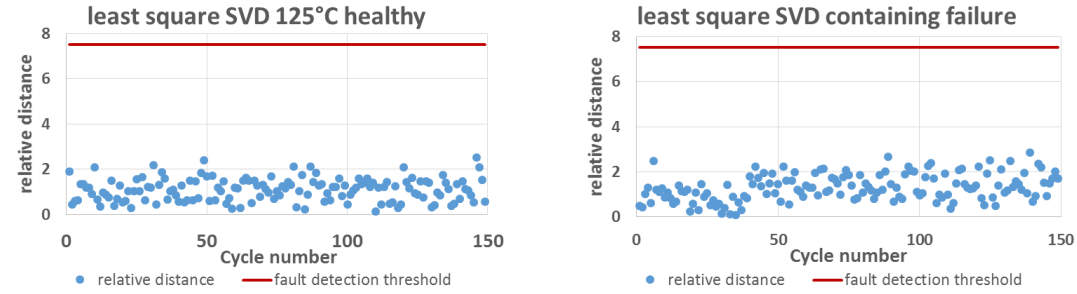

(a) (b)

Figure 7.3.10: : Results of an LS-SVD algorithm with adaptive healthy baseline update applied (a) on healthy data from measurement and (b) on data with failure.

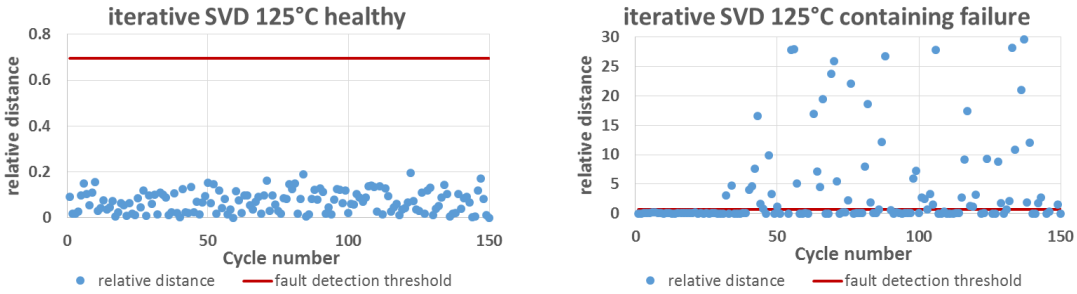

(a) (b)

Figure 7.3.11: Results of an iterative SVD algorithm with adaptive healthy baseline update applied (a) on healthy data from measurement and (b) on data with failure.

7.4 Comparison of data detection algorithms

The MD and SVD algorithms are both used for damage detection, and their performances have been evaluated and compared. Table 7.4 summarizes the advantages and disadvantages of both presented methods. Both algorithms work on normalized data and do not require prior knowledge on failures. The calculation time of MD is much longer as the calculations are made using relatively big matrices. For the MD approach, it is recommended that the healthy baseline is large so that failure can be detected in a reliable manner. In the case of SVD, the healthy baseline should be limited. The first reason for this is that failure detection can be made only when there are as many healthy as unhealthy observations. Additionally, too many points in the healthy baseline can cause SVD algorithm to be somehow too strict, which then could give false positive outcomes. Handling of much smaller data sets causes the SVD algorithm to have a much shorter calculation time. However, the robust SVD algorithm has a comparable calculation time to MD, as the matrix decomposition must be calculated multiple times. This is also the only version of the algorithm that detects a failure in a reliable way. Thus, the MD method is somehow more suitable for damage detection as it can detect the damage earlier and has a comparable calculation time.

Table 7.3: Calculation time of used algorithms

Algorithm	Calculation time [s]
Mahalanobis Distance	0.11
Classic SVD	0.05
Iterative SVD	0.08
Robust SVD	0.10

Table 7.4: Advantages and disadvantages of tested damage detection algorithms

Mahalanobis Distance	**SVD**
Advantages	
Works on normalized data	Works on normalized data
	Short calculation time
Does not require prior knowledge about failures	Does not require prior knowledge about failures
Good accuracy	
Easy to implement	
Disadvantages	
Relatively long calculation time	
Inconclusive for shear stress results	Sensitive to noise
False warning result	Requires more than one data point for data with failure

7.5 Support Vector Machine

SVM is a machine learning algorithm that can solve classification problems. Its main advantage is that it can form accurate boundaries between datasets even with a small amount of training data [81]. Additionally, it can often provide a good generalization and can find a single global minimum for a problem.

The main idea behind using an SVM is to find the plane separating the given datasets in such a way that the distance between them is maximized. For n—dimensional sets of data, an $n-1$—dimensional hyperplane that separates them is searched. This hyperplane can be a linear or non-linear boundary.

To explain the SVM algorithm, an example of two dimensional linear problem is presented (see Figure 7.5.1). First, the training data are labeled, thus creating separate sets. For each point, x_i from the first data set the value $y_i = -1$ is assigned as a label; for points x_i from the other set, the value $y_i = 1$ is assigned. The classification in this case is performed by considering plane $H1$ to consist of the points that satisfy the equation $wx + b = 0$, where w is normal to the plane and b is the perpendicular distance from the plane to the origin, normalized by length of w. The following conditions should be satisfied for all training data points:

$$x_i \cdot w + b \geq 1 \quad \text{for} \quad y_i = 1 \tag{7.5.1}$$

$$x_i \cdot w + b \leq -1 \quad \text{for} \quad y_i = -1 \tag{7.5.2}$$

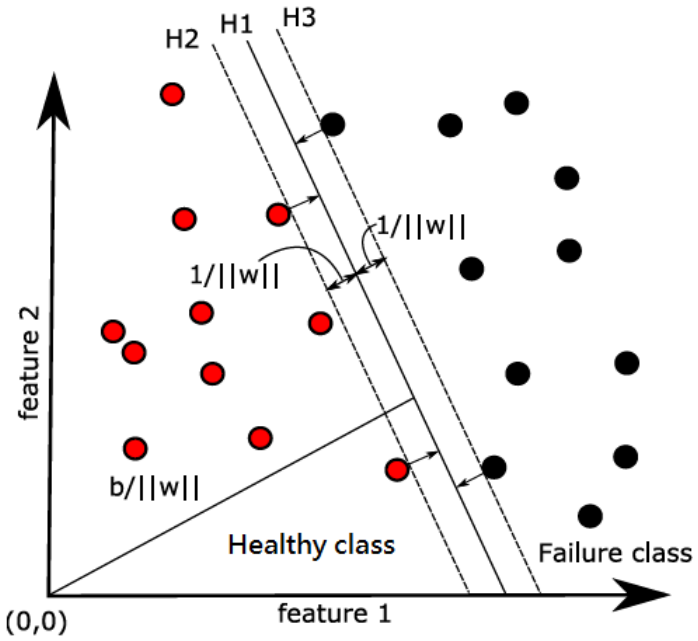

Figure 7.5.1: Linear SVM problem.

The points for which (7.5.1) is satisfied are found on the hyperplane $H2$, and the points for which (7.5.2) is satisfied are found on the hyperplane $H3$. Hence, the distance between $H1$ and $H2$ is $d_+ = 1/||w||$, the distance between $H1$ and $H3$ is $d_- = 1/||w||$, and the margin is simply $2/||w||$. Considering that H2 and H3 are parallel and no points lie between them, the optimization problem needs to minimize $||w||^2$, which is subjected to the constraint:

$$y_i(x_i w + b) - 1 \geq 0 \tag{7.5.3}$$

(7.5.3) simply combines (7.5.1) and (7.5.2) into one set of inequalities. The optimization problem is then solved by changing the constraints into Lagrangian multipliers. The objective function can be written as [81]:

$$L_p = \frac{1}{2}||w^2|| - \sum_{i=1}^{m} \alpha_i y_i (x_i w + b) + \sum_{i=1}^{m} \alpha_i \tag{7.5.4}$$

where α_i are positive Lagrangian multipliers.

The aim is to minimize Lp with respect to w and b.

The non-linear classification involves mapping the data points from a lower dimensional feature space into a higher dimensional space. This can be made by a function, which is called a kernel function. There are several functions used in the literature, but the one used in this study is the Gaussian radial basis function (RBF):

$$K(x_i, x_j) = exp(-\frac{||x - y||^2}{2\sigma^2}) \tag{7.5.5}$$

After mapping the points, the same linear separation procedure is applied, and the calculations are just executed in a different space.

For the given problem, different approaches to define performance parameters set were tested. The one that was able to separate the datasets containing different failures was when the SVM method was applied to each sensor cell separately—that is, the training data contained healthy and unhealthy values of stress difference and shear stress, measured at one location on the silicon chip. The results are depicted on 12 separate graphs concerning cells on the left side of the chip, as shown in Figure 7.5.2. The right side of the sensor behaves symmetrically, and it is not shown here for the sake of simplicity. Each graph depicts a rectangular space divided into subspaces marked with a different background color. They represent the areas separated by the boundaries between datasets calculated by the algorithm. Additionally, points representing the training data are placed on each graph. In general, the data sets containing different failures are well separated. It is worth noting that the performance of the algorithm depends on the position on the chip of the measurement. The datasets are separated the best in Cells 3 and 10 which are located inside the chip, and the worst are found in Cells 1 and 6 on the edge of the chip. Also, in some cells the points indicating FM2 are not perfectly separated from the healthy data. However, if one of the previous methods has already identified the point as one that contains failure, it is possible to easily avoid having the wrong qualification given by SVM. That is another reason why this method is proposed only for damage typology, not for damage detection.

This result shows that the SVM algorithm can classify the damage using SVM algorithm based on the measurement from the piezoresistive stress sensor. However, the typical signals corresponding to different failures occurring in the system must be provided as an input to the algorithm. This signal will likely have different characteristics depending on various criteria used, such as the type of the ECU, different material used, the position of the sensor, or the size of the sensor. Hence, providing a complete database for the algorithm is complex; in practice, the input data would have to be supplied based on the field measurements. Therefore, it is indispensable to use a damage detection algorithm before using the damage classification algorithm.

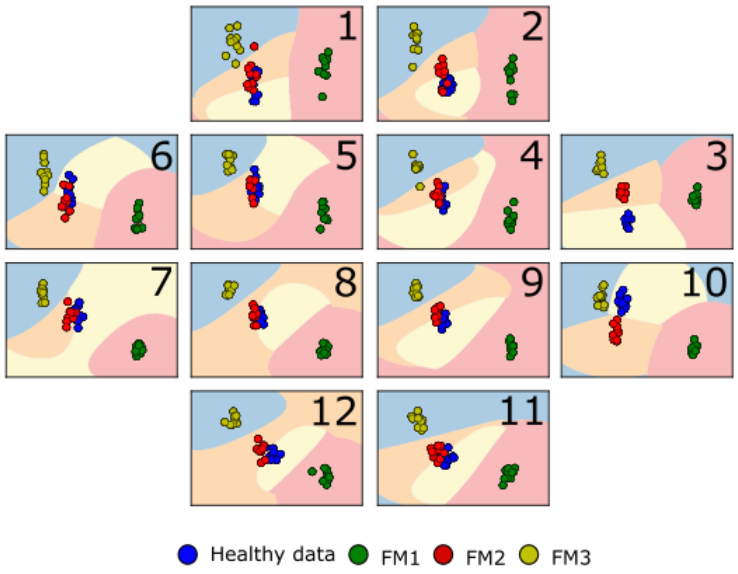

Figure 7.5.2: Results of SVM algorithm with RBF kernel function calculated separately for every cell.

7.6 Summary

This chapter explored damage detection using the piezoresistive silicon stress sensor. First, the stress states in the sensor subjected to different damage types was collected using validated FEM simulations. Then, three statistical pattern recognition algorithms were investigated with the data—namely MD and SVD for damage detection and SVM for damage typology. Both damage detection algorithms have successfully distinguished the differences between healthy and damage containing data, even for the case where failure was not inserted directly under the sensor. The advantages and disadvantages of both algorithms were evaluated. The SVM was applied to classify the failures. Additionally, the damage detection algorithms were tested with the available data containing damage progression.

For future studies, it is recommended to conduct a broader study to evaluate the minimum size of failure that can be detected by the sensor. Additionally, more of the actual damage data from the test vehicles should be collected to evaluate the performance of the proposed approach.

Chapter 8

Fusion approach

8.1 Proposed methodology

The two presented approaches for PHM using a piezoresistive stress sensor can be combined in order to improve their performances. The proposed workflow of such a fusion approach is presented in Figure 8.1.1. The methodology requires an in-situ monitoring of the investigated system using a piezoresistive stress sensor. The measured signal can be used to implement both physics-of-failure and data-driven approaches. The periodically measured temperature and stress values can be used as inputs to the reduced FEM model. The FEM model should be simplified by a model order reduction technique in order to enable in-situ evaluation of damage parameters, such as PSED or CSED. Then, using the established physics-of-failure model, it is possible to execute periodical calculation of RUL. In the same time, the pattern recognition algorithms can observe the stress signal in search for delamination signature. When it is detected, the reduced model for calculation of damage parameters can be updated. This leads to more accurate failure prediction under changing load conditions.

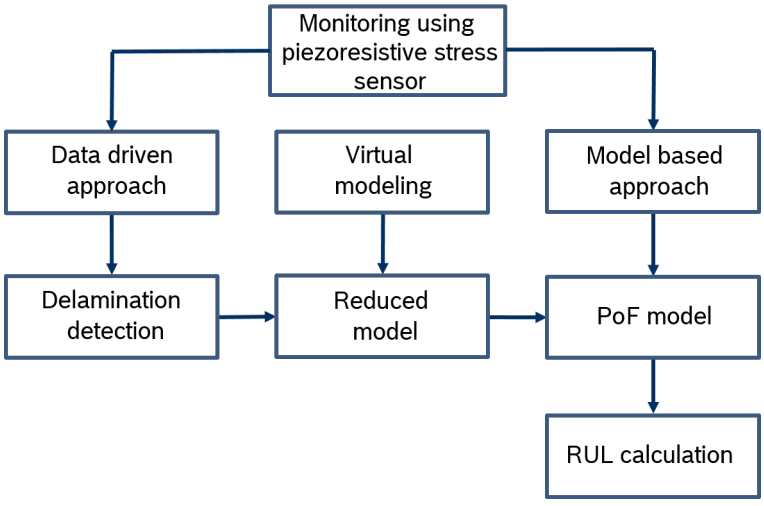

Figure 8.1.1: Workflow of proposed fusion approach.

8.2 RUL calculation

When the delamination occurs, the load in the design element changes rapidly. Because of this, an iterative approach was chosen for RUL calculation. The non-iterative approach takes an average of the load history

as a reference for RUL calculation, thus it is not suitable for cases where the load permanently increases. The iterative method for RUL calculation is based on the following equation [17]:

$$RUL_N = RUL_{N-1} - D_N \cdot PTL \tag{8.2.1}$$

Where:
RUL_{N-1} - remaining useful life calculated at the end of N-1 period
D_N - damage ratio accumulated over the Nth cycle/day/hour
PTL - predicted total life

However, in this approach the predicted total life is calculated only at the beginning. In the case where the delamination causes a permanent change in the load, the predicted total life should be updated as delamination appears so that a more accurate RUL prediction can be obtained. Hence, when the delamination occurs, a damage accumulated until the date should be calculated first. To do this, it is assumed that the delamination was detected at the $(n+1)$ cycle. The RUL at the end of n-th cycle can be expressed as:

$$RUL_n = PTL_1(1 - D_n) \tag{8.2.2}$$

Where:
D_n - damage ratio accumulated until the nth cycle
PTL_1 - predicted total life at the load level without delamination

Then, the damage accumulated until n-th cycle can be calculated as:

$$D_n = 1 - \frac{PTL_1}{RUL_n} \tag{8.2.3}$$

Similar equation as (8.2.2) can be formulated for the load level after delamination PTL_2:

$$RUL_n = PTL_2(1 - D_n) \tag{8.2.4}$$

Combining (8.2.3) and (8.2.4), we obtain:

$$RUL_n = PTL_2 \frac{RUL_n}{PTL_1} \tag{8.2.5}$$

This value can be further used in (8.2.1) as the RUL after first load cycle with delamination is calculated. Additionally, values of the predicted total life as well as of damage accumulated per cycle should be updated.

A result of a RUL calculation with an iterative method and updated predicted total life is shown in Figure 8.2.1. In this study, the damage parameters which were used for the calculation of RUL when the delamination occurred was evaluated using FEM simulation. Two different cases were calculated. For wire bond failure, the delamination between the copper lead frame and the DPAK mold in the area of a wire bond heel was modeled. For solder joints, the delamination was modeled between the solder and outer mold. Both of these cases maximize the delamination impact on the load in the investigated design elements.

According to the established failure model, the reliability of both wire bond and solder joint should decrease significantly when delamination occurs Figure 8.2.1. In the case of solder joint fatigue, when the delamination occurred, the RUL decreased from about 7500 thermal cycles to 700. In the case of a wire bond, delamination decreased from about 3000 thermal cycles to 600. It shows how critical it is to consider structural damage such as delamination while evaluating the RUL of an electronic system.

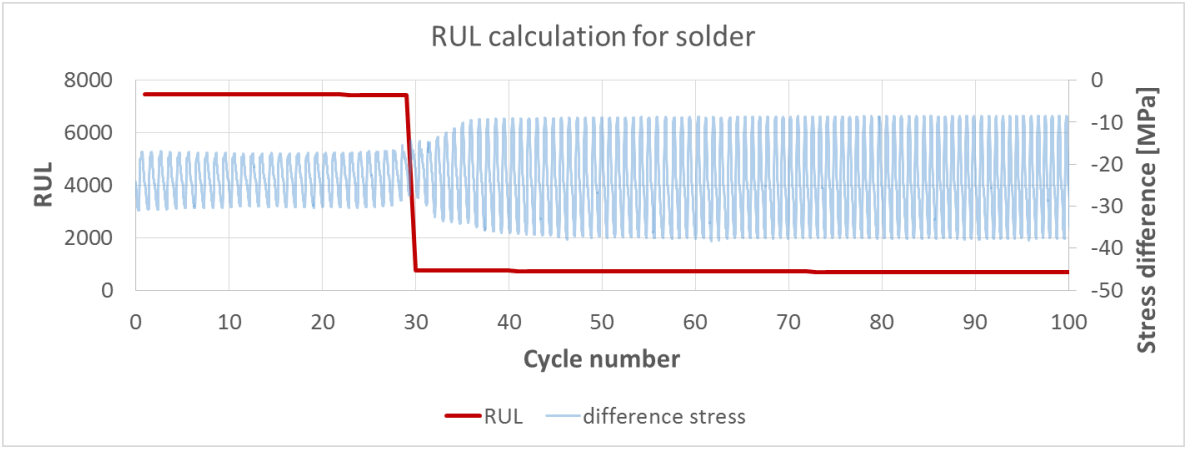

(a)

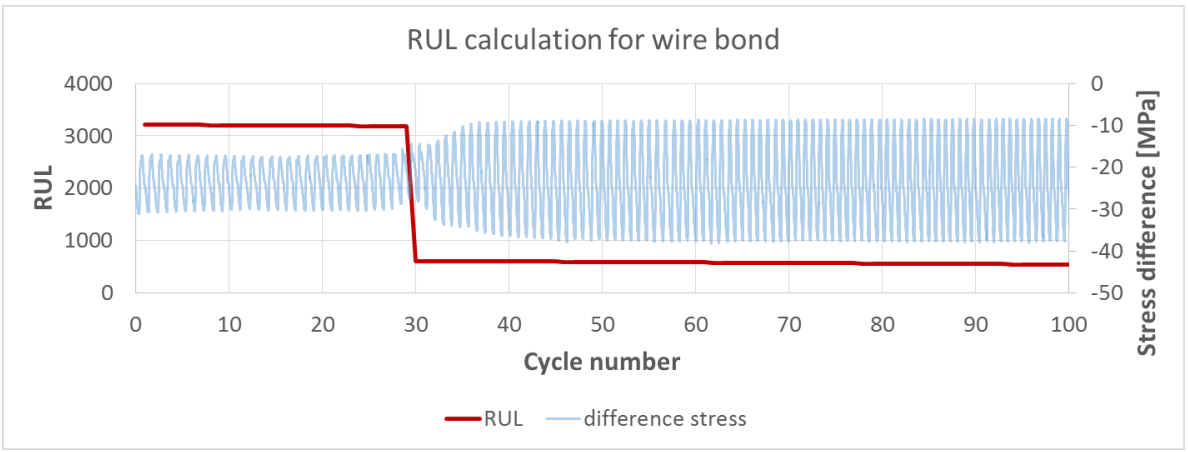

(b)

Figure 8.2.1: RUL calculation for (a) a solder joint and (b) a wire bond.

In the future investigations, the focus should be on optimizing the package of the sensor and its location in the system to enable the most efficient detection of the delamination in the critical regions. The sensor should be placed in direct vicinity of the critical design element to ensure a reliable failure detection. Additionally, this would help the sensor signal to be directly related to the load acting on the investigated design element. It would also be reasonable to consider integrating the sensor in the microelectronic package that is expected to fail first, or even integrating it within the silicon chip of this package. In this way, the same material properties which affect the stress state in the investigated design element would also affect the stresses measured with the piezoresistive stress sensor.

Chapter 9

Summary

PHM is a promising field of research in the reliability domain. Its main aim is to evaluate the reliability of a device in the real working conditions. Implementation of this methodology is especially attractive for automotive applications as the technology develops towards autonomous driving. This technology will likely address many needs of our fast developing world—it could increase vehicle traffic safety, and it could also reduce exhaust emission and traffic jams. However, the autonomous driving system has to be very reliable, and as seen in this thesis, such a high reliability can be achieved using PHM methodology.

The PHM techniques can generally be divided into three groups—model-based, data-driven and fusion approaches. The model-based approach usually utilizes a detailed analysis of an investigated device. The goal of the analysis is to identify the possible failure modes and understand the mechanisms that activate them. Once this is achieved, a physics-of-failure model for the most vulnerable design elements can then be created. In-situ monitoring of a load acting on the investigated device completes the approach and enables the calculation of RUL. The data-driven approach is typically based on the monitoring of performance parameters of an investigated device and does not require prior knowledge on its construction, failure modes, or expected loads. It always involves the usage of algorithms for data analysis to detect the deviations of the investigated system behavior from norm and anomalies. Lastly, a fusion approach combines both model-based and data-driven approaches in order to produce a more reliable RUL prediction.

The main goal of this study is to develop a framework for the implementation of a piezoresistive silicon stress sensor to PHM methodology for automotive applications. This sensor is very promising for reliability monitoring, as it is able to measure stress values that are directly related to the damage. The initial challenge in this study was to apply a stress sensor for system-level monitoring. The findings show that it was possible to develop an approach to PHM involving this sensor. The aim is to develop a fusion approach, since it minimizes the drawbacks of using the model-based and data-driven approaches separately.

To realize the assumptions of this thesis, the fundamental work on the applicability of piezoresistive stress sensor on a system level was firstly conducted, as described in Chapter 3. At the beginning, the uncertainties related to the measurements with the stress sensor were quantified, and their sources were also identified. The major challenges in conducting accurate measurements using a CMOS piezoresistive stress sensor included the relationship between their characteristics and certain parameters—specifically in that their characteristics depend on the temperature and operating current. Also, the calculated stress values can be dependent on other components of stress that are assumed insignificant in the governing equations. To apply the sensor at a system level, it is recommended to estimate all the components of stress which appear in the governing equations in order to verify the accuracy of the conducted measurements. Additionally, this thesis developed and tested a novel acquisition unit that enables gathering the data from a large number of sensors. Only using a miniaturized system with multiple measurement channels enabled the collection of sufficient data which are essential when applying the piezoresistive silicon stress sensor for system-level monitoring.

After accomplishing the initial preparatory stage of this research, a methodology for a fusion approach to PHM was prepared. This was achieved in three stages. First, to obtain an insight into the thermo-mechanical behavior of an investigated test vehicle, a detailed FEM modeling was performed. The chosen approach is described in details in Chapter 5. The development of a model included detailed geometry preparation, material modelling, and accurate definitions of boundary conditions. The active operation of the investigated test vehicle was simulated using coupled solutions of electro-thermal, thermal, and thermo-mechanical models to determine the exact loading conditions. Then, the model was verified using the moiré interferometry technique, which is a full field optical measurement method that can determine the in-plane deformations within the whole cross section of a test vehicle. It also allows an accurate modeling verification, including the behavior of all used materials. Two challenges encountered in making these measurements involves using an unusually large surface of the sample and also conducting the measurements under an active thermal loading condition. Following this, a model-based approach was developed, as described in Chapter 6. The model-based approach preparation started with using FMMEA to determine the most vulnerable design elements and the possible mechanisms of failure. The delamination between a copper lead frame and molding compound, solder fatigue and wire-bond lift-off were identified as the leading mechanisms of failure. Next, the physics-of-failure models for solder fatigue and wire-bond lift-off were established and the defined damage parameters were extracted from the validated simulation. Additionally, reliability tests were performed to verify the methodology. Four groups of test vehicles were tested—these were with/without outer mold, subjected to active and passive cycling. During thermal cycling the test vehicles were monitored using piezoresistive stress sensors, which recorded not only the stress, but also temperature values. The stress sensor signal was correlated with the load acting on the damage parameters by means of FEM simulations. This allowed a real-time evaluation of RUL for the tested devices.

Next, the study developed a data-driven approach based on measurements from the stress sensor. When a failure such as delamination occurs, the thermo-mechanical behavior of the device changes. This change can be detected using a piezoresistive stress sensor, as it reacts directly to mechanical loads. A developed data-driven approach focuses on delamination detection based on a monitoring signal. The data-driven methodology utilizes statistical pattern recognition methods in order to ensure that damage detection would take place in an automatic and reliable way. MD and SVD were studied for damage detection; the MD algorithm showed a better performance when it was applied to the stress sensor data. Additionally, an SVM approach was tested to see whether it can be used for damage classification. Findings show that the approach could detect a fault based on a signal from the stress sensor, and it could also identify the type of the fault. A recommendation was made to use both damage detection and damage classification algorithms in order to avoid situations where an unknown previously failure is classified as a healthy behavior.

Finally, a way to combine both developed approaches was proposed. In this approach, the investigated product should be monitored using a piezoresistive stress sensor. Then, the RUL of an investigated product should be calculated based on the developed physics-of-failure model and monitoring signal. Simultaneously, a data-driven approach should be used to detect any anomalies in the stress signal. If a damage is detected, the physics-of-failure model can be updated so that the model takes the changed loading conditions into consideration, which consequently leads to a more accurate prediction of RUL.

9.1 Conclusions

In this study, it was shown that the piezoresistive stress sensor can be implemented to monitor the state of health of an ECU. My original contribution to the knowledge gap includes the development of a framework to apply the piezoresistive silicon stress sensor on a system level as well as proposing a fusion approach to PHM using the sensor. This includes the development of a real-time monitoring method, a physics-of-failure approach, and a data-driven approach to PHM, based on piezoresistive silicon stress sensor measurements.

First, the study extended the applicability of piezoresistive stress sensor. Additionally, the uncertainties on a system level were quantified, and the study recommends that an estimation should be firstly made for both the z-component and the sum of in-plane stresses that act on the silicon die before applying the sensor on a system level. The reason for this is so that more accurate measurements can be made. Furthermore, the study developed an approach for the detailed modeling of complex loading conditions. Moreover, a method for accurate stress results extraction from the stress sensor simulation was found—specifically at the location where the stress is evaluated exactly in the regions where it is measured. The study also proposed a model-based approach to prognostics based on monitoring using the stress sensor. To verify the approach, the reliability test were planned and performed. Following this, the study proposed a data driven approach to prognostics based on measurements with the stress sensor. The statistical pattern recognition techniques—MD and SVD—were studied for damage detection. It was found that MD is more suitable for damage detection based on the stress sensor signal. MD requires the same computational power as SVD, but it is able to detect the fault earlier. Moreover, the study found that a failure can be detected and also isolated based on the stress sensor signal. Finally, the study proposed to combine both the developed methods; the proposed fusion approach used a data-driven approach for delamination detection so that the physics-of-failure model can be continually updated for a more accurate estimation of RUL.

9.2 Outlook

The future research should focus on gathering stress measurement data during damage initiation and progression. It is recommended to design a test vehicle where failure occurs much earlier. Furthermore, the damage should occur in a controlled way. To ensure high stresses acting on critical design elements, a couple of approaches can be used, such as 1) designing a very stiff construction, 2) using materials that have large mismatch in thermal expansion coefficients or by making the construction weaker, 3) minimizing adhesion between the layers, and 4) reducing the size of solder joints or the diameter of wire bond. FEM modelling should be implemented in the design process of such specimens. The data gathered from the prepared specimens should be used to develop a database of stress sensor response with different failures for the data-driven approach. The minimal damage size detectable by the sensor should be determined. Furthermore, it should be investigated how the distance to the damage affects the sensor signal.

Additionally, the packaging of the sensor in a more robust way should be considered. It would be most advantageous to encapsulate the sensor directly in the package of interest. Also, the position of the stress sensor in the system should be determined with the help of FEM modeling. The location should be chosen in such a way that maximizes the stresses acting on the die so that damage could occur there first. Aside from this, the sensitivity of a sensor to the damage could be maximized by an appropriate placement of the sensor.

Moreover, the model order reduction technique should be developed to enable real time evaluation of damage parameters for the physics-of-failure model. Then, it should be implemented in the acquisition unit that gathers the data from the sensors. Furthermore, data reduction algorithms that enable the gathering of the data in the field for long time periods should be established. Then, the Miner's rule should be implemented to evaluate the RUL under varying load conditions.

Finally, a study to validate the developed approach should be conducted. It should involve reliability testing with an irregular loading profile. This would allow the validation of a method in conditions similar to the field. An approach to take irregular load history into account while calculating RUL should also be proposed. This is important not only for model-based approaches; data-driven approaches should be tested against irregular load conditions also. Ultimately, the methodology should be tested in a real field conditions to monitor an ECU working under the engine hood.

Bibliography

[1] *Bosch Mobility Solutions*, `http://products.bosch-mobility-solutions.com/en/de/specials/specials_safety/automated_driving/motivation_and_conditions/motivation_1/motivation.html`, 2015.

[2] *The Daily Telegraph UK*, `http://www.telegraph.co.uk/motoring/news/10699415/Complex-car/-electronics/-spark-rise-in-breakdowns.html`, 2014.

[3] M. Pecht, *Prognostics and Health Management of Electronics*, John Wiley & Sons, Inc., ISBN 9780470278024, 25 FEB 2008.

[4] A. Sasi, A. Yadur, P. Gromala, *Simulation driven design of novel integrated circuits - Part 1: Selection of the materials based on the Virtual DoE*, 2015 16th International Conference on Thermal, Mechanical and Multi-Physics Simulation and Experiments in Microelectronics and Microsystems (EuroSimE), pp.1-7, 19-22 April 2015.

[5] P. Gromala, B. Muthuraman, B. Öztürk, H. Yan, K.M.B. Jansen, L. Ernst, *Simulation driven design of novel integrated circuits - Part 2: Constitutive material modeling of thermosets*, 2015 IEEE 65th Electronic Components and Technology Conference (ECTC), pp.1894-1900, 26-29 May 2015.

[6] P. Gromala, B. Muthuraman, B. Öztürk, K.M.B Jansen, L. Ernst, *Material Characterization and Nonlinear Viscoelastic Modelling of Epoxy Based Thermosets for Automotive Application*, 16th International Conference on Thermal, Mechanical and Multi-Physics Simulation and Experiments in Microelectronics and Microsystems, EuroSimE 2015,19-22 April 2015, Budapest, Hungary.

[7] D.S. Kim, B. Han, A. Yadur, P.J. Gromala, *Electronic control package model calibration using moiré interferometry*, 2014 15th international conference on Thermal, mechanical and multi-physics simulation and experiments in microelectronics and microsystems (eurosime), pp.1-5, 7-9 April 2014.

[8] M. Riccio, A. Irace, G. Breglio, P. Spirito, V. Kosel, M. Glavanovics, A. Satka, *Thermal simulation and ultrafast IR temperature mapping of a Smart Power Switch for automotive applications*, 21st International Symposium on Power Semiconductor Devices & IC's, ISPSD 2009, pp.200-203, 14-18 June 2009.

[9] X. Jorda, M. Vellvehi, X. Perpiny, J.L. Galvez, P. Godignon, *Validation of Dynamic Thermal Simulations of Power Assemblies Using a Thermal Test Chip*, International Conference on Mechanical and Multi-Physics Simulation Experiments in Microelectronics and Micro-Systems, EuroSime 2007, pp.1-6, 16-18 April 2007.

[10] L. Dupont, S. Lefebvre, Z. Khatir, J. C. Faugiere, *Power cycling test circuit for thermal fatigue resistance analysis of solder joints in IGBT*, 10th European Conference on Power Electronics and Applications.

[11] P. Gromala, J. Duerr, M. Dressler, K.M.B. Jansen, M. Hawryluk; J. de Vreugd, *Comprehensive material characterization and method of its validation by means of FEM simulation*, 12th International Conference on Thermal, Mechanical and Multi-Physics Simulation and Experiments in Microelectronics and Microsystems (EuroSimE), pp.1-8, 18-20 April 2011.

[12] B. Wu, D.S. Kim, B. Han, A. Palczynska, P. Gromala, *Thermal deformation analysis of automotive electronic control units subjected to passive and active thermal conditions*, 16th International Conference on Thermal, Mechanical and Multi-Physics Simulation and Experiments in Microelectronics and Microsystems (EuroSimE), pp.1-6, 19-22 April 2015.

[13] P. Gromala, S. Fischer, T. Zoller, A. Andreescu, J. Duerr, M. Rapp, J. Wilde, *Internal Stress State Measurements of the Large Molded Electronic Control Units*, 14th International Conference on Thermal, Mechanical and Multi-Physics Simulation and Experiments in Microelectronics and Microsystems, EuroSimE 2013, 15-17 April 2013, Wroclaw, Poland.

[14] N. Schafet, C. Lemm, U. Becker, H. Guttler, P. Schmid, *Development of a submodel technique for the simulation of solder joint fatigue of electronic devices mounted within an assembled ECU*, 10th International Conference on Thermal, Mechanical and Multi-Physics simulation and Experiments in Microelectronics and Microsystems, EuroSimE 2009, pp.1-8, 26-29 April 2009.

[15] M. Pecht, J. Gu, *Physics-of-failure-based prognostics for electronic products*, Transactions of the Institute of Measurement and Control June/August 2009 vol. 31 no. 3-4 309-322.

[16] C.Y. Yin, H. Lu, M. Musallam, C. Bailey, C.M. Johnson, *A Physics-of-failure based Prognostic Method for Power Modules*, 10th Electronics Packaging Technology Conference, EPTC, pp.1190,1195, 9-12 Dec. 2008.

[17] S. Mishra, M. Pecht, T. Smith, I. McNee, and R. Harris, *Remaining life prediction of electronic products using life consumption monitoring approach*, in Proc. Eur. Microelectron. Packag. Interconnection Symp., Cracow, Poland, Jun. 16–18, 2002, pp. 136–142.

[18] A. Ramakrishnan and M. Pecht, *A life consumption monitoring methodology for electronic systems*, IEEE Trans. Comp. Packag. Technol., vol. 26, no. 3, pp. 625–634, Sep. 2003.

[19] L. Nasser and M. Curtin, *Electronics reliability prognosis through material modeling and simulation*, 2006 IEEE Aerospace Conference, Big Sky, MT.

[20] E. Suhir, *Aerospace-electronics reliability-assurance (AERA): Three-step prognostics-and-health-monitoring (PHM) modeling approach*, 17th International Conference on Thermal, Mechanical and Multi-Physics Simulation and Experiments in Microelectronics and Microsystems (EuroSimE), Montpellier, 2016, pp. 1-14.

[21] S. Gierschner, T. Rump, H. G. Eckel, *Lifetime estimation for three level converter for wind energy application*, IEEE 6th International Symposium on Power Electronics for Distributed Generation Systems (PEDG), Aachen, 2015, pp. 1-8.

[22] N. Vichare, P. Rodgers, V. Eveloy, M. G. Pecht, *Monitoring environment and usage of electronic products for health assessment and product design*, in Proc. IEEE Workshop Accelerated Stress Testing Reliability (ASTR), Austin, TX, Oct. 2–5, 2005.

[23] H. Oh, M. H. Azarian, M. Pecht, C. H. White, R. C. Sohaney and E. Rhem, *Physics-of-failure approach for fan PHM in electronics applications*, 2010 Prognostics and System Health Management Conference, Macao, 2010, pp. 1-6.

[24] J. Gu, N. Vichare, T. Tracy, M. Pecht, *Prognostics implementation methods for electronics*, Annual Reliability and Maintainability Symposium, RAMS, Orlando 2007.

[25] M. Pecht, *Prognostics and health monitoring of electronics*, International Conference on Electronic Materials and Packaging, EMAP 2006, Kowloon 2006.

[26] BS 5760 Part 5, *Reliability of systems, equipment and components*, Guide to failure modes, effects and criticality analysis (FMEA and FMECA), 1991.

[27] A. Goel, R.J. Graves, *Using Failure Mode Effect Analysis to Increase Electronic Systems Reliability*, 30th International Spring Seminar on Electronics Technology, , pp.128-133, 9-13 May 2007.

[28] H. Ljazzar, M. Fischer, L. Grunske, M. Kuntz, F. Leitner-Fischer, S. Leue, *Safety Analysis of an Airbag System Using Probabilistic FMEA and Probabilistic Counterexamples*, Sixth International Conference on the Quantitative Evaluation of Systems, QEST '09, pp.299-308, 13-16 Sept. 2009.

[29] X.P. Zhu, L.B. Zhang, W. Liang, G.N. Shi, *A quantitative comprehensive safety evaluation method for centrifugal compressors using FMEA-fuzzy operations*, 2nd International Symposium on Instrumentation and Measurement, Sensor Network and Automation (IMSNA), pp.202-206, 23-24 Dec. 2013.

[30] M. Hillenbrand, M. Heinz; N. Adler, J. Matheis, K.D. Muller-Glaser, *Failure mode and effect analysis based on electric and electronic architectures of vehicles to support the safety lifecycle ISO/DIS 26262*, 21st IEEE International Symposium on Rapid System Prototyping (RSP), pp.1-7, 8-11 June 2010.

[31] S. Mathew, D. Das, R. Rossenberger, M. Pecht, *Failure mechanisms based prognostics*, International Conference on Prognostics and Health Management, PHM, pp.1-6, 6-9 Oct. 2008.

[32] S. Mathew, M. Alam and M. Pecht, *Identification of Failure Mechanisms to Enhance Prognostic Outcomes*, Journal of Failure Analysis and Prevention: Volume 12, Issue 1, Pg. 66-73, 2012.

[33] F. Li, M. Pecht, D. Lau and Gang Niu, *The research and application of the method of life consumption monitoring based on physics of failure*, Electronic Packaging Technology & High Density Packaging (ICEPT-HDP), 2010 11th International Conference on, Xi'an, 2010, pp. 1027-1033.

[34] W.J. Crichlow, A.J. McCulloch, L. Young, M. A. Melcon, *An engineering evaluation of methods for the prediction of structural fatigue from measured flight parameters*, Defense Documentation Center for Scientific and Technical Information, Cameron Station Alexandria, Virginia, March 1962.

[35] M.A. Miner, *Cumulative damage in fatigue*, Journal of Applied Mechanics, pp. A-159 to A-164, September 1945.

[36] P. Borgesen, S. Hamasha, M. Obaidat, V. Raghavan, X. Dai, M. Meilunas, M. Anselm, *Solder joint reliability under realistic service conditions*, Microelectronics Reliability, Volume 53, Issues 9–11, 2013, pp.1587-1591.

[37] J. Gu, D. Barker, M. Pecht, *Prognostics implementation of electronics under vibration loading*, Microelectronics Reliability, Volume 47, Issue 12, Pages 1849-1856, December 2007.

[38] J. Gu, D. Barker, M. Pecht, *Uncertainty assessment of prognostics implementation of electronics under vibration loading*, AAAI Fall Symposium on Artificial Intelligence for Prognostics, Arlington, VA.

[39] Y. Xing, Q. Miao, K. L. Tsui and M. Pecht, *Prognostics and health monitoring for lithium-ion battery*, 2011 IEEE International Conference on Intelligence and Security Informatics (ISI), pp. 242-247, Beijing, 2011.

[40] P. Lall, R. Lowe, K. Goebel, *Particle filter models and phase sensitive detection for prognostication and health monitoring of leadfree electronics under shock and vibration*, IEEE 61st Electronic Components and Technology Conference (ECTC), pp.1097-1109, May 31-June 3 2011.

[41] S. Kumar, T.W.S. Chow, M. Pecht, *Approach to Fault Identification for Electronic Products Using Mahalanobis Distance*, IEEE Transactions on Instrumentation and Measurement, vol.59, no.8, pp.2055-2064, Aug. 2010.

[42] V. A. Sotiris, M. Pecht, *Support Vector Prognostics Analysis of Electronic Products and Systems*, Artificial Intelligence for Prognostics, AAAI Fall Symposium Series, Arlington, VA, November 9-11, 2007.

[43] P. Lall, P. Choudhary,S. Gupte, J. Suhling, *Health monitoring for damage initiation & progression during mechanical shock in electronic assemblies*, Proceedings of 56th Electronic Components and Technology Conference, 2006.

[44] S.M. Namburu, M. Wilcutts, S. Chigusa, Q. Liu, K. Choi, K. Pattipati, *Systematic Data-Driven Approach to Real-Time Fault Detection and Diagnosis in Automotive Engines*, IEEE Autotestcon, pp.59,65, 18-21 Sept. 2006.

[45] T. Petsche, A. Marcantonio, C. Darken, S.J. Hanson , G.M. Kuhn, I. Santoso, *A Neural Network Autoassociator for Induction Motor Failure Prediction*, Proceedings of the 1995 Conference of Advances in Neural Information Processing Systems 8, The MIT Press, Cambridge, Massachusets.

[46] L. Lopez, *Advanced electronic prognostics through system telemetry and pattern recognition methods*, Microelectronics Reliability, Volume 47, Issue 12, December 2007.

[47] N. Patil, D. Das, M. Pecht, *Anomaly detection for IGBTs using Mahalanobis distance*, Microelectronics Reliability, Volume 55, Issue 7, June 2015, Pages 1054-1059.

[48] A. Oukaour, B. Tala-Ighil, B. Pouderoux, M. Tounsi, M. Bouarroudj-Berkani, S. Lefebvre, B. Boudart, *Ageing defect detection on IGBT power modules by artificial training methods based on pattern recognition*, Microelectronics Reliability, Volume 51, Issue 2, February 2011, Pages 386-391.

[49] K.-C. Yung, B. Sun, X. Jiang, *Prognostics-based qualification of high-power white LEDs using Levy process approach*, Mechanical Systems and Signal Processing, Available online 26 May 2016.

[50] D. Liu, S. Wang, Y. Peng and X. Peng, *On-line adaptive data-driven fault prognostics of complex systems*, 2011 IEEE AUTOTESTCON, Baltimore, MD, 2011, pp. 166-173.

[51] H. Pan, E. Dong, Y. Jiang and P. Zhang, *Prognostic and health management for aircraft electrical power supply system*, Prognostics and System Health Management (PHM), 2012 IEEE Conference on, Beijing, 2012, pp. 1-5.

[52] L. Song, Z. Hu, J. Wang, H. Zhou, *Data-driven fault detection design for satellite's attitude control system*, Prognostics and System Health Management Conference, Hunan, Zhangiiaijie, 2014, pp. 237-244.

[53] A. Rezaei, A. Dadouche, *Development of a turbojet engine gearbox test rig for prognostics and health management*, Mechanical Systems and Signal Processing, Volume 33, November 2012, Pages 299-311.

[54] J. Dai, D. Das, M. Pecht, *Prognostics-based risk mitigation for telecom equipment under free air cooling conditions*, Applied Energy, Volume 99, November 2012, Pages 423-429.

[55] P. Baraldi, F. Mangili, E. Zio, *A prognostics approach to nuclear component degradation modeling based on Gaussian Process Regression*, Progress in Nuclear Energy, Volume 78, January 2015, Pages 141-154, ISSN 0149-1970.

[56] G. Niu, B.S. Yang, *Intelligent condition monitoring and prognostics system based on data-fusion strategy*, Expert Systems with Applications, Volume 37, Issue 12, December 2010, Pages 8831-8840.

[57] S. Kumar, V. Sotiris and M. Pecht, *Mahalanobis Distance and Projection Pursuit Analysis for Health Assessment of Electronic Systems*, IEEE Aerospace Conference, Big Sky, MT, 2008, pp. 1-9.

[58] P. Lall, D. Iyengar, S. Shantaram, P. Gupta, D. Panchagade and J. Suhling, *Feature extraction and health monitoring using image correlation for survivability of leadfree packaging under shock and vibration*, International Conference on Thermal, Mechanical and Multi-Physics Simulation and Experiments in Microelectronics and Micro-Systems, EuroSimE, Freiburg im Breisgau, 2008, pp. 1-15.

[59] T. Sutharssan, C. Bailey, S. Stoyanov and Y. Rosunally, *Prognostics and reliability assessment of light emitting diode packaging*, 12th International Conference on Electronic Packaging Technology and High Density Packaging (ICEPT-HDP), Shanghai, 2011, pp. 1-7.

[60] T. Sutharssan, S. Stoyanov, C. Bailey and Y. Rosunally, *Data analysis techniques for real-time prognostics and health management of semiconductor devices*, 18th European Microelectronics and Packaging Conference (EMPC), Brighton, 2011, pp. 1-7.

[61] Y. Wang, Q. Miao and M. Pecht, *Health monitoring of hard disk drive based on Mahalanobis distance*, Prognostics and System Health Managment Confernece, Shenzhen, 2011, pp. 1-8.

[62] J. Fan, C. Qian, X. Fan, G. Zhang and M. Pecht, *In-situ monitoring and anomaly detection for LED packages using a Mahalanobis distance approach*, First International Conference on Reliability Systems Engineering (ICRSE), Beijing, 2015, pp. 1-6.

[63] X. Jin, E. W. M. Ma, L. L. Cheng and M. Pecht, *Health Monitoring of Cooling Fans Based on Mahalanobis Distance With mRMR Feature Selection*, in IEEE Transactions on Instrumentation and Measurement, vol. 61, no. 8, pp. 2222-2229, Aug. 2012.

[64] J. L. Godwin and P. Matthews, *Prognosis of wind turbine gearbox failures by utilising robust multivariate statistical techniques*, IEEE Conference on Prognostics and Health Management (PHM), Gaithersburg, MD, 2013, pp. 1-8.

[65] R. Krishnan and S. Jagannathan, *Hierarchical Mahalanobis Distance Clustering Based Technique for Prognostics in Applications Generating Big Data*, IEEE Symposium Series on Computational Intelligence, Cape Town, 2015, pp. 516-521.

[66] M. Gosnell and R. Woodley, *Exploring the Mahalanobis-Taguchi approach to extract vehicle prognostics and diagnostics*, IEEE Symposium on Computational Intelligence in Vehicles and Transportation Systems (CIVTS), Orlando, FL, 2014, pp. 84-91.

[67] A. Soylemezoglu, S. Jagannathan and C. Saygin, *Mahalanobis-Taguchi System as a Multi-Sensor Based Decision Making Prognostics Tool for Centrifugal Pump Failures*, in IEEE Transactions on Reliability, vol. 60, no. 4, pp. 864-878, Dec. 2011.

[68] S. Vanlanduit, E. Parloo, B. Cauberghe, P. Guillaume, P. Verboven, *A robust singular value decomposition for damage detection under changing operating conditions and structural uncertainties*, Journal of Sound and Vibration, Volume 284, Issues 3—5, 21 June 2005, Pages 1033—1050, ISSN 0022—460X.

[69] R. Hajrya, N. Mechbal, M. Verge, *Proper orthogonal decomposition applied to structural health monitoring*, Communications, Computing and Control Applications (CCCA), 2011 International Conference on , vol., no., pp.1-6, 3-5 March 2011.

[70] R. Ruotolo, C. Surace, *Using SVD to Detect Damage in Structures with Different Operational Conditions*, Journal of Sound and Vibration, Volume 226, Issue 3, 23 September 1999, Pages 425-439, ISSN 0022-460X.

[71] M.F. Abu El-Yazeed, *An integrated approach for analog circuit testing using autocorrelation analysis, singular value decomposition and probabilistic neural network*, Proceedings of the 15th International Conference on Microelectronics, 2003.

[72] S. Zhou, J. Zhang, S. Wang, *Fault diagnosis in industrial processes using principal component analysis and hidden Markov model*, Proceedings of the 2004 American Control Conference, Boston, MA, USA, 2004, pp. 5680-5685

[73] Q. P. He, J. Wang, *Fault Detection Using the k-Nearest Neighbor Rule for Semiconductor Manufacturing Processes*, in IEEE Transactions on Semiconductor Manufacturing, vol. 20, no. 4, pp. 345-354, Nov. 2007.

[74] S. Bouhouche, M. Lahreche, A. Moussaoui, J. Bast, *Quality Monitoring Using Principal Component Analysis and Fuzzy Logic Application in Continuous Casting Process*, American Journal of Applied Sciences, 2007, Volume 4, Issue 9, Pages 637-644

[75] D. Lixiang, Z. Laibin, L. Feng, *Feature Reduction Integrated with Distance Measure and SVD and Its Application in Mechanic Fault Diagnosis*, International Forum on Information Technology and Applications, Chengdu, 2009, pp. 391-393.

[76] C. Cempel, *Generalized singular value decomposition in multidimensional condition monitoring of machines—A proposal of comparative diagnostics*, Mechanical Systems and Signal Processing, Volume 23, Issue 3, April 2009, Pages 701-711.

[77] R. Li, D. Wang, P. Han, T. Wang, *On the applications of SVD in fault diagnosis*, IEEE International Conference on Systems, Man and Cybernetics, 2003, pp. 3763-3768 vol.4.

[78] C. Peng, Z. Ying, D. Enzeng, L. Xin, *Fault detection algorithm of inverter based on singular value decomposition nonlinear filtering*, IEEE International Conference on Computer Science and Automation Engineering (CSAE), Shanghai, 2011, pp. 85-89.

[79] Z. Zhu, Y. Sun, *Application of EMD and SVD in fault identification*, International Power Engineering Conference (IPEC), Singapore, 2007, pp. 1247-1250.

[80] V. Vapnik, *Estimation of Dependences Based on Empirical Data*, Springer Verlag, 1982

[81] C. J.C. Burges, *A Tutorial on Support Vector Machines for Pattern Recognition*, Data Mining and Knowledge Discovery, 1998, Volume 2, Number 2, Page 121.

[82] S. Poyhonen, M. Negrea, P. Jover, A. Arkkio, H. Hyotyniemi, *Numerical magnetic field analysis and signal processing for fault diagnostics of electrical machines*, The International Journal for Computation and Mathematics in Electrical and Electronic Engineering 22, number 4, pages 969-981.

[83] J. Wang, J. Shi and Q. He, *Research on component-level health quantitative assessment based on SVM algorithm for analog electronic circuits*, Prognostics and System Health Management Conference (PHM), 2015, Beijing, 2015, pp. 1-5.

[84] J. Kang, X. Zhang, J. Zhao, H. Teng, D. Cao, *Gearbox fault diagnosis method based on wavelet packet analysis and support vector machine*, IEEE Conference on Prognostics and System Health Management (PHM), Beijing, 2012, pp. 1-13.

[85] M. A. Taie, M. Diab, M. ElHelw, *Remote prognosis, diagnosis and maintenance for automotive architecture based on least squares support vector machine and multiple classifiers*, 4th International Congress on Ultra Modern Telecommunications and Control Systems and Workshops (ICUMT), St. Petersburg, 2012, pp. 128-134.

[86] W. Qiancheng, Z. Shunong, K. Rui, *Research of small samples avionics prognostics based on Support Vector Machine*, 2011 Prognostics and System Health Managment Conference, Shenzhen, 2011, pp. 1-5.

[87] R. de Pádua Moreira, C. L. Nascimento, *Prognostics of aircraft bleed valves using a SVM classification algorithm*, IEEE Aerospace Conference, Big Sky, MT, 2012, pp. 1-8.

[88] L. Xiong, H. D. Ma, H. Z. Fang, K. X. Zou, D. W. Yi, *Anomaly detection of spacecraft based on least squares support vector machine*, Prognostics and System Health Managment Conference, Shenzhen, 2011, pp. 1-6.

[89] A, Nuhic, T. Terzimehic, T. Soczka-Guth, M. Buchholz, K. Dietmayer, *Health diagnosis and remaining useful life prognostics of lithium-ion batteries using data-driven methods*, Journal of Power Sources, Volume 239, 1 October 2013, Pages 680-688

[90] J. Liu, R. Seraoui, V. Vitelli, E. Zio, *Nuclear power plant components condition monitoring by probabilistic support vector machine*, Annals of Nuclear Energy, vol. 56, pp. 23-33, 2013.

[91] H. Zhang, R. Kang, M. Pecht, *A hybrid prognostics and health management approach for condition-based maintenance*, IEEE International Conference on Industrial Engineering and Engineering Management, Hong Kong, 2009, pp. 1165-1169.

[92] G. J. Kacprzynski, M. J. Roemer, G. Modgil, A. Palladino and K. Maynard, *Enhancement of physics-of-failure prognostic models with system level features*, IEEE Aerospace Conference Proceedings, 2002, pp. 6-2919-6-2925 vol.6.

[93] G. Zhang, C. Kwan, R. Xu, N. Vichare, M. Pecht, *An Enhanced Prognostic Model for Intermittent Failures in Digital Electronics*, 2007 IEEE Aerospace Conference, Big Sky, MT, 2007, pp. 1-8.

[94] S. Cheng, M. Pecht, *A fusion prognostics method for remaining useful life prediction of electronic products*, IEEE International Conference on Automation Science and Engineering CASE 2009, Bangalore 2009.

[95] C. Chen, M. Pecht, *Prognostics of lithium-ion batteries using model-based and data-driven methods*, IEEE Conference on Prognostics and System Health Management (PHM), Beijing, 2012, pp. 1-6.

[96] Robert Bosch GmbH, *Electrical and electronic systems in the vehicle*, in Bosch Automotive Electrics and Automotive Electronics, Systems and Components, Networking and Hybrid Drive, 5th Edition, Springer Fachmedien Wiesbaden, 2014.

[97] M. Melito, *Car ignition with IGBTs*, Application Note, STMicroelectronics, 1999.

[98] Fairchild TM, *AN-8208, Introduction to Automotive Ignition Systems*, Fairchild Semiconductor Corporation, Rev. 1.0.0, April 2014.

[99] A. Palczynska, F. Pesth, P. J. Gromala, T. Melz and D. Mayer, *Acquisition unit for in-situ stress measurements in smart electronic systems*, 15th International Conference on Thermal, Mechanical and Multi-Physics Simulation and Experiments in Microelectronics and Microsystems (EuroSimE), Ghent, 2014.

[100] A. Palczynska, P. Gromala, B. Han, D. Mayer, T. Melz, *On the Accuracy of CMOS-based Piezoresistive Stress Sensor: Theory and Experiment*, In Preparation.

[101] J.C. Suhling, R.C. Jaeger, *Silicon piezoresistive stress sensors and their application in electronic packaging*, IEEE Sensors Journal, vol.1, no.1, pp.14-30, June 2001.

[102] R.C. Jaeger, J.C. Suhling, R. Ramani, A.T. Bradley, X. Jianping, *CMOS stress sensors on [100] silicon*, IEEE Journal of Solid-State Circuits, vol.35, no.1, pp.85-95, Jan. 2000.

[103] R.C. Jaeger, R. Ramani, J.C. Suhling, K. Yanling, *CMOS stress sensor circuits using piezoresistive field-effect transistors (PIFETs)*, Digest of Technical Papers, Symposium on VLSI Circuits, pp.43-44, 8-10 June 1995.

[104] C. Yonggang, R.C. Jaeger, J.C. Suhling, *CMOS Sensor Arrays for High Resolution Die Stress Mapping in Packaged Integrated Circuits*, IEEE Sensors Journal, vol.13, no.6, pp.2066-2076, June 2013.

[105] C. Yonggang, R.C. Jaeger, J.C. Suhling, *Multiplexed CMOS Sensor Arrays for Die Stress Mapping*, Proceedings of the 32nd European Solid-State Circuits Conference, ESSCIRC 2006, pp.424-427, 19-21 Sept. 2006.

[106] A. T. Bradley, R.C. Jaeger, J.C. Suhling, Y. Zou, *Test chips for die stress characterization using arrays of CMOS sensors*, Proceedings of the IEEE Custom Integrated Circuits, 1999, pp.147-150, 1999.

[107] A.T. Bradley, R.C. Jaeger, J.C. Suhling, Y. Zou *Die stress characterization using arrays of CMOS sensors*, Proceedings of the 24th European Solid-State Circuits Conference, ESSCIRC '98, pp.472-475, 22-24 Sept. 1998.

[108] S. Hussain, R.C. Jaeger, J.C. Suhling, *Current dependence of the piezoresistive coefficients of CMOS FETs on (100) silicon*, 44th European Solid State Device Research Conference (ESSDERC), 2014, pp.74-77, 22-26 Sept. 2014.

[109] T. Kaufmann, D. Kopp, F. Purkl, M. Baumann, P. Ruther, O. Paul, *Piezoresistive response of five-contact vertical Hall devices*, IEEE Sensors, pp.562-565, 1-4 Nov. 2010.

[110] B. Lemke, R. Baskaran, O. Paul, *Piezoresistive CMOS sensor for the localized measurement of five independent stress components*, IEEE 23rd International Conference on Micro Electro Mechanical Systems (MEMS), pp.596-599, 24-28 Jan. 2010.

[111] J. Bartholomeyczik, P. Ruther, O. Paul, *Multidimensional CMOS in-plane stress sensor*, Proceedings of IEEE Sensors, 2003, vol.1, pp.242-247,22-24 Oct. 2003.

[112] P. Gieschke, Y. Nurcahyo, M. Herrmann, M. Kuhl, P. Ruther, O. Paul, *CMOS Integrated Stress Mapping Chips with 32 N-Type or P-Type Piezoresistive Field Effect Transistors*, IEEE 22nd International Conference on Micro Electro Mechanical Systems (MEMS), pp.769-772, 25-29 Jan. 2009.

[113] P. Gieschke, J. Held, M. Doelle, J. Bartholomeyczik, P. Ruther, O. Paul, *Smart brush based on a high density CMOS stress sensor array and SU-8 microposts*, IEEE 20th International Conference on Micro Electro Mechanical Systems, 2007, pp.631-634, 21-25 Jan. 2007.

[114] M. Doelle, C. Peters, P. Ruther, O. Paul, *Piezo-FET stress-sensor arrays for wire-bonding characterization*, Journal of Microelectromechanical Systems, vol.15, no.1, pp.120-130, Feb. 2006.

[115] M. Doelle, C. Peters, P. Gieschke, P. Ruther, O. Paul, *Two-dimensional high density piezo-FET stress sensor arrays for in-situ monitoring of wire bonding processes*, 17th IEEE International Conference on Micro Electro Mechanical Systems (MEMS), 2004 pp.829-832, 2004.

[116] J. Roberts, S. Hussain, M.K. Rahim, M. Motalab, J.C. Suhling, R.C. Jaeger, P. Lall, Z. Ron, *Characterization of microprocessor chip stress distributions during component packaging and thermal cycling*, Proceedings of 60th Electronic Components and Technology Conference (ECTC), 2010, pp.1281-1295, 1-4 June 2010.

[117] J.C. Roberts, M.K. Rahim, S. Hussain, J.C. Suhling, R.C. Jaeger, P. Lall, *Die stress variation in area array components subjected to accelerated life testing*, 11th Intersociety Conference on Thermal and Thermomechanical Phenomena in Electronic Systems (ITHERM), pp.705-713, 28-31 May 2008.

[118] J. Roberts, M. Motalab, S. Hussain, J.C. Suhling, R.C. Jaeger, P. Lall, *Measurement of die stresses in microprocessor packaging due to thermal and power cycling*, IEEE 62nd Electronic Components and Technology Conference (ECTC), 2012, pp.756-770, May 29 2012-June 1 2012.

[119] M.K. Rahim, J. Roberts, J.C. Suhling, R.C. Jaeger, P. Lall, *Continuous In-Situ Die Stress Measurements During Thermal Cycling Accelerated Life Testing*, Proceedings of 57th Electronic Components and Technology Conference (ECTC), 2007, pp.1478-1489, May 29 2007-June 1 2007.

[120] F. Schindler-Saefkow, F. Rost, A. Otto, W. Faust, B. Wunderle, B. Michel, S. Rzepka, *Stress chip measurements of the internal package stress for process characterization and health monitoring*, 13th International Conference on Thermal, Mechanical and Multi-Physics Simulation and Experiments in Microelectronics and Microsystems (EuroSimE), 2012, pp.1/10-10/10, 16-18 April 2012.

[121] C. Yu-Yao, C. Hsien, L. Ben-Je Lwo, T. Kun-Fu, *In Situ Stress and Reliability Monitoring on Plastic Packaging Through Piezoresistive Stress Sensor*, IEEE Transactions on Components, Packaging and Manufacturing Technology, vol.3, no.8, pp.1358-1363, Aug. 2013.

[122] C. Yu-Yao, C. Hsien, L. Ben-Je, T. Ren-Tzung, T. Kun-Fu, *In-situ reliability monitoring on PBGA packaging through piezoresistive stress sensor*, 5th International Microsystems Packaging Assembly and Circuits Technology Conference (IMPACT), 2010 , pp.1-4, 20-22 Oct. 2010.

[123] P. Lall, M.N. Islam, M.K. Rahim, J.C. Suhling, *Prognostics and Health Management of Electronic Packaging*, IEEE Transactions on Components and Packaging Technologies, vol.29, no.3, pp.666-677, Sept. 2006.

[124] P. Lall, N. Islam, K. Rahim, J. Suhling, S. Gale, *Leading indicators-of-failure for prognosis of electronic and MEMS packaging*, Electronic Components and Technology Conference, 2004. Proceedings. 54th , vol.2, pp.1570-1578 Vol.2, 1-4 June 2004.

[125] A. Palczynska, B. Wu, D.S. Kim, P. Gromala, B. Han, D. Mayer, T. Melz, *Application of the IForce piezoresistive silicon based stress sensor for prognostic and health monitoring methods*, 2015 European Microelectronics Packaging Conference (EMPC), Friedrichshafen, 2015, pp. 1-6.

[126] P. Gromala, A. Palczynska, B. Han, *Prognostic approaches for the wirebond failure prediction in power semiconductors: A case study using DPAK package*, 16th International Conference on Electronic Packaging Technology (ICEPT), , pp.413-418, 11-14 Aug. 2015.

[127] A. Palczynska, P. J. Gromala, D. Mayer, B. Han and T. Melz, *In-situ investigation of EMC relaxation behavior using piezoresistive stress sensor*, International Conference on Thermal, Mechanical and Multi-Physics Simulation and Experiments in Microelectronics and Microsystems (EuroSimE), Budapest, 2015, pp. 1-5.

[128] H. Kittel, S. Endler, H. Osterwinter, S. Oesterle and F. Schindler-Saefkow, *Novel Stress Measurement System for Evaluation of Package Induced Stress*, 2nd European Conference & Exhibition on Integration Issues of Miniaturized Systems - MOMS, MOEMS, ICS and Electronic Components (SSI), Barcelona, Spain, 2008, pp. 1-8.

[129] Robert Bosch GmbH, *Abschlussbericht zum Verbundvorhaben iForceSens : Entwicklung eines integrierten Stressmesssystems zur Quantifizierung der 3D-Verformung von Sensorbauelementen in Abhängigkeit des Verpackungsprozesses*, Technische Informationsbibliothek u. Universitätsbibliothek, Abstatt, 2008.

[130] *IFORCESENS CHIRP CONTROL UNIT 30-004-A01 Instructions for Use*, Steinbeis GmbH & Co. KG für Technologietransfer, TZ Mikroelektronik, Göppingen, 2006.

[131] Analog Devices, *Quad, 12-/14-/16-Bit nanoDACs with 5 ppm/ °C On-Chip Reference, I2C Interface*, AD5625, Rev. D, 2007.

[132] Burr Brown Products from Texas Instruments, *12-bit, 52-kSPS, Data Acquisition System with Analog-to-Digital Converter, MUX, PGA and Reference*, ADS7870, Dec. 1999 [Revised Dec. 2005].

[133] Analog Devices, *4.5 Ω R_{ON}, 16-Channel, Differential 8-Channel,±5 V,+12 V,+5 V, and +3.3 V Multiplexers*, ADG1607, Rev. 0, 2009.

[134] Vishay Siliconix, *8-Ch/Dual 4-Ch High-Performance CMOS Analog Multiplexers*, DG408, S13-2504-Rev. K, Dec. 13.

[135] B. Van Zeghbroeck, *Principles of semiconductor devices*, University of Colorado, 2004.

[136] R.C. Jaeger, J.C. Suhling, R. Ramani *Errors associated with the design, calibration and application of piezoresistive stress sensors in (100) silicon*, IEEE Transactions on Components, Packaging, and Manufacturing Technology, Part B: Advanced Packaging, vol.17, no.1, pp.97-107, Feb 1994.

[137] S. Hussain, R.C. Jaeger, J.C. Suhling, J.C. Roberts, M.A. Motalab, C. Chun-Hyung, *Error analysis for piezoresistive stress sensors used in flip chip packaging*, 12th IEEE Intersociety Conference on Thermal and Thermomechanical Phenomena in Electronic Systems (ITherm), 2010, pp.1-12, 2-5 June 2010.

[138] E. Zukowski, T. Kimpel, D. Kraetschmer and A. Roessle, *Efficient modeling of printed circuit boards structures for dynamic simulations*, 16th International Conference on Thermal, Mechanical and Multi-Physics Simulation and Experiments in Microelectronics and Microsystems (EuroSimE), Budapest, 2015, pp. 1-5.

[139] Alicja Palczynska, Arun Sasi, Matthias Werner,Alexandru Prisacaru, Przemyslaw Gromala, Bongtae Han, Dirk Mayer, Tobias Melz, *Simulation Driven Design of Novel Integrated Circuits – Physics of Failure Simulation of the Electronic Control Modules for Harsh Environment Application*, 2016 IEEE 66th Electronic Components and Technology Conference (ECTC), Las Vegas, 2016.

[140] J. M. Hurley, *Estimating the Engineering Properties of Electronic Packaging Materials*, IEEE Transactions on Components and Packaging Technologies, vol. 31, no. 2, pp. 417-424, June 2008.

[141] N. Chawla, K. K. Chawla, *Matrix Materials*, Metal Matrix Composites, Springer US, 2006.

[142] P. Gromala, J. Reichelt, S. Rzepka, *Accurate thermal cycle lifetime estimation for BGA memory components with lead-free solder joints*, 10th International Conference on Thermal, Mechanical and Multi-Physics simulation and Experiments in Microelectronics and Microsystems, EuroSimE 2009, pp.1-9, 26-29 April 2009.

[143] D. Post, B. Han, *Moiré Interferometry*, Springer Handbook of Experimental Solid Mechanics, 2008, pp 627-654.

[144] S. Cho, B. Han, *Observing Real-time Thermal Deformations in Electronic Packaging*, Experimental Techniques, vol. 26 (2002), pp. 25-29.

[145] S. Cho, *Temperature dependent deformation analysis of ceramic ball grid array package assembly under accelerated thermal cycling condition*, Journal of Electronic Packaging, vol. 126 (2004), pp. 41-47.

[146] Guo, Y. et al., *Solder ball connect (SBC) assemblies under thermal loading: I. Deformation measurement via moiré interferometry, and its interpretation*, IBM Journal of Research and Development, vol. 37 (1993),pp. 635-648.

[147] J. H. Park, K. W. Jang, K. W. Paik and S. B. Lee, *A Study of Hygrothermal Behavior of ACF Flip Chip Packages With Moiré Interferometry*, IEEE Transactions on Components and Packaging Technologies (2010), vol. 33, no. 1, pp. 215-221.

[148] J. H. Park, K. W. Jang, K. W. Paik and S. B. Lee, *Reliability Evaluation for Flip-Chip Electronic Packages under High Temperature and Moisture Condition using Moiré*, Electronics Packaging Technology Conference (2008), Singapore, pp. 633-638.

[149] C. Jang, S. Yoon and B. Han, *Measurement of the Hygroscopic Swelling Coefficient of Thin Film Polymers Used in Semiconductor Packaging*, IEEE Transactions on Components and Packaging Technologies, vol. 33, no. 2, pp. 340-346, June 2010.

[150] B. Han, *Characterization of Stresses and Strains in Microelectronics and Photonics Devices Using Photomechanics Methods*, Springer US, 2007-01-01.

[151] H.D. Solomon, *Fatigue of 60/40 Solder*, IEEE Transactions on Components, Hybrids, and Manufacturing Technology, vol.9, no.4, pp.423-432, Dec 1986.

[152] W. Engelmaier, *Fatigue Life of Leadless Chip Carrier Solder Joints During Power Cycling*, IEEE Transactions on Components, Hybrids, and Manufacturing Technology, vol.6, no.3, pp.232-237, Sep 1983.

[153] A. Schubert, R. Dudek, E. Auerswald, A. Gollbardt, B. Michel, H. Reichl, *Fatigue life models for SnAgCu and SnPb solder joints evaluated by experiments and simulation*, Proceedings of 53rd Electronic Components and Technology Conference, pp.603-610, 30-30 May 2003.

[154] A. Syed, *Accumulated creep strain and energy density based thermal fatigue life prediction models for SnAgCu solder joints*, Proceedings of 54th Electronic Components and Technology Conference, pp.737-746 Vol.1, 1-4 June 2004.

[155] L. Yang, P.A. Agyakwa, C.M. Johnson, *Physics-of-Failure Lifetime Prediction Models for Wire Bond Interconnects in Power Electronic Modules*, IEEE Transactions on Device and Materials Reliability, vol.13, no.1, pp.9,17, March 2013.

[156] S. S.Manson, *Behaviour of materials under conditions of thermal stress*, NACA, Washington, DC, Rep. No. 1170, 1954

[157] O.H. Basquin, *The exponential law of endurance tests*, American Society of Testing Materials, vol. 10, pp. 625-630.

[158] M. Ciappa, *Selected failure mechanisms of modern power modules*, Microelectronics Reliability, Volume 42, Issues 4–5, April–May 2002, Pages 653-667

[159] W.W Lee, L.T Nguyen, G.S Selvaduray, *Solder joint fatigue models: review and applicability to chip scale packages*, Microelectronics Reliability, Volume 40, Issue 2, 28 February 2000, Pages 231-244.

[160] S. Knecht, *Integrated Matrix Creep: Application to Lifetime Prediction of Eutectic Tin-Lead Solder Joints*, MRS Proceedings, 203, 411

[161] A. R. Syed, *Thermal fatigue reliability enhancement of plastic ball grid array (PBGA) packages*, 46th Electronic Components and Technology Conference, Orlando, FL, 1996.

[162] R. Darveaux, K. Banerji, A. Mawer, and G. Dody, *Reliability of Plastic Ball Grid Array Assembly*, Ball Grid Array Technology, J. Lau Editor, McGraw-Hill, Inc., New York 1995

[163] G. Q. Zhang, W. D. Van Driel, X. J. Fan, *Mechanics of Microelectronics*, Solid mechanics and its applications, Volume 141, 2006.

[164] M.K. Rahim, J. Roberts, J.C. Suhling, R.C. Jaeger, P. Lall, *Continuous In-Situ Die Stress Measurements During Thermal Cycling Accelerated Life Testing*, Electronic Components and Technology Conference, 2007. ECTC '07. Proceedings. 57th, vol., no., pp.1478-1489, May 29 2007-June 1 2007.

[165] P. Lall, P. Choudhary, S. Gupte, *Health Monitoring for Damage Initiation & Progression during Mechanical Shock in Electronic Assemblies*, Proceedings of the 56th IEEE Electronic Components and Technology Conference, San Diego, California, pp.85-94, May 30- June 2, 2006.

[166] B. Saha, S. Poll, K. Goebel and J. Christophersen, *An integrated approach to battery health monitoring using bayesian regression and state estimation*, Autotestcon, 2007 IEEE, Baltimore, MD, 2007, pp. 646-653.

[167] S. Kumar; T.W.S. Chow, M. Pecht, *Approach to Fault Identification for Electronic Products Using Mahalanobis Distance*, Instrumentation and Measurement, IEEE Transactions on , vol.59, no.8, pp.2055 —2064, Aug. 2010.

[168] G. Box and D. Cox, *An analysis of transformations*, J. R. Stat. Soc., Ser. B Stat. Methodol., vol. 26, no. 2, pp. 211 —252, 1964.